HOW TO COMPARTMENTALIZE: GENOME COMPARTMENTALIZATION AFTER CELL DIVISION AND A NOVEL ROLE FOR LAMIN C

by
Victoria Elizabeth Hoskins

A dissertation submitted to Johns Hopkins University in conformity with the requirements for

the degree of Doctor of Philosophy

Baltimore, Maryland
August 2020

Abstract

The contents of the eukaryotic nucleus are highly organized for functional efficiency. This is seen on a variety of levels within the nucleus from protein-DNA hubs that perform particular roles, such as DNA damage repair, to higher organization of the chromatin itself. Lamina Associated Domains (LADs) are one such form or organization within the nucleus. LADs are largely inactive regions of chromatin that are proximal to the meshwork of lamins that underlie the nuclear membrane and are marked by specific repressive histone modifications. A type lamins, lamin A and lamin C, have been implicated as the lamin isotypes specifically responsible for proper LAD recruitment and anchoring at the nuclear periphery. These domains are developmentally regulated and are crucial for cell fate and identity. Disruption of this organization has been implicated in various disease pathogeneses. Here we show that LADs represent the same functional regions of the genome, including a shared sub-domain structure and boundaries, as the B compartment identified through chromatin capture techniques such as HiC. These studies have identified two types of 3D organization: areas of local self-interaction called topologically associated domains (TADs) and long-range genome-wide self-interactions that divide the genome into A (active) and B (inactive) compartments. Recently, we and others have demonstrated that these forms of genome organization are lost during mitosis as the chromosomes are reorganized and undergo large scale compaction. All genome organization is reestablished after mitosis during G1, but how this dynamic reorganization occurs is largely unknown. We have shown that LAD self-association occurs in anaphase prior to LAD establishment at the lamina. All of the LADs within a chromosome form 1-2 aggregates during anaphase and the nonLADs/A compartment of the chromosome form an exterior layer around these aggregates. These aggregates then make their way to the newly established nuclear periphery over the course of several hours where they become anchored and flatten along the lamina. The protein partners contributing to this process remain largely unknown however, we show that specifically lamin C plays a critical role in promoting proper LAD aggregation and establishment at the nuclear periphery, buffering intrachromosomal or intercompartmental interactions.

Primary Reader and Adivsor: Karen L. Reddy

Secondary Reader and Advisor: Loyal A. Goff

Acknowledgments

This thesis was a highly collaborative work and there are many folks who contributed to the science contained herein. The foundations of this project were laid down by Dr. Teresa Romeo Luperhcio (TRL), Dr. Xianwrong Wong (XW), Dr. Sauria (MEGS) and Dr. Karen L Reddy and this thesis would not have been possible without their foundational experiments.

I would like to thank TRL for the development of the Chromosome Conformation Paints (CCP) in collaboration with Agilent Technologies. She pioneered this method in the lab and drove the epigenetic perturbations portion of chapter 2. I would like to thank TRL, XW and MEGS for the collection and processing of the DamID data sets in both chapters 2 and 3. MEGS also drove and completed the analysis of the single-cell HiC data set in chapter 2.

I would like to further thank XW for doing the foundational experiments in chapter 3. He designed the Reddy lab version of the LAD/m6A tracer system and pioneered the lamin isotype knock downs. XW is the co-first author of the publication that resulted from the work contained in chapter 2, and attribution of that work should be shared between us equally. I would also like to acknowledge Jennifer Harr for the contribution of the TCIS work in chapter 2.

Other folks within the Center for Epigenetics also contributed a great deal to the success of this project and myself as a student. I would like to thank Dr. Rakel Tryggvadottir for her invaluable scientific help and friendship. I would also like to thank

David Vinson for training me in western blots and for his unwavering support throughout the final years of my thesis. I would also like to thank Dr. Kim Stephens who has been very supportive of my work and her advice on navigating the complex waters of graduate school got me through some sticky patches.

I would like to thank my mentors Dr. Karen L Reddy and Dr. Loyal A Goff for their tireless mentorship. I would not have completed this journey without their training and guidance. I would also like to thank the Goff Lab members (Dr. Genevieve Stein-O'brien, Dr. Kenji Johnson, Liz Vincent, Johnathan Augustin, Bri Winer, Alexa Perez-Torres, Ale Patino, Gabby Cannon) for all of their support and for being a scientific sounding board for me through this process.

Both the Human Genetics predoctoral training program and Biological Chemistry departments lent me a great deal of support and guidance though my training and I would like to extend a special thanks to them.

I would also like to pay tribute to my family who got me to this point in my career, without their love and support I would not be who I am today. I would like to especially thank my parents who taught me to persist even through great obstacles. Without that and many other qualities that they instilled in me, I would not have made it this far nor completed this dissertation.

Finally, I would like to thank my husband, Nicholas Schirillo, who has stood by me and supported me through this journey. Getting through graduate school is more than just doing experiments, it is a monumental journey, and without his support I do not think I would have made it through. Thanks for you ever easy smile and for always finding the joy in the little things.

Dedication

I would like to dedicate this thesis to my Nana, Fay Hoskins. She was what I aspire to be, both thoughtful and kind, as well as persistent, strong and bold.

Contents

List of Figures

Chapter 1: The interface between chromatin and the nuclear lamina

1.1 Introduction

The nucleus is a highly structured organelle with many compartments that act as hubs of interactions between protein, DNA and RNA. One such compartment within the nucleus is the microenvironment underlying the nuclear envelope where intermediate filament proteins, lamins, act as a link between the inner nuclear membrane (INM) and heterochromatin. These dynamic interactions regulate many cellular processes and when they are perturbed it can lead to varied and, often severe, disease phenotypes.

1.2 3D Genome organization and lamina associated domains

The nucleus is highly functionally organized, with regions of heterochromatin called Lamina Associated Domains (LADs) positioned at the nuclear periphery and more euchromatic regions positioned in the nuclear interior or interacting with nuclear pore complexes (NPC). While both heterochromatin and euchromatin compartments have long been identified by cytological measures using DNA stains, modern descriptions and analyses of of these chromatin domains and compartments has been obtained using mainly two different molecular methods: DamID and chromatin conformation capture (3C) methods such as HiC. DamID is most often used to detectLADs [1,2], while HiC is used to identify both local and long-range chromatin interactions [3–7]. In particular, HiC identifies local self-interacting regions called Topologically Associated Domains (TADs) and promoter-enhancer interactions as well as two broad self-interacting domains: the A (active)and B (inactive) compartments, with activity state of the compartments being operationally defined via intersections with transcriptome or, more often, with chromatin state [3–6]. While it has been believed for a while that LAD regions correlate with the B compartment, we have recently shown that LADs and the inactive B compartment identified through HiC, are analogous features sharing the same domain structures and boundaries [8]. In contrast to the A compartment, which is comprised of self-interacting domains and regulatory loops (TADs, sub-TADs), we showed that LADs are not bound by classic TAD forming proteins such as CTCF. This lack of binding is consistent with HiC based studies that show cohesin, another protein required for TAD formation, is not needed for A/B compartmentalization [9,10].

While LADs do not seem to be dependent on loop formation via CTCF and cohesin, some distinct regulators of these regions are known, such histone post-translational modifications. LAD formation/compartmentalization is dependent on repressive histone post translational modifications, H3K9me2/3 and H3K27me3, for their recruitment and maintenance at the nuclear lamina [11–14]. Beyond driving LAD anchoring these histone modifications are also important for LAD compaction and aggregation [8,12]. Heterochromatic regions have been shown to be attracted to each other and in the absence of a tethering force, such as A type lamins, all heterochromatin aggregates together in the center of the nucleus due its self attraction [15]. Further, heterochromatin associated factor HP1α has been shown to be able to form phase separated droplets in vitro the presence of naked DNA and has been shown to occur in vivo early in development in drosophila embryos [16,17]. This epigenetic silencing is also crucial for cell type specification and cellular identity and the LADed regions that are different between cell types contain cell-type specific/developmentally regulated genes [11,13,18,19]. A recent study finds that this control may go beyond broad cell types finding that the LADs positioned at the periphery in individual cells, within a cell type, are only a subset of LADS found through aggregate measures [20]. They further show that more gene dense regions fluctuate more in lamina association, implying that these disruptions may be due to differential gene usage between cells. It has also been shown that certain promoters can escape silencing within LADed regions [21]. These escaping promoters are generally less sensitive to H3K27me3 and lie in more weakly bound regions [21]. Further, when a LAD boundary is removed altogether it can cause the spread of neighboring euchromatin into that region causing upregulation of genes near the boundary [22]. Intriguingly, a recent study also showed that a similar effect can be found in mESC lacking all lamins, where LADs can escape the periphery to form new TAD association with nonLAD TADs causing expression of previously repressed genes [23]. Lamins provide a crucial role in genome organization through their anchoring or LADs as well as through their dynamic interaction with other proteins at the INM-chromatin interface.

1.3 Lamins dynamically regulate chromatin and the inner nuclear membrane

Lamins are intermediate filament proteins that help to regulate genome organization that underlie the nuclear envelope acting as an interface between the inner nuclear membrane (INM) and chromatin providing both structural and regulatory support to either side. There are two main subgroups of lamins: 1) the A type lamins, which include lamin A and lamin C, are mostly expressed in more differentiated cell types and 2) the B type lamins, which include lamin B1 and lamin B2 and are expressed throughout development. Lamins A and C are alternatively spliced isoforms transcribed from the LMNA gene, while lamin B1 and B2 are transcribed from separate genes. The different lamin isoforms form distinct irregular networks extending 14 ± 2nm below the nuclear envelope [24]. Each lamin isotype has been shown to form its own network but perturbations to one network affects the arrangement of the others [25]. They are also expressed in different ratios over developmental time and across tissue types, with predominantly B type lamins expressed in early development and lamins A and C beginning to be expressed as cells differentiate [26]. Further, lamins are decorated with post-translational modifications that attenuate their functions and many individual cellular roles have been discovered for each lamin isotype [27].

There have been few recent studies on specific roles for B types lamins and their role in genome organization remains unclear. While several studies show that Lamin B1 is dispensable for genome organization [28,29], one recent study found that disrupted LAD organization in triple knockout mESC can be rescued by reintroducing Lamin B1 [23]. Another intriguing study found that Lamin B1 associates with TAD boundaries dynamically over EMT in development, alluding to a role for Lamin B in the establishment of new LADs during differentiation [30].

While it remains unclear how much of a role B type lamins play in genome organization several roles in genome organization have been attributed to A type lamins. A type lamins are alternatively spliced off the LMNA gene such that the majority of their protein sequence is identical, with a long C-terminal tail on lamin A being the main difference. This tail undergoes specific processing steps that when perturbed lead to disease phenotypes [31]. A type lamins are crucial to the maintenance of heterochromatic LADs at the nuclear periphery, as well as for LAD and overall chromosome compaction [11,32]. Furthermore, laminAC interact directly with histone modifying proteins which contribute to gene regulation, such as HDAC2. HDAC2 is a histone deacetylase that is a member of transcription repressing complexes which interacts with LaminAC during oxidative stress to allow for the upregulation of response factors [33]. Recently, LaminAC has also been shown to dynamically recruit a regulator of HDAC2, PCAF, over differentiation of myoblasts leading to gene silencing [28,34–37]. Interestingly, laminAC has recently been shown to play roles in euchromatic regions of the genome as well. Lamin AC binds euchromatin early in development and the transition of these regions to heterochromatic ones over differentiation is facilitated by GlcNAcylated histone H2B [38]. However, more recent studies indicate that laminAC binding to euchromatic regions is more than just a way to guide regions to the nuclear periphery. One study found that phosphorylated (S22P) nucleoplasmic LaminAC binds enhancer regions and affects transcription, possibly through interactions with other proteins such as lap2α, which was shown by another group to enhance laminAC binding to euchromatin [39,40]. The S22P modification was found at higher levels on lamin C than lamin A, implicating a strong role for lamin C in this form of genome organization. Strikingly, a distinct role has also been recently found for lamin C in organizing compartmentalization by promoting proper self-aggregation of LADs and for LAD tethering at the nuclear periphery [28].

Beyond chromatin regulation lamins also interface with the INM and play crucial roles in regulating INM organization. Our recent study on this interconnected network of proteins detailed many players on either side of the nuclear lamina, many of which had been individually identified previously, to create a more holistic view of the microenvironment at nuclear envelope chromatin interface [41]. A type lamins in particular seem to display many important interactions with INM proteins. A recent study shows that in the absence of lamin AC emerin is unable to properly localize to the INM and recently these two proteins have been shown to regulate the cytoskeleton and chromatin mobility in concert [42]. Furthermore, A type lamins play a role in regulating NPC distribution. Lamin C fibers colocalize at super resolution with NPCs and in the absence of both A type lamins NPCs cluster together rather than dispersing across the membrane, indicating lamin C may be responsible for the spacing of NPCs. One study proposed that this is through interactions with TPR, an NPC protein member, although TRP may not exclusively bind A type lamins [35,43].This complex interface between INM, lamins and chromatin is tightly regulated, and this become especially apparent during cell division when the nuclear envelope and nuclear lamina get broken down and genome organization is dismantled to form mitotic chromosomes.

1.4 Dismantlement and reconstruction of the lamina interface through cell division

During mitosis the complex set of interaction between lamins, INM and chromatin are disrupted and after the segregation of chromosomes into daughter cells this network has to be functionally re-established. At the onset of mitosis there is large scale dismantlement of genome organization to form the mitotic chromosome structure, including dissociation of LADs from lamin proteins which become dispersed into the cytoplasm [12,44–46]. The mitotic organization is formed by a nested looping structure determined by length rather than by any other content (LAD/nonLAD identity, histone modifications, sequence identity, gene content etc.) which is anchored by condensin I and condensin II. Where condensin I forms the outer scaffold and condensin II forms this inner scaffold. As cells enter into anaphase and sister chromatids begin to segregate, LADs of individual chromosomes form agglomerates prior to nuclear envelope formation [12,45]. As chromosomes continue to segregate there is a transition from condensin driven organization to cohesin driven organization where chromosomes appear to exist in untangled loops without much structure [47]. This too is when the nuclear envelope and nuclear lamina must begin to reform. Lamin B is incorporated first into the reforming nuclear lamina at the transition from anaphase to telophase, followed quickly by lamin A [28,48,49]. At this time lamin C remains nucleoplasmic surrounding the LAD agglomerates, probably retaining the S22P modification [28,40]. At cytokinesis TADs and loops begin to rapidly form in the nonLAD compartment after cohesin and CTCF loading [47]. At this time LADs persist as agglomerates that have not anchored at the newly formed nuclear lamina. Slowly over the course of early G1 compartmentalization strengthens and LADs reach the nuclear envelope [12,45]. As LADs contact the nuclear lamina, the LADs at the distal portion of the chromosome make contact first earlier in G1 and over the course of several hours the more central portions become anchored, coinciding with the strengthening of compartmentalization and the flattening of domains against the lamina [12,50]. Furthermore, across this same time course lamin C becomes belatedly incorporated at the nuclear lamina. In the absence of lamin C during this reorganization LAD agglomerates merge together and fail to become established at the periphery [28]. As cells proceed through G1 and into S phase compartmentalization and LAD contact at the lamina continue to strengthen [45,50].

While these studies collectively reveal a nice model of the structure of 3D genome and lamina organization through the cell cycle there is not yet much insight into the interplay of these transitions in genome structure and the rebuilding of the INM and we lack an understanding of how the more elusive types of heterochromatin, such as telomeres and centromeres, may factor into this reorganization.

1.5 Impacts of Laminopathies on Genome Organization and Gene Regulation

Because A type lamins are at this complex dynamic interface between the INM and chromatin, when they are perturbed, they lead to severe and varied phenotypes. The diseases that result from mutations in LMNA, or other INM proteins that heavily interact with laminAC, are called laminopathies. Due to the complex interactions of LMNA and varied expression levels during development and in different tissue laminopathies display a wide breadth of phenotypes, pulling from four general categories: lipodystrophies, skeletal muscle disorders, peripheral neuropathies, and premature aging. These symptoms are caused both by dysregulation of the INM and genome which can cause perturbations in signaling, structural and mechanical functions, as well as genome organization and transcription. In this review we will focus on the effects on gene expression and genome organization.

One such syndrome that displays disrupted genome organization is Hutchinson's-Gilford Progeria Syndrome (HGPS), a rare mendelian disorder caused by a mutation in the tail of lamin A that does not allow proper processing. Patients with the syndrome experience severe symptoms that appear to be premature aging. One molecular effect of these mutations is dysregulation of genome organization. Patient fibroblasts at low passages show some loci are switch compartments followed by loss of compartmentalization after further culture [51]. This is thought to be caused by changes in H3K27me3 where it is gained in some gene rich regions and lost in gene poor regions [51]. This could also possibly be linked to lamin AC interactions with HDAC2. Another study showed that in the presence of progeria, under oxidative stress, the interactions of lamin AC and HDAC2 are lowered. This leads to changes in heterochromatin state [33]. Furthermore other types of heterochromatin are also dysregulated in this syndrome. HGPS stemming from the E145K mutation results in abnormal clustering of centromeres along with the mislocalization of telomeres [52]. Interestingly, the diffusion of centromeric and telomeric heterochromatin are altered in the presence of Lamin A depletion [53]. The roles of centromeres and telomeres in HGPS and other laminopathies have not been extensively studied, but doing so may reveal further insights into how these forms of heterochromatin behave throughout the cell cycle. Genome disorganization is not only caused in progeria but can also be linked to muscle defects in Emery-Dreifuss Muscular Dystrophy (EDMD). A recent study showed changes in LAD organization during muscle differentiation where some LADs are not recruited to the lamina and some nonLADS become aberrantly anchored at the periphery. This also leads to downstream gene expression changes, especially of sox2, which inhibits differentiation [54].

This mechanism of transcriptional disruption is not unique to EDMD. Impacts on genome organization often cause downstream transcriptional changes such as in Familial Partial Lipodystrophy (FPLD) which results from a mutation in the IG tail region of lamin A that results in an upregulation of an miRNA which normally resides in a LADed region of adipocytes after differentiation and is therefore silenced [55]. This mutation disrupts the local chromatin environment and allows enhancer promoter coupling and expression of this microRNA [55]. Furthermore, this mutation has recently been shown to have no effect on the structural properties of laminA [56]. While many transcriptional changes in these disorders result from disruption of LAD recruitment at the nuclear periphery, a recent study A type lamins directly to transcription by showing that lamin A and C bind enhancers when phosphorylated at serine 22. In cells expressing progerin, S22P lamin A and C bind novel sights causing an upregulation of clinically relevant genes [40].

1.6 Conclusion

The nuclear peripheral zone is a unique environment where nuclear lamins act as a bridge between the nuclear envelope and chromatin. These interactions are highly dynamic and serve important regulatory functions that lead to often severe disease phenotypes when perturbed. A recent and intriguing focus of the field has been cell division, during which this whole region is disassembled and reorganized. Cell division presents a prime opportunity to study the establishment and dynamics of the nuclear peripheral compartment.

Chapter 2: Chromosome conformation paints reveal the dynamic role of lamina associated domains in genome organization and regulation

2.1 Introduction

DNA is highly and dynamically organized within the eukaryotic cell nucleus. This spatial organization has been implicated in a variety of crucial processes including sequestration of proteins involved in transcription, developmentally coordinated gene expression, and RNA processing and DNA repair into nuclear sub-domains. Nuclear organization manifests in a hierarchy of structures, each of which tends to favor self-interaction. At the whole-nucleus level, chromosomes occupy distinct regions in the nuclear volume called chromosome territories (CT), suggesting that each chromosome has a three-dimensional self-interacting organization [57–61]. These CTs are identifiable microscopically using whole chromosome-specific DNA probes or “paints” in a fluorescence in situ hybridization (FISH) assay. Subsequent FISH studies have demonstrated a sub-territory level of organization tightly linked to gene activity, with certain domains within a CT changing their relative disposition depending upon activity state[60].

Recent high-throughput DNA sequencing based approaches, such as Hi-C or similar chromosome conformation capture (3C) based techniques, have been employed to uncover the organization of chromatin and identify self-interacting structures at the sequence level [3,5,6,62].

Two distinct types of structures have been found: locally self-interacting chromatin domains (TADs) and genome-wide predominantly bipartite spatial segregation known as the A- and B-compartment [5,62]. The B-compartment represents primarily repressed domains lacking self-interactions while the A-compartment displays robust self-interactions between active regions of the genome [5]. Compartment boundaries are typically bound by CTCF, which is highly depleted in the B-compartment, but can be found throughout the A-compartment in association with TADs [63].

DNA Adenine Methyltransferase Identification (DamID) is a genome-wide technique to identify nuclear lamina-proximal chromatin, thus measuring the spatial distribution of chromosomal sub-domains within the nuclear volume [64–68], These domains, termed Lamina Associated Domains (LADs) are approximately 100 kilobase (kb) to a megabase (Mb) in size and are enriched for transcriptionally silent genes and histone modifications indicative of facultative heterochromatin, such as histone H3 lysine 9 di- and trimethylation (H3K9me2/3) and histone H3 lysine 27 trimethylation (H3K27me3) [1,2,14,64,66,69–71]. Moreover, recent studies have demonstrated that both H3K9me2/3 and H3K27me3 are involved in LAD organization [14,66,71,72]. LADs are immediately flanked by active promoters, highlighting the stark delineation between repressed LAD domains and adjacent active regions. These borders also show enrichment for CTCF, as is seen in the boundaries between chromatin compartments observed by Hi-C [6,7,62,64]. LADs are enriched in the B-compartment [5,10,73], although a detailed exploration of the relationship between the domain architecture of LADs and chromosomal sub-domain organization, such as the A/B-compartments, is surprisingly lacking.

How LADs organize at the single-cell level is unclear. One study used live cell imaging of a cancer cell line and followed LADs from one cell cycle to the next, finding that only 30% of regions identified by DamID are lamina-proximal in any single cell [71]. While some of the LADs repositioned to the lamina with fidelity, others appeared to remain in the nuclear interior in the subsequent cell cycle. These data suggest that the organization detected by ensemble techniques, such as DamID, might obscure significant cell-to-cell variability. Another study employing single-cell DamID in a haploid cancer cell line demonstrated that there is some variability between individual cells with a substantial set of core LADs consistently maintained at the lamina [70]. LADs that showed an increased variability of lamina association in this cell line were enriched in developmentally regulated genes. However, many developmentally regulated loci, such as the Igh locus in pro-B cells, display association with the nuclear lamina in greater than 90% of cells, as measured by 3D-FISH, suggesting a robust interaction of developmentally programmed genes with the nuclear lamina in relevant cell types [66,74–80]. One caveat to these and many other FISH studies is that they largely rely on mapping a single or small number of loci within the nucleus [81]. Such an approach inherently misses some important information—particularly the relationships of LADs with each other and their positioning relative to other LADs, non-LADs, and the nuclear lamina within the context of the entire chromosome polymer. While oligopaint technologies have been employed to identify the disposition of multiple locations within the nuclear volume, these approaches have relied on either assaying relatively small regions (up to several megabases), or entire chromosomes but with low coverage [82–84].

Here we address the question of how LADs spatially organize within the nucleus, examining the relationships of LAD organization relative to both the nuclear lamina and non-LAD regions within an individual chromosome. We also investigate these relationships and spatial dynamics as the genome reorganizes post-mitosis and uncover an uncoupling of lamin association and LAD organization in early G1. In order to directly assess these relationships, we use two novel approaches to directly visualize LAD spatial organization at the single cell level: high density chromosome paints that differentially label LADs and non-LADs across an entire chromosome and a modified live cell LAD labeling system. Using high-density pools of chemically synthesized oligomers (Oligo Library Synthesis, OLS, Agilent Technologies) derived from DamID data in mouse embryonic fibroblasts (MEFs) [84,85], we are able to detect LAD and non-LAD domains in situ and within the context of an entire chromosome. With this, we demonstrate a functional organization of the chromosome territory and epigenetic requirements for organization in single cells only hinted at by population-based assays such as Hi-C, ChIP and DamID. We also utilize our chromosome conformation paints to examine LAD dynamics through specific stages of the cell cycle. We show the distinct phases of genome partitioning that underlie A/B-compartmentalization, in which LADs first aggregate followed by movement to the periphery. We employ a LAD labeling approach in live cells, enabling the visualization of LAD self-aggregation post-mitosis and establishment of the chromosomal subdomain at the nuclear periphery in real time. Finally, we confirm these temporal dynamics through single-cell Hi-C. Taken together, we demonstrate that single-cell measures are indispensable for understanding spatial organization and dynamics of LADs.

2.2 LADs, which largely correspond to the B-compartment, are reproducibly constrained in a peripheral zone of the nucleus in fibroblasts

To explore spatial organization and chromosome folding in single cells, we developed high resolution chromosome conformation oligopaints distinguishing LADs and non-LADs via a two fluorophore system. We first derived lamina-chromatin interaction maps in MEFs using DamID, which employs a bacterial adenine methyltransferase protein coupled to the nuclear lamina protein lamin B1 (LmnB1) (Fig. 2.1a) [64]. DamID material was initially hybridized to high-density tiling microarrays and replicate experiments were subsequently deep sequenced [66,86]. The resulting maps largely agreed with those previously published for MEFs (Fig. S2.1). Using LAD regions defined by our DamID array maps in MEFs, we derived 150 base oligonucleotide probes for both LAD and non-LAD regions across chromosomes 11 and 12 separately, taking into account GC content, hybridization temperature and filtering for uniqueness of sequence in the genome. The resulting chromosome conformation paints were comprised of 0.5 million high-density oligonucleotide probes per chromosome and were divided into LAD and non-LAD pools that were chemically coupled to easily distinguishable fluorophores (Fig. S2.1; Agilent Technologies).

In order to test whether the in situ organization of LADs is stochastic, as previously reported, or displays a more reproducible and constrained configuration, we performed FISH on 3D-preserved nuclei in ex vivo expanded early pass primary MEFs using our chromosome conformation paints [71,87]. LAD and non-LAD domains were clearly spatially segregated across the majority of their volumes and LADs were preferentially oriented near the lamina (Fig. 2.1b).

To assess the distribution of domains, we measured fluorescence intensity in medial image planes for at least 50 chromosomes along lines perpendicular to the nuclear periphery (as demarcated by LmnB1 staining) and passing through LmnB1, LAD and non-LAD signals, with three line measurements per territory (Fig. 2.1c and Fig. S2.2). For both chromosomes tested, LAD distributions demonstrated a close proximity to the lamina with a peak density of LAD signal at approximately 0.25 microns away and the majority of LAD signals resided within 0.6um of the nuclear lamina[71]. Distributions of LADs for both chromosomes 11 and 12 were almost identical despite differing LAD composition (49.97% versus 62.17% for chromosomes 11 and 12, respectively) (Fig. 2.1c and Figs. S2.3 and S2.4) suggesting that constraint at the nuclear lamina results from the physical properties of the interface and not from overall LAD content. We also observed that LADs aggregated and formed a compact sub-territory, while non-LAD distributions were much broader, peaking nearly a micron away from the lamina. Unlike the LADs, the non-LAD distributions varied between chromosomes suggesting a different type of structure for these domains. The compact nature of these LAD domains at the lamina irrespective of differential LAD density leads us to describe this region where LADs are restricted and interface with the edge of the nucleus as the “peripheral zone”[76]. The existence of the peripheral zone is supported by studies that show an enrichment or specific exclusion of chromatin factors proximal to the nuclear lamina [71,77,87]. Taken together, our observation of the peripheral zone with the restriction of the majority of the LAD signal and an under-representation of non-LAD signals suggests a functional nuclear domain.

Previous studies have shown an enrichment of LADs in the B-compartment, suggesting that these designations may represent orthogonal measures of the same structures. In order to clarify the relationship between LADs and the B-compartment, we compared our genome-wide MEF LAD data with MEF Hi-C data using a refined compartment calling method [88,89]. To achieve a higher resolution compartment metric, we created a maximum likelihood-based score with independent distance-based signal decay curves depending on the compartment state of both interacting bins. LAD DamID showed a high degree of overlap with this Hi-C based compartment score, including a strong agreement between LAD and B-compartment state (85.5%) as well as boundary locations (Fig. S2.5). Additionally, examination of B-compartment interactions showed self-associations within a single chromosome, which mirrors the compact organization of LADs of a single chromosome we observed by microscopy (Fig. S2.5e,f). Taken together, these data suggest that LADs and the B-compartment are measures of the same structural domains. The regions of disagreement were highly enriched in ambiguous compartment scores (close to zero), representing regions of low Hi-C sequencing coverage, transient lamina association, or mixed state across the population. Because the chromosome conformation paints cover these LAD and non-LAD regions, they are able to highlight the spatial organization and segregation of the A- and B-compartments within a chromosome and act as a surrogate marker of the A- and B- compartments.

2.3 LAD and A/B-compartment organization is dependent on both chromatin state and A-type lamins

Previous studies have demonstrated that the localization of at least some LADs to the nuclear lamina is dependent upon H3K9me2/3 and H3K27me3 and that the accumulation of these histone modifications may contribute mechanistically to LAD formation and maintenance [14,66,67,71,72]. Our group has previously shown that individual loci in LADs are directed away from the lamina upon disruption of either H3K9me2/3 or H3K27me3 [66]. To test the impact of disruption of these epigenetic marks on chromosome organization as a whole, we treated primary MEFs with Trichostatin A (TSA, an HDAC inhibitor that promotes histone acetylation), BIX01294 (which inhibits H3K9me2 through inhibition of G9a and G9a-like protein) or 3-Deazaneplanocin A (DZNep, which decreases H3K27me3 through inhibiting EZH2)[66,72,90–92]. DamID showed little to no disruption of LAD organization by these measures with scores for DZNep, BIX01294, and TSA treatments having mean correlations across all replicate combinations of 90%, 89%, and 81% with non-treated cells, respectively, on par with the 89% correlation between non-treated replicates (Fig. 2.2a and Fig. S2.6). These data appeared to contradict our previous study demonstrating the requirement for both H3K9me2/3 and H3K27me3 for individual LAD organization [66]. We hypothesized that since DamID is a longer-term ensemble measure of lamin association across a population of cells, single-cell variability in acute perturbations may be masked using this technique. To determine if these treatments altered in situ chromosome organization in single cells, we performed 3D-immunoFISH using our chromosome conformation paints (Fig. 2.2b). The level of disruption of LAD organization in individual cells was striking and varied from cell to cell (Figs.S2.7 and S2.8). Many chromosomes could not be scored by our methodology because of the disruption and disaggregation of the sub-territories leading to a distribution of LADs through multiple planes of the nucleus or predominantly non-medial chromosome localization. These treatments also altered the morphology of the nuclei. In agreement with previous studies, disruption of H3K9me2/3 or H3K27me3 caused relocalization of some LADs away from the lamina, although some portion of LADs in both chromosome 11 and chromosome 12 remained proximal to the nuclear lamina. To remain consistent with the scoring of the untreated cells, scoring was performed only on chromosomes that displayed lamina proximal LAD signal in the medial planes and had 1-2 identifiable chromosome territories, leading to an under-representation of organizational disruption (Figs. S2.7 and S2.8). Even with these limitations we were able to detect substantial reorganization (Fig. 2.2c). The most obvious effect of the drug treatments on LAD and non-LAD organization was dispersion and intermingling of both LAD and non-LAD chromatin, including a disaggregation of LADs that remained proximal to the lamina, suggesting a loss of A/B-compartmentalization and decrease in intra-chromosomal LAD associations. For all three drug treatments, our measurements demonstrate an expansion of the LAD sub-territory, loss of restriction to the peripheral zone, and an increase in the LAD and non-LAD spatial distribution variability across cells compared to untreated (Fig. 2.2c).

Previous data suggests a role for lamins in organizing chromatin to the nuclear lamina [26,29,66,93]. However, it is not clear how disruption of A-type lamins affects overall 3D organization within a chromosome. To test the role of lamin A/C in organizing LADs and the A/B-compartments across and within an individual chromosome, we removed lamin A/C by shRNA-mediated knockdown in MEFs. Knockdown of lamin A/C was nearly complete and did not affect either H3K9me2/3 or H3K27me3 (Fig. S2.9b). Similar to what we observed for the epigenetic perturbations, loss of lamin A/C did not result in substantially altered LAD profiles by DamID (Fig. 2.3a). To examine if the DamID ensemble measure was missing perturbations at the single-cell level, we performed 3D-immunoFISH with the chromosome conformation paints. This revealed significant chromosome disorganization in individual cells (Fig. 2.3b,c). Because of the complete disruption to LAD organization, distribution throughout the nuclear volume, and loss of distinct chromosome territories, many nuclei could not be scored (Fig. S2.9b). These disruptions included severe decompaction of the chromosome territory, intermingling of non-LAD and LAD signals (i.e. loss of A/B-compartmentalization), loss of peripheral association of many LADs and loss of LAD-to-LAD aggregation. We also observed that some of the organization of these chromosomes resulted in an “inversion” of chromosome organization, with LAD chromatin occupying the interior of the nucleus (Fig. S2.9b). This is in agreement with a previous study where an inversion of heterochromatin domains was noted in the absence of LMNA/C [26]. We note that this inverted chromatin phenotype was not observed for the epigenetic perturbations.

2.4 The B-compartment/LADs display step-wise organization through the cell cycle

We have previously shown that reorganizing a de novo LAD region to the nuclear lamina requires transit through the cell cycle, suggesting a link between mitosis and dynamic LAD reorganization [26,67,68]. To explore the dynamics of LAD/B-compartment reconfiguration and LAD reestablishment to the nuclear periphery after mitosis, we modified the previously described m6A-tracer system that demarcates LADs in live cells to label LADs specifically in interphase (Fig. 2.4a)[71]. By employing this modified LAD tracer system in a C57Bl/6j fibroblast cell line, along with a GFP-coupled single chain antibody to lamin, we observed that many LADs were not co-located with the reforming nuclear envelope during anaphase and telophase, in agreement with a previous study [71]. However, we found that these nucleoplasmic LADs did relocate to the nuclear periphery later in G1, taking nearly two hours post-mitosis to fully regain their lamina-proximal configuration (Fig. 2.4b). Based on the size and distribution of these LAD signals in early G1, we concluded that each aggregate was comprised of many LADs in the nuclear interior prior to lamina association. To measure the distribution and number of aggregates more carefully, we next employed super-resolution structured illumination microscopy (SIM) to measure LAD organization in mid-G1 versus early G1 cells (Fig. 2.4b,c). Each nucleus contained 70 to 100 LAD-aggregates. Accounting for ploidy (3-4N), this corresponded to 1-2 LAD aggregates per chromosome, suggesting that LADs within individual chromosomes self-aggregate. LAD signals at the periphery, while punctate in appearance, appeared to compress or spread out along the nuclear lamina later in G1. To further solidify the timing of this process we employed live cell super-resolution of these cells starting at metaphase and through nuclear lamina reformation. We found that aggregation of LAD domains occurs asynchronously beginning as early as the start of anaphase and continues until the nuclear lamina has reformed (Fig. 2.5). While this phenomenon occurs on every chromosome the process is the most apparent when focusing on lagging chromosomes where the entire body of the chromosome can be observed (Fig. 2.5, magnified images). Taken together these results indicate that compartmentalization occurs as early as anaphase, prior to nuclear lamin formation, and over the course of several hours LAD aggregates become belatedly established at the nuclear periphery.

2.5 Separate compartmentalization and relocation observed in single-cell Hi-C data

To better understand the relationship between LAD organization and compartments during the cell cycle, we analyzed LAD organization within publicly available single-cell Hi-C (scHi-C) data obtained from cells throughout the cell cycle [45]. Our analysis used 506 haploid cell datasets spanning the entire cell cycle with a minimum of 100,000 interactions each. Cells were ordered through the cell cycle according to the scores detailed by Nagano et al. (Fig. 2.6a) [45]. For every dataset, we ran multiple molecular dynamic annealing simulations at a resolution of 100 Kb to obtain three-dimensional chromatin configurations, selecting the best-fitting model for each cell. We then classified each 100 Kb region as LAD or non-LAD according to its majority membership. Our results confirm a dramatic reorganization of LADs and A/B-compartment configuration during different stages of the cell cycle and highlight the step-wise organization of LADs after mitosis. During mitosis, cells exhibited extensive interactions between LAD and non-LAD regions of chromatin, suggesting that A/B-compartmentalization is absent in this time-frame, in agreement with previous studies. Immediately after entering G1, we observed a large reduction in these inter-region interactions, while interactions within LAD chromatin, the presumptive B-compartment, increased (Fig. 2.6b), suggesting that compartmentalization is established almost immediately after mitosis, in strong agreement with our imaging data. This compartmentalization, also consistent with the imaging results, was not concurrent with the radial partitioning observed between non-LADs/LADs and A/B-compartment during the majority of the cell cycle (Fig. 2.6c). Instead, these data showed that LADs remained in the nuclear interior during early G1 as aggregated foci (B-compartment), reducing their contact with non-LAD chromatin (A-compartment). This radial segregation increased throughout G1 and S phase. We also examined local chromatin separation (distance between sequences 200 Kb apart) for both LADs and non-LADs (Fig. 2.6d). There was little difference in local separation of these domains at the resolution investigated here throughout G1. Differences only became evident in S phase, with relative LAD chromatin spacing increasing throughout until it peaked at the beginning of G2 and disappeared by mitosis. Taken together, the segregation of LADs at the periphery appear to involve three steps, which are supported by imaging data. First, a reduction in inter-state (A/B-compartment or non-LAD/LAD) interactions is accomplished independently of compaction or spatial isolation. Second, non-LADs/LADs are isolated from each other along the radial axis of the nucleus. Third, as LADs interact more with the periphery, individual LADs spread out across the lamina, suggesting that LAD/B-compartment regions assume a different topology compared to non-LAD/A-compartment regions. We also observed a reduction in the fidelity of chromosome territories as interphase proceeded (Fig. 2.6e). These appear to be driven entirely by non-LAD chromatin as the levels of LAD interchromosomal interactions remain unchanged throughout interphase.

2.6 Chromosomes separate into subdomains independent of nuclear envelope assembly

Chromosome conformation paints and ensemble Hi-C data show that many LADs interact in a chromosome sub-territory, and both the LAD tracer system and single cell Hi-C data indicate that at least some LADs form an intra-chromosomal B-compartment prior to their organization to the lamina. By counting the number of large foci in the LAD-tracer system immediately post-mitosis, we inferred that the LADs may self interact in 1-2 large domains per chromosome. In order to determine if LADs from a single chromosome form a single aggregate and the relative organization of A-compartment chromatin, we used our chromosome conformation paints to visualize the LADs/non-LADs within either chromosome 11 or chromosome 12 transiting mitosis. In primary MEFs, early G1 daughter cells clearly showed a single LAD or B-compartment domain that was not associated with the nuclear lamina and was surrounded by the non-LAD or A-compartment chromatin, which was often found more proximal to the lamina at this stage (Fig. 2.7a,b). These data agree with formation of a single LAD/B-compartment aggregate within an individual chromosome. It is also clear that the nuclear lamina is not scaffolding the formation of the B-compartment or LADs, but rather that these interactions precede association with the nuclear periphery. These results highlight a transient stage in late anaphase, prior to nuclear envelope reformation but after daughter cell chromosome segregation, during which A/B-compartmentalization and LAD-LAD self-interactions are already being established (Fig. 2.7c).

2.7 Discussion

Organization of LADs has been studied in a variety of cell types, both by genomic and cytological measures. Genome-wide approaches allow for global measurement of lamin association with high-resolution but give only an average measure of the population while single-cell approaches can capture variability between cells but at low resolution [70]. Conversely, cytological measures permit in situ measurements of nuclear partitioning either for specific loci in fixed cells (FISH), or LADs genome-wide in live cells (LAD-tracer system). With this study, we have bridged this gap using a combination of chromosome conformation paints and a modified LAD-tracer system to examine chromosome-wide LAD and A/B-compartment configurations in situ within the 3D context of the chromosome fiber and LAD dynamics through the cell cycle, respectively. Thus we establish organizing principles of LADs, both in their localization and formation.

Application of the chromosome conformation paints in primary early pass MEFs demonstrates that LADs are not strictly stochastic in their association with the nuclear lamina, but instead display a constrained configuration within a contiguously occupied peripheral zone (Fig. 2.1c). This zone results from the combination of lamina proximity and aggregation of LADs together, specifically those occupying the same chromosome. Our description of a peripheral zone compliments recent findings using TSA-seq as a molecular ruler defining an axis of increasing transcriptional activity from the lamina (repressive) to nuclear speckles (highly transcriptionally active)[94]. Our results also suggest that some LAD regions are more lamina distal, but still exist as part of a LAD aggregate seated against the lamina under spatial constraint. Using ensemble Hi-C measures, we confirm the within-chromosome aggregation of LADs and demonstrate the extensive overlap of LADs and the B-compartment, concluding our chromosome conformation paints allow us to visualize in vivo A/B-compartmentalization and both measures are indicative of LAD/B-compartment partitioning to the peripheral zone.

Our observations of LAD dynamics through the cell cycle further underscores LAD aggregation by showing it is independent of and precedes localization of the LADs to the nuclear lamina (Fig. 2.4, Fig. 2.5). This process is also independent of the nuclear envelope, since aggregation of LADs occurs in anaphase, prior to nuclear envelope reformation. We propose that

LAD formation and disposition is a three stage process beginning immediately post-mitosis. First, as chromatids decondense, LADs begin a process of aggregation, eventually forming foci (1-2 per chromosome) by early G1 (Figs. 2.7 and 2.8). Second, these foci are localized to the nuclear periphery and third, are subsequently spread out and adopt a more extended configuration as a greater portion of the LAD aggregates interact with the lamina (Fig. 2.8). However, the dissociation of the LADs from the lamina during mitosis begs the question, by what mechanism are LADs moved to the periphery. More comprehensive visualization techniques such as we have described may yet provide an answer.

We demonstrate that both aggregation and localization organizational forces are dependent on epigenetics (Figs. 2.2 and 2.3). Disruption of histone methylation machinery and increased histone acetylation led to similar outcomes, with disaggregation of the LAD sub-territory at the periphery and movement of some LADs away from the lamina. Our observations of LAD aggregation and a peripheral zone that partitions the A and B-compartments, rather than a strict coupling of the LAD regions to the lamina, are supported by recent work suggesting that heterochromatin is sequestered via phase separation [95–97]. What is less clear is the specific role of Lamin A/C in this process. Previous work showed that there is a developmental transition from utilizing Lamin B Receptor (LBR) to Lamin A/C for lamina association and constitutive loss of these proteins led to an inverted chromatin organization with heterochromatic domains occupying the nuclear interior [26]. Modeling of chromosome folding behavior in this study agrees with our experimental data that LAD/B-compartment heterochromatin domains drive self-organization and that scaffolding at the lamina is an independent force contributing to the radial position of chromosomal domains, but not self-association of LADs [98]. Here we show that acute loss of

Lamin A/C by shRNA-mediated depletion caused a subset of MEFs, which do not express appreciable levels of LBR, to display an inverted LAD organization, in agreement with those prior studies identifying inverted heterochromatic structures in the absence of Lamin A. We note that this phenotype was not fully penetrant, likely reflecting the varying levels of Lamin A/C remaining in these cells or the time-scale during which the cells were lacking A-type lamins. Through our separate analysis of epigenetic marks and composition of the nuclear periphery, we have begun to dissect the roles each play in 3D nuclear organization, and suggest that aggregation of LADs and positioning at the nuclear periphery are temporally and spatially distinct processes.

Understanding principles of LAD organization is dependent on our ability to resolve both temporal dynamics and cell-to-cell variability. Our study of genome organization and establishment of nuclear sub-domains attempts to overcome limitations imposed by fixed cell labeling and ensemble genomic measures. Our combined approach reveals multiple forces working in collaboration to establish the canonical LAD organization seen and B-compartmentalization predicted across the vast majority of time-points and cell types. The chromosome conformation paints , designed based on genome-wide molecular data, clearly indicate preferential LAD and non-LAD organization. We directly confirm A/B-compartmentalization in an in vivo 3D whole-chromosome context. The epigenetic and LaminA/C perturbations suggest possible mechanisms for both aggregation and peripheral association, respectively. Live cell measurements of LADs demonstrate the dynamics of peripheral association post-mitosis and analysis of single cell Hi-C support the idea of step-wise compartmentalization and organization of chromosomes after nuclear breakdown. Finally, chromosome conformation paints during these time points without nuclear lamina involvement reveal the subdomain organization of the chromosomes as the underlying driving force for compartmentalization. Taking these results together, this multi-approach study highlights the complexity of the underlying forces working in conjunction to establish and maintain nuclear compartmentalization and chromatin architecture.

2.8 Experimental models

Generation and maintenance of primary murine embryonic fibroblast (MEFs)

For primary MEFs, wild-type eight-week-old C57BL/6 mice were bred and embryos were harvested at E13.5. Individual embryos were homogenized using a razor blade, and cells were dissociated in 3 mL 0.05% trypsin for 20 min at 37°C, then 2 mL of 0.25% trypsin was added and incubated again at 37°C for 5 min. Cells were pipetted vigorously to establish single cells, passed through a 70 µm cell strainer, pelleted and then plated in 10 cm dishes and labeled as P0. MEFs were cultured DMEM High Glucose with 10% FBS, penicillin/streptomycin, L-glutamine and non-essential amino acids. Cells were cultured for no longer than 5 passages before harvesting for experiments. For initial DamID experiments, longer term-culture C57BL/6 MEFs were purchased from ATCC (American Tissue Culture Collection, CRL-2752) and cultured according to their established protocols, in medium containing DMEM High, 10% FBS, Penicillin/Streptomycin and L-glutamine.

2.9 Methods

Drug treatments

Primary MEFs were cultured as described and were treated with epigenetic modifying drugs for 24-60 hours, as previously described. Drugs were added to the media at the following concentrations and refreshed at 24 hour intervals: 40 ng/mL TSA (Sigma, 1952), 0.5 µM BIX01294 (Ryan Scientific, RYS-AF-0051), 0.25 µM DZNep (Cayman Chemical, 13828, batch 0443536-5). For 3D-immunoFISH experiments, MEFs were treated with inhibitors while grown on slides. For drug treatment combined with DamID, primary MEFs were treated for 18-24 hours with the specified inhibitor, prior to infection with DamID virus.

Lamin A/C knockdown

shRNA-mediated LMNA/C knockdown was carried out as described previously. Briefly, virus for knockdowns was generated in HEK 293T/17 cells (ATCC CRL-11268) by co-transfecting VSV-G, delta 8.9, and shLmnA/C (Sigma, clone NM_001002011.2-901s21c, 5'-GCGGCTTGTGGAGATCGATAA-3') or shluciferase (5'-CGCTGAGTACTTCGAAATGTC-3') with Fugene 6 transfection reagent (Promega E2691). 10 mM sodium butyrate was then added to the transfected cells 3 hours post transfection for an overnight incubation at 37°C, 5% CO2. The transfection media containing sodium butyrate was removed the following day and the cells were washed with 1X PBS. Opti-MEM was then added back to the cells which were then incubated at 37°C, 5% CO2. Viral supernatant was collected every 12 hours up to 3 collections and the supernatant of all 3 collections were pooled. Primary MEFs were cultured as described and incubated overnight with shLmnA/C or shluciferase fresh viral supernatants supplemented with 4 µg/mL polybrene and 10% FBS for 12-14 hours. Fresh MEF media was then added to the cells after the virus was removed and selected with 10 µg/ml blasticidin. For DamID profiling, cells were infected with DamID virus 4 days post shRNA transduction and cultured for additional 48 hours.

DamID Infection

DamID was performed as described previously (Reddy et al 2008). Cells were either transduced with murine retroviruses or with lentiviruses harboring the Dam constructs. Self-inactivating retroviral constructs pSMGV Dam-V5 (Dam-Only) and pSMGV Dam-V5-LaminB1 (Dam-LaminB1) were transfected using Fugene 6 transfection reagent (Promega, E2691) into the Platinum-E packaging line (Cell Biolabs, RV-101) to generate infectious particles. These viral supernatants in DMEM were used to directly infect MEF lines. Lentiviral vectors pLGW-Dam and pLGW Dam-LmnB1 were co-transfected with VSV-G and delta 8.9 into HEK 293T/17 packaging cells using the Fugene 6 transfection reagent in DMEM High glucose complete media (DMEM High glucose supplemented with 10% FBS, Penicillin/Streptomycin, L-glutamine). 10 mM sodium butyrate was added to the transfected cells 3 hours post-transfection and left overnight. The following day this media was removed and the cells were washed briefly with 1X PBS before Opti-MEM media was added. Supernatants containing viral particles were collected every 12 hours between 36-72 hours after transfection, and these collections were pooled, filtered through 0.45 µM SFCA or PES, and then concentrated by ultracentrifugation. For infection with retrovirus or lentivirus, MEFs were incubated overnight with either Dam-only or Dam-LmnB1 viral supernatant and 4 µg polybrene. Cells were allowed to expand for 2-4 days then pelleted for harvest.

DamID protocol

MEFs were collected by trypsinization and DNA was isolated using QIAamp DNA Mini kit (Qiagen, 51304), followed by ethanol precipitation and resuspension to 1 µg/ul in 10 mM Tris, pH 8.0. Digestion was performed overnight using 0.5-2.5 µg of this genomic DNA and restriction enzyme DpnI (NEB, R0176) and then heat-killed for 20 minutes at 80°C. Samples were cooled, then double stranded adapters of annealed oligonucleotides (IDT, HPLC purified) AdRt (5′-CTAATACGACTCACTATAGGGCAGCGTGGTCGCGGCCGAGGA-3’) and AdRb (5′-TCCTCGGCCG-3’) were ligated to the DpnI digested fragments in an overnight reaction at 16°C using T4 DNA ligase (Roche, 799009). After incubation the ligase was heat-inactivated at 65°C for 10 minutes, samples were cooled and then digested with DpnII for one hour at 37°C (NEB, R0543). These ligated pools were then amplified using AdR_PCR oligonucleotides as primer (5′-GGTCGCGGCCGAGGATC-3’) (IDT) and Advantage cDNA polymerase mix (Clontech, 639105). Amplicons were electrophoresed in 1% agarose gel to check for amplification and the size distribution of the library and then column purified (Qiagen, 28104). Once purified, material was checked for LAD enrichment via qPCR (Applied Biosystems, 4368577 and StepOne Plus machine) using controls specific to an internal Immunoglobulin heavy chain (Igh) LAD region (J558 1, 5′-AGTGCAGGGCTCACAGAAAA-3′, and J558 12, 5′-CAGCTCCATCCCATGGTTAGA-3’) for validation prior to microarray hybridization and/or sequencing.

DamID-seq Library Preparation

In order to ensure sequencing of all DamID fragments, post-DamID amplified material was randomized by performing an end repair reaction, followed by ligation and sonication. Briefly, 0.5-

5 µg of column purified DamID material (from above) was end-repaired using the NEBNext End Repair Module (NEB E6050S) following manufacturer's recommendations. After purification using the QIAquick PCR Purification Kit (Qiagen, 28104), 1µg of this material was then ligated in a volume of 20 µL with 1µl of T4 DNA ligase (Roche, 10799009001) at 16°C to generate a randomized library of large fragments. These large fragments were sonicated (in a volume of 200µL, 10mM Tris, pH 8.0) to generate fragments suitable for sequencing using a Bioruptor® UCD-200 at high power, 30 seconds ON, 30 seconds OFF for 1 hour in a 1.5 mL DNA LoBind microfuge tube (Eppendorf, 022431005). The DNA was then transferred to 1.5 ml TPX tubes (Diagenode, C30010010-1000) and sonicated for 4 rounds of 10 minutes (high power, 30 seconds ON and 30 seconds OFF). The DNA was transferred to new TPX tubes after each round to prevent etching of the TPX plastic. The sonication procedure yielded DNA sizes ranging from 100-200 bp. After sonication, the DNA was precipitated by adding 20 µl of 3M sodium acetate pH 5.5, 500 µl ethanol and supplemented with 3 µl of glycogen (molecular biology grade, 20 mg/ml) and kept at -80°C for at least 2 hours. The DNA mix was centrifuged at full speed for 10 min to pellet the sheared DNA with the carrier glycogen. The pellet was washed with 70% ethanol and then centrifuged again at full speed. The DNA pellet was then left to air dry. 20 µl of 10 mM Tris-HCl was used to resuspend the DNA pellet. 1 µl was quantified using the Quant-iT PicoGreen dsDNA kit (Invitrogen, P7589). Sequencing library preparation was performed using the NEBNext Ultra DNA library prep kit for Illumina (NEB, E7370S), following manufacturer's instructions. Library quality and size was determined using a Bioanalyzer 2100 with DNA High Sensitivity reagents (Agilent, 5067-4626). Libraries were then quantified using the Kapa quantification Complete kit for Illumina (Kapa

Biosystems, KK4824) on an Applied Biosystems 7500 Real Time qPCR system. Samples were normalized and pooled for multiplex sequencing.

LAD and non-LAD chromosome-wide probe design and labeling

LADs from murine embryonic fibroblasts were defined through the LADetector algorithm, and complementary regions to Chromosomes 11 and 12 were defined as non-LADs. Data provided Geo GSE56990. Centromeres were excluded, and LAD and non-LADs were repeat masked. Probes were selected in silico based on TM and GC content, and those with high homology to off target loci were specifically removed. 150 base pair oligos were chemically synthesized using proprietary Agilent technology and probes were labeled in either Cy3 or Cy5 dyes using the Genomic DNA ULS Labeling Kit (Agilent, 5190-0419). 40 ng of LAD and non-LAD probes were combined with hybridization solution (10% dextran sulfate, 50% formamide, and 2X SSC) then denatured at 98°C for 5 minutes and pre-annealed at 37°C.

3D-ImmunoFISH and immunofluorescence

3D-immunoFISH was performed as described previously\cite{Reddy2008-ut,Harr2015-eh,Solovei2013-iz}. Briefly, primary fibroblast cells were plated on poly-L-lysine coated slides overnight. Cells on slides were fixed in 4% paraformaldehyde (PFA)/1X PBS for 15 minutes, then subjected to 3-5 minute washes in 1X PBS. After fixation and washing, cells were permeabilized in 0.5% TritonX-100/0.5% saponin for 15-20 minutes. The cells were washed 3 times 5 minutes each wash in 1X PBS, then acid treated in 0.1N hydrochloric acid for 12 minutes at room temperature. After acid treatment, slides were placed directly in 20% glycerol/1X PBS and then incubated at least one hour at room temperature or overnight at 4°C. After soaking in glycerol, cells were subjected to 4 freeze/thaw cycles by immersing glycerol coated slides in a liquid nitrogen bath. Cells were treated with RNAse (100 µg/ml) for 15 min in 2X SSC at room temperature in a humidified chamber. DNA in cells was denatured by incubating the slides in 70% formamide/2X SSC at 74°C for 3 min, then 50% formamide/2X SSC at 74°C for 1 min. After this denaturation, cells were covered with a coverslip containing chromosome conformation paints in hybridization solution and sealed. After overnight incubation at 37°C, slides were washed three times in 50% formamide/2X SSC at 47°C, three times with 63°C 0.2X SSC, one time with 2X SSC, and then two times with 1X PBS before blocking with 4% BSA in PBS for 30-60 min in a humidified chamber. Slides were then incubated with primary antibody (1:200 dilution; Santa Cruz, SC-6217) in blocking medium overnight at 4°C. Slides were washed three times with 1X PBS/0.05% Triton X-100 and then incubated with secondary antibody in blocking medium DyLight 488 (1:200 dilution; Jackson ImmunoResearch, 211-482-171) for 1 hour at room temperature. Post incubation, slides were washed three times with 1X PBS/0.05% Triton X-100, and then DNA counterstained with 1 µg/ml Hoechst. Slides were then washed, mounted with SlowFade Gold (Life Technologies, S36936).

Live Cell imaging

B6 3T3 Cells stably expressing Dam-V5-LaminB1-CDT, [m6A tracer construct] and [single chain antibody construct] were seeded on 5mm coverslips coated with Pol-L-Lysine. Cells were grown in the presence of shield ligand for 24 hours and simultaneously synchronized with a single 1mM thymidine block for 24 hours followed by release by addition of 25µM 2'-Deoxycytidine for 4 hours. Cells were then blocked at G2/M by incubation with 10uM R0-3306 for 16-20 hours. Cells were release by washing 3 times with warm Fluorobrite DMEM +10% FBS, Penicillin/Streptomycin and L-glutamine. 2 hours after release cells were imaged every seconds using a 3i spinning disc confocal microscope or Nikon SIM super resolution microscope for early G1 imaging. Interphase cells were not synchronized and were imaged every seconds.

FISH Image acquisition and processing

Slides were imaged using a Zeiss Axiovert fitted with an ApoTome and AxioCam MRm Camera. Imaging was performed at 100x or 63x with an Apochromat oil immersion objective with an NA of 1.5 using Immersol 518. (check all these details). AxioVision software was used to acquire images and .zvi files were exported and processed in FIJ. Chromosome territories were evaluated for nuclear position and attachments to the lamina. As all chromosome 11 and 12 territories were visually determined maintain some level of proximity to the lamina, territories were measured through LAD signals closest to the lamina (lamin B1 signal) in medial planes. The distribution of LAD and non-LAD signals was measured using line scans in triplicate from outside to inside the nucleus and histogram measurements of pixel intensity were acquired for each channel using FIJI. Nuclei that were polyploid for chromosome 11 or 12, exhibited damage or were not fully visible in the field were excluded from the analysis. For each measurement, maximum lamin B1 signal was set to x=zero and all distances are relative to this zero point. Distance measurements were normalized by total pixel intensity (Normalized value = Pixel intensity/Sum of total pixel intensity). Data was collected from multiple experiments performed on different days and results were pooled.

DamID-seq Data Processing

DamID-seq reads were processed using LADetector (https://github.com/thereddylab/pyLAD) , an updated and packaged version of the circular binary segmentation strategy previously described for identifying LADs from either array or sequencing data\cite{Harr2015-eh,Zullo2012-ge}. For arrays, DamID array signal intensity data were lifted over to mm9 using the Galaxy converter tool, and then data from replicate arrays were averaged together and quantile normalized and smoothed with the preprocessCore R package. DamID array data were analyzed using an earlier version of LADetector (https://github.com/thereddylab/LADetector). For both sequencing and array DamID data, LADs separated by less than 25 kb were considered to be part of a single LAD. All other parameters were left at default values. LADs were post-filtered to be greater than 100 kb, complementary genomic regions to LADs were defined as non-LADs. BedGraphs were generated for array data visualization using bedtools genomecov and output from the pyLAD LADetector for sequencing data.

CTCF Data Processing

CTCF ChIP-seq sequencing data and associated control were downloaded from SRA (GSM426758). Data were aligned to the mouse genome build 9 using Bowtie version 1.1.1 allowing up to 2 seed mismatches, the “--tryhard” option, and only reporting uniquely mappable reads. All other parameters were left with default values. Peak calls and pileup tracks were generated using MACS2 version 2.1.1.20160309}. With the exception of setting the genome to mouse, all other parameters were left with default values.

Hi-C normalization

Raw sequences for MEF Hi-C data from Krijger et al. (GSE76479) were obtained from GEO. Read ends were aligned to the mouse genome build 9 using BWA mem version 0.7.12-r1039 and default settings. Reads were kept if they met one of the following criteria: Each read end mapped to a single position; one end failed to map but the other end mapped to two positions falling in two different restriction fragments; both ends mapped to no more than two positions from different restriction fragments and the downstream position of one end occurred on the same fragment as the upstream position of the other end. All replicates were combined. Reads were processed and normalized using HiFive version 1.3.2. A maximum insert size of 650 bp was used to filter reads. Fends were filtered to have a minimum of one valid interaction.

The data were normalized using the binning algorithm correcting for GC content, fragment length, and mappability. GC content was calculated from the 200 bp upstream of restriction sites or the length of the fragment, whichever was shorter. Mappability was determined using the GEM mappability function, version 1.315}. Mappability of 36-mers was calculated every 10 bp with an approximation threshold of six, a maximum mismatch of 1 bp, and a minimum match of 28 bp. For each fend, the mean mappability score for the 200 bp upstream of the restriction site, or total fragment size if smaller, was used. For normalization, only intra-chromosomal reads with an interaction distance of at least 500 kb were used. GC content and fragment length were partitioned into 20 bins each and mappability was partitioned into 10 bins. All parameter partitions were done such that together they spanned the full range of values and contained equal numbers of fends in each bin. All bins were seeded from raw count means and GC and length parameters were optimized for up to 100 iterations or until the change in log-probability was less than one, whichever was achieved first.

Hi-C Compartment Scoring

Eigenvector-based compartment scores were calculated as previously described. Enrichments were calculated for either 1 Mb (low-resolution) or 10 kb bins (high-resolution). Bins were expanded using HiFive's dynamic binning to a minimum or 3 reads per bin. For each pairwise combination of rows for the enrichment heatmap, the Pearson correlation was calculated. Taking the first eigenvector of the correlation matrix yielded the eigenvector-based compartment score. Because the sign of the eigenvector is random, we used mean transcriptional activity in positively versus negatively scored regions to determine A and B-compartment score signs. Where necessary, signs were flipped so that all B-compartments corresponded to positive eigenvector scores.

Likelihood compartment scores were calculated as the log2-transformed ratio of the probability of each 10 kb interval occurring in the B-compartment divided by the probability of that interval occurring in the A-compartment. The sign of the high-resolution first eigenvector score described above determined compartment initialization (positive values were associated with the B-compartment). Bins with fewer than five interactions longer than 1.5 Mb were removed. Interactions spanning 1.5 Mb or greater were divided into three groups: both sides occurring in the A-compartment, the B-compartment, or one side in each compartment. The distance dependent signal curve for each category was calculated by find the sum of counts divided by the sum of expected values at each distance interval. For distance intervals containing fewer than 10000 reads were joined with the next largest interval prior to finding enrichment. This was continued until the 10000 read minimum was met. The effective distance for joined bins was calculated as the mean of the log-transformed bin distances. Enrichment values for distances corresponding to bins that had fewer than 10000 reads were interpolated linearly based on the log-transformed expected values and log-transformed distances of the two adjacent bins. The probability for each interval was calculated under the Poisson distribution as follows:

where si is the compartment state of interval i, Ai is the set of valid interactions of at least 1.5 Mb involving interval i, cij is the sum of observed counts for the interaction bin between intervals i and j, fij is the sum of interaction normalization values for bin ij, dij is the distance between midpoints of intervals i and j, and Dgg and Dggc are the distance dependent signal functions for within compartments of type b and between different compartments, respectively.

Training was accomplished on a chromosome by chromosome basis in an iterative fashion, calculating the distance dependent signal curves, calculating the compartment scores, updating the top 50% of scores (rounding up), and adjusting states based on the signs of the scores. This was performed for up to 200 rounds. If a stable set of interactions was achieved, the associated scores were kept. If a chromosome began switching between two sets of stable states, the mean of these two sets of scores was taken. Otherwise after a 20 round burn-in period, scores were sampled every round and the mean score for each interval was taken after the final iteration.

Single cell Hi-C Modeling

Haploid single cell Hi-C processed counts from Nagano et al.} were obtained from the Tanay lab (http://compgenomics.weizmann.ac.il/files/archives/schic_hap_2i_adj_files.tar.gz and http://compgenomics.weizmann.ac.il/files/archives/schic_hap_serum_adj_files.tar.gz). Only cells with a total of 100,000 reads or more were used. Data were further filtered using HiFive single cell Hi-C filters. This involved removing fragment ends (fends) with no interactions, fends smaller than

21 bp or larger than 10 Kb, and all fends not originating from chromosomes 1 through 19 or X. Next, because only haploid cell data were used any fend with more than two interactions was removed and fends with exactly two interactions were removed it the interactions occurred with partner fends more than 40 fends apart; otherwise, the longer of the two interactions was kept. Finally, fends were partitioned into 1 Mb bins and a connectivity graph was created with edges present if at least one unfiltered interaction existed between bins. For each edge, interactions were removed if the next shortest path between bins was longer than three steps.

Modeling was performed for each cell dataset using a coarse grained annealing molecular dynamic simulation. Chromatin was represented as beads representing 100 Kb beads, starting from the first 100 Kb bin for each chromosome containing at least one valid interaction and ending with the last bin containing a valid interaction. Intervening bins containing no interactions were kept for the purposes of modeling but excluded for all subsequent analyses. The force field was setup similar to that described by Nagano et al.. Two forces were applied to each bead, a general repulsive force and a harmonic bonding force. All pairwise combinations of beads, with the exception of those having scHi-C interactions, were given a repulsive force with a scaling factor (k1) of one for distances less than 60 nm (d_{lim}).

$F_{rep}=k_1(d-d_{lim})$

All beads representing adjacent chromatin bins (backbone) and bead pairs with scHi-C interactions (constraint) were given a flat-bottomed harmonic potential force with a scaling factor of 25 (k2) around an effective target distance (deff) of 150 nm or 120 nm (dtarget) for backbone and constraint bonds, respectively, scaled by the inverse of the square-root of the number of observed valid reads (r) supporting an interaction (backbone bonds were always given a distance scaling factor of one). At distances less than 15% of dtarget (dlower) for constraint bonds (there was no lower limit for backbone bonds, thus dlower equaled 0), an exponential repulsive force was applied. At distances between dtarget and dtarget + 30 nm (dupper), an exponential attractive force was applied. At distances greater than dupper, the attractive force became linear.

$$d_{eff} = \frac{d_{target}}{\sqrt{r}}$$

$$F_{bond} = \begin{cases} k_2\left(d_{lower} - d\right)^2 & d < d_{lower} \\ 0 & d_{lower} \leq d < d_{eff} \\ k_2\left(d - d_{eff}\right)^2 & d_{eff} \leq d < d_{upper} \\ k_2\left[\left(d_{upper} - d_{eff}\right)^2 + 2\left(d_{upper} - d_{eff}\right)\left(d - d_{upper}\right)\right] & d_{upper} \leq d \end{cases}$$

Simulations were run using OpenMM version 7.1.1 and wrapped using the Mirny lab's openmm-polymer (https://bitbucket.org/mirnylab/openmm-polymer). Specific forces were custom implemented and available in the accompanying code. Initial model conformations generated by randomly ordering chromosomes, end to end, and treating all beads as a single polymer. Beads were arranged around a 3 µm circle, evenly spaced along 5 oscillations of a sine wave perpendicular to the plane of the circle with an amplitude of 1.5 µm. Each simulation was run for 301 time steps, each consisting of 1000 motion steps. For the first 101 time steps, the temperature was linearly ramped from 10000 K to 5000 K. At the same time, the k2 parameter for constraint bonds was ramped from 0 to 25. During the remaining 200 time steps, the temperature was linearly ramped down from 5000 K to 10 K. Each simulation was repeated 10 times and the resulting model with the fewest bonds exceeding their effective target lengths was selected for downstream analysis.

For each scHi-C cell model, a hull was constructed based on polymer bead positions. Initially, for each chromosome, the set of distances for that chromosome's beads from the chromosome's mean bead position was calculated. The standard deviation across all sets of chromosome distances was determined and any beads whose distance exceeded 3 standards of deviation was removed from the set used to determine the nuclear hull. For each chromosome, the valid beads were used to construct a convex hull. The nuclear hull was defined as the union of all chromosome hulls.

For each bead, a ray was projected from the hull center of mass, through the bead position. Next, the longest distance from the center of mass position to an intersection with the nuclear hull was found. Because nuclear hulls were not guaranteed to be convex, the ray could intersect the hull multiple times. Only the furthest distance was used. The radial position was defined as the bead distance from the center of mass divided by the projection intersection distance from the center of mass. In the case of outlier beads excluded from the hull-defining set, if the bead distance exceeded the projection distance, the radial position was defined as one.

Model compaction was determined from scHi-C models by examining every chromosome bead triplet and if all three beads were in the same state (in or out of a LAD), calculating the distance between the end beads.

2.10 Figures

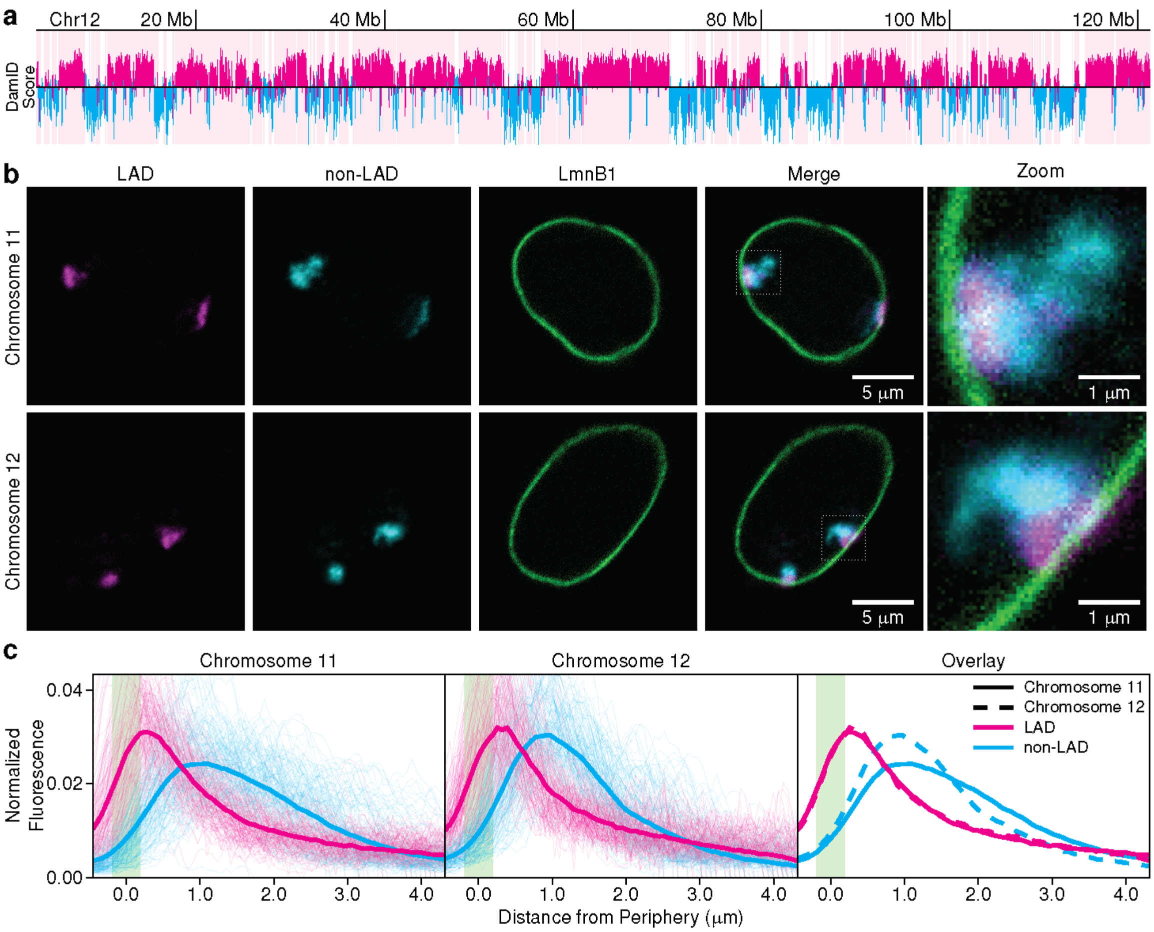

Figure 2.1. LAD definition and design of novel sub-chromosome compartment oligonucleotide paints. (A) LmnB1 DamID $\log_2$ ratio plots for chromosomes 11 and 12 and LADs (solid pink bars) called by LADetector. (B) 3D-immunoFISH probes (chromosome conformation paints) in single primary wild-type non-treated MEF nuclei reveal chromosome organization and the presence of LAD and non-LAD subdomains for both chromosome 11 and chromosome 12. (C) Continuous measurements for chromosome 11 (n=510) and 12 (n=50) plotted to show the distributions of the LAD (magenta) and non-LAD (cyan) signals, as measured from the lamina (x=0, green), single cell measurements are shown as thin lines, average as thick lines.

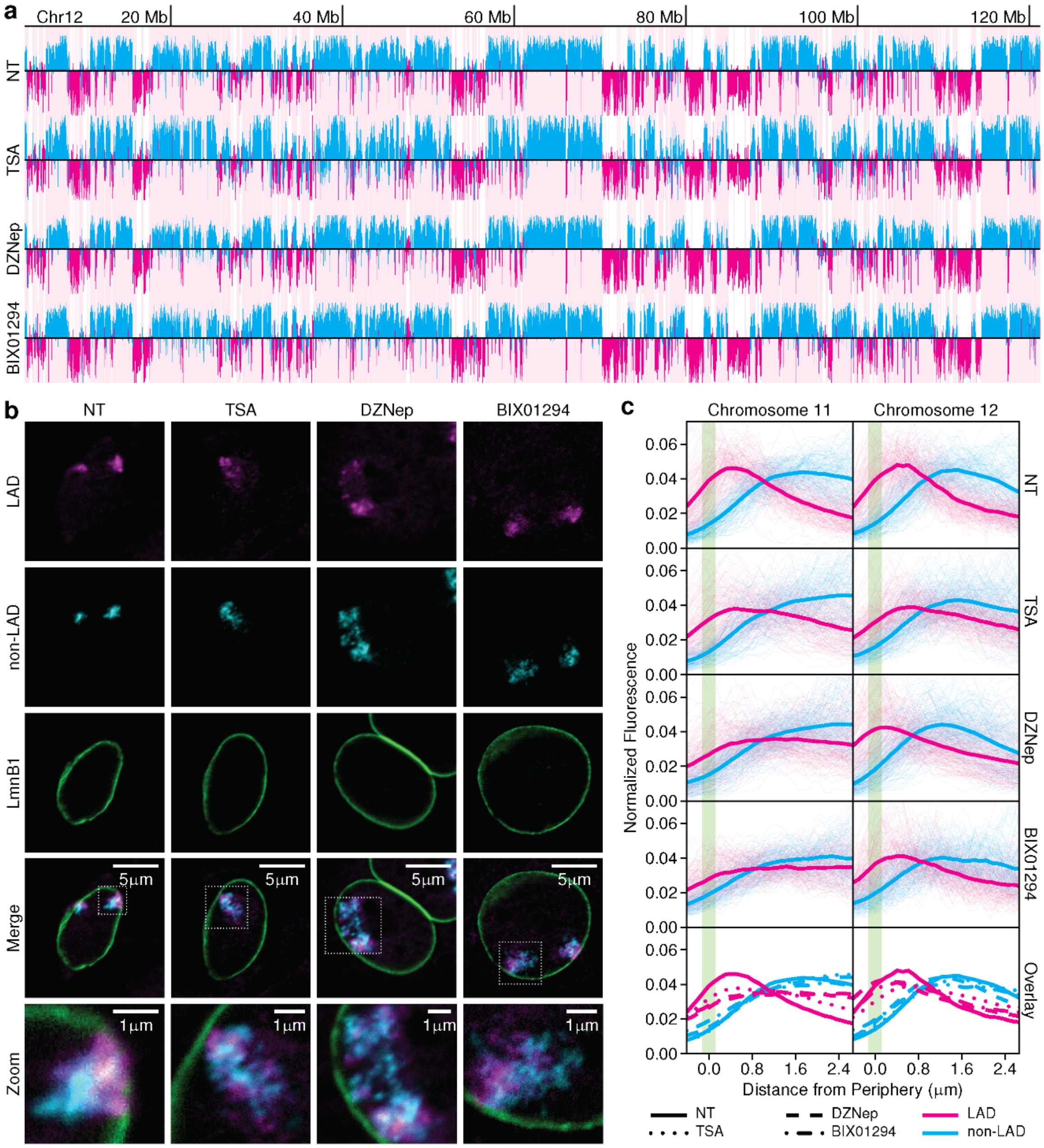

Figure 2.2. Epigenetic perturbation and sub-chromosomal architecture. (A) Chromosome 12 LmnB1 DamID signal for wild-type primary wild-type non-treated (NT)(WT) and drug-treated cells are shown with non-treated WT LAD calls indicated by pink bars and magenta signal. NT non-LAD signal is represented in cyan. (B) 3D immunoFISH signals of LADs and non-LADs for wildtype and cells treated with TSA, DZnep, or BIX01294 in chromosome 12 show perturbation of sub-territory

organization. (C) Individual measurements show distributions of LAD (magenta) and non-LADs (cyan) relative to laminB1 (x=0, green). Individual measurements of chromosome territories are shown as thin lines for NTWT (See figure 1; Chr11 n=510, Chr12 n=50), TSA treated (Chr11 n=52, Chr12 n=51), DZNep treated (Chr11 n=52, Chr12 n=54) and BIX01294 treated nuclei (Chr11 n=27, Chr12 n=15). Overlays of distributions for chromosomes 11 and 12 are provided in bottom two graphs.

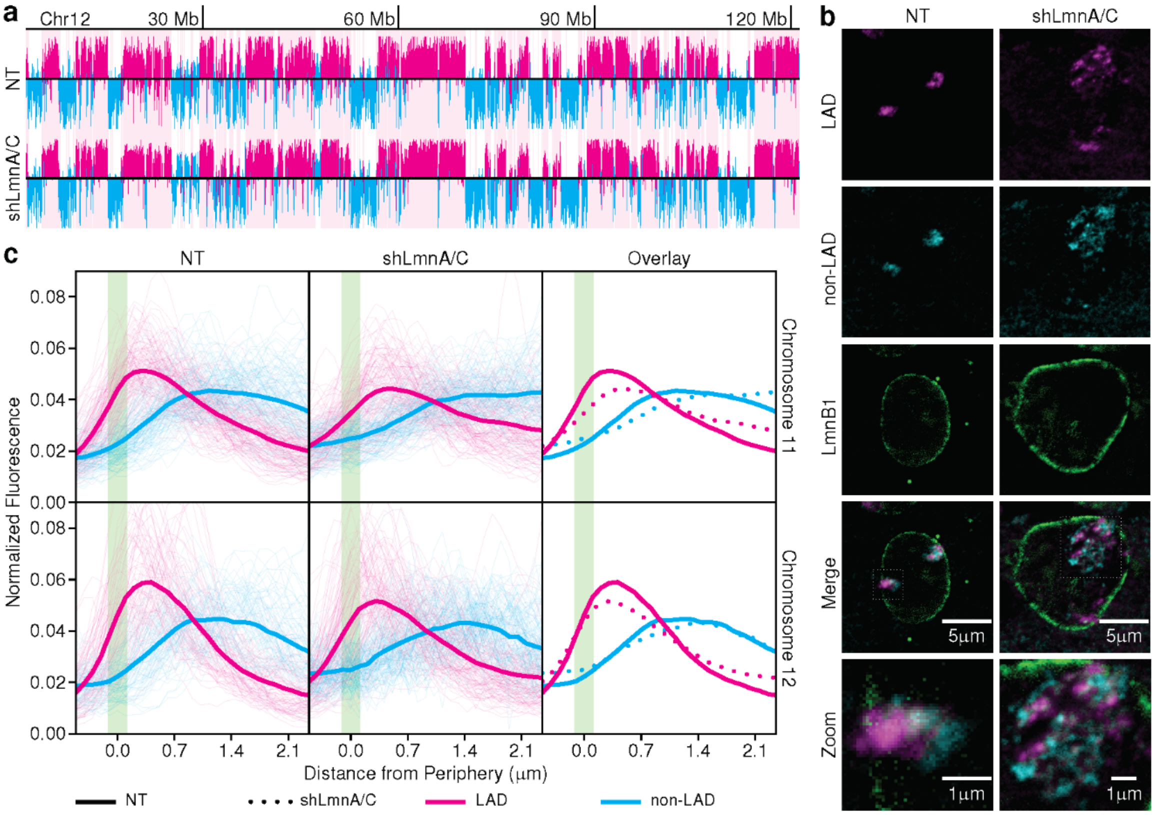

Figure 2.3. Nuclear structure integrity and sub-chromosomal architecture. (A) LmnB1 DamID data for primary wWild-type non-treated (NWT) vs LaminA/C knockdown for chromosome 12. NTWT LAD calls are indicated by pink bars and magenta signal. NTWT non-LAD signal is represented in cyan. (B) 3D immunoFISH signals of LADs (magenta) and non-LADs (cyan) in NTWT and LaminA/C knockdown highlight chromosome 12 sub-territory organization after LaminA/C knockdown. (C) Continuous measurements for NWT (Chr11 n=44, Chr12 n=28) and LaminA/C (Chr11 n=60, Chr12 n=67). Individual measurements show distributions of LAD (magenta) and non-LADs (cyan) relative to LmnB1 (x=0, green). Individual measurements of chromosome territories are shown as thin lines. Overlays of distributions for chromosomes 11 and 12 are provided in bottom two graphs.

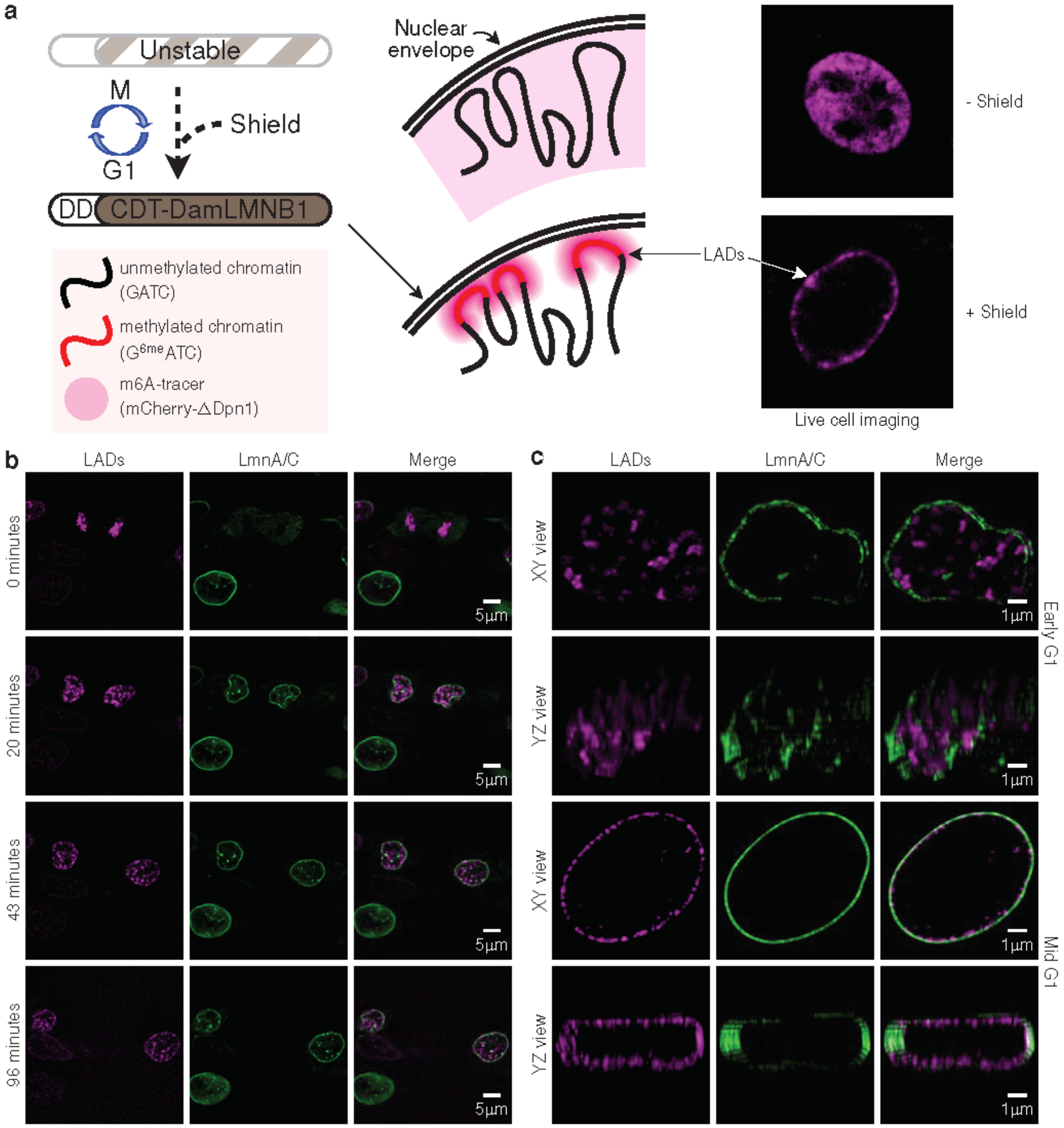

Figure 2.4. LAD self-aggregation occurs prior to peripheral localization, with lamina localization resolving by late G1. (A) A modified m6A tracer system. Dam-LmnB1 construct containing the ubiquitination domain from cdt1 and a destabilization domain (DD) enables restriction of its stable expression to G1-phase of the cell cycle in the presence of a stabilizing reagent (Shield 1) for discrete labeling of adenines during G1. Similar to the previous system, a DpnI construct without a functional cleavage domain coupled to an mCherry (red) fluorophore (magenta) allows

visualization. Representative images + and - Shield. (B) Live cell images of LADs/B compartment shown in magenta (m6A tracer), shows a progression through early G1 for 96 min with the start of early G1 marked as 0 min. The nuclear periphery is shown in green using single chain antibody against lamin (GFP-scfv Lamins). (C) Super resolution microscopy of LADs using m6A tracer system in early G1 cell and mid G1 nuclei.

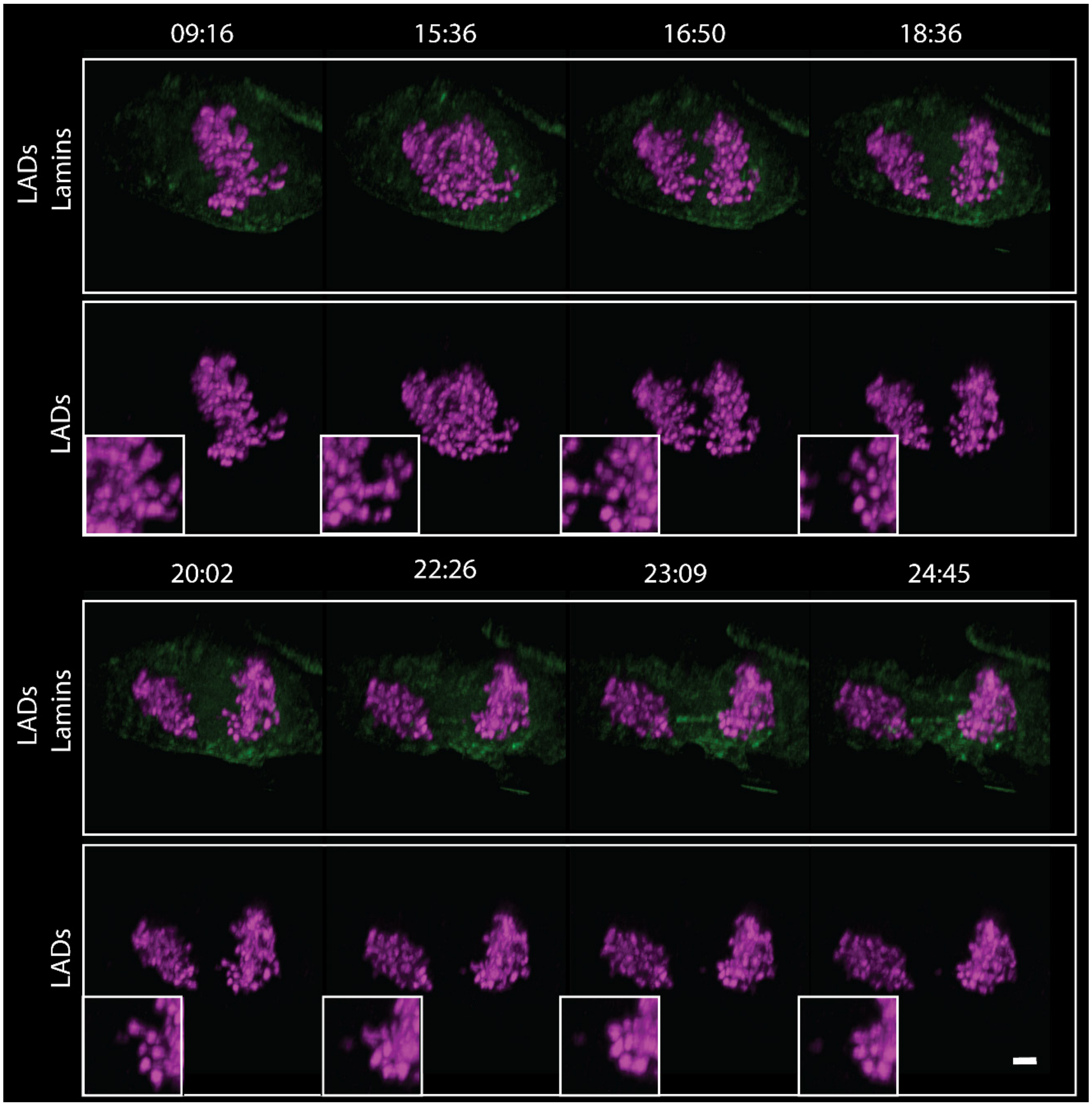

Figure 2.5. Compartments intercalate during mitosis and begin separating during anaphase (A) Stills from live cell time lapse superresolution imaging of m6A tracer (magenta) and single chain antibody to lamins (green) through mitosis. Scale bar is 2μm.

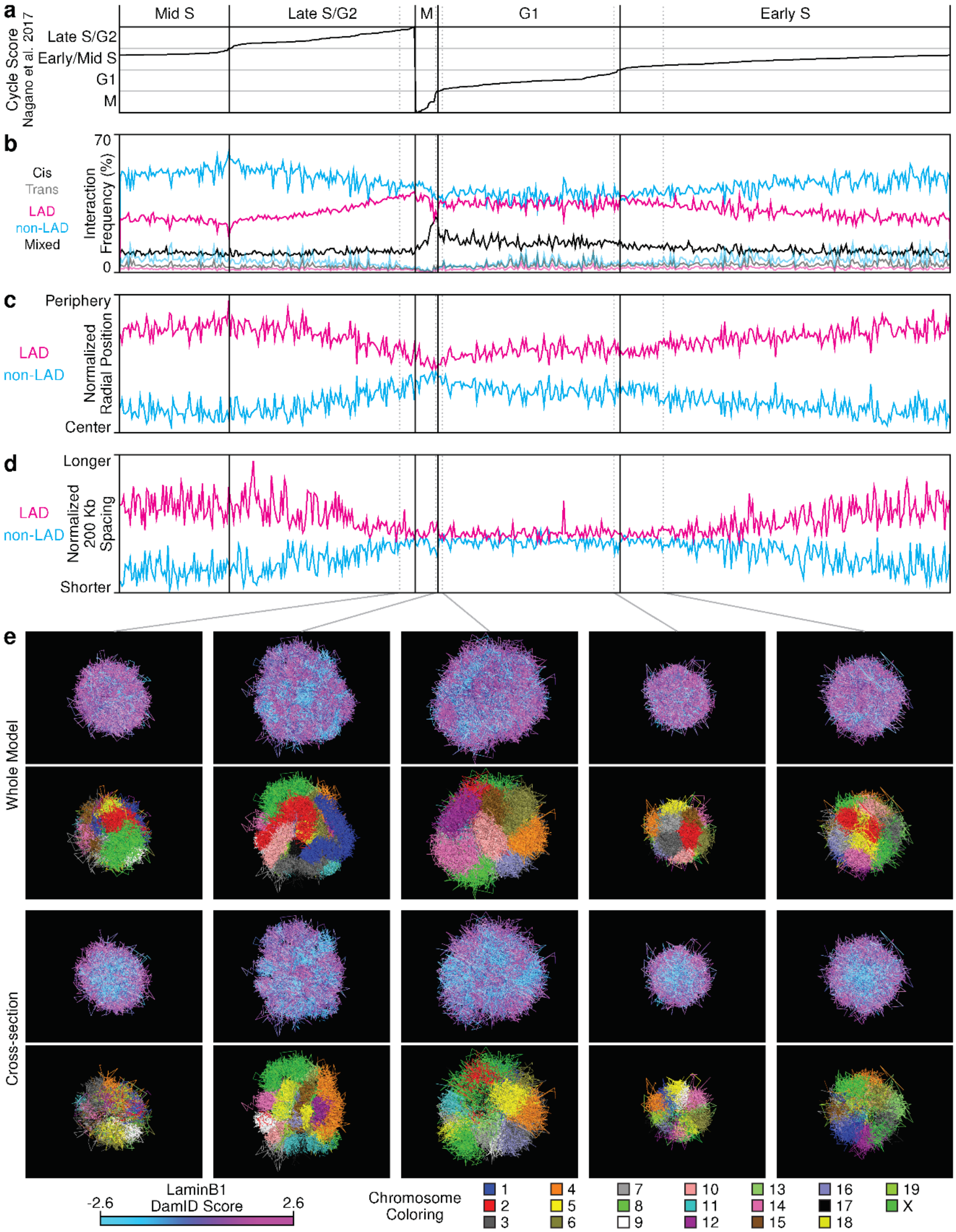

Figure 2.6. Modeling of single-cell Hi-iC data. (A) Cell cycle scores for high-coverage haploid cells taken from Nagano et al. (2017). (B) Interaction frequency broken into groups by LAD/non-LAD and within chromosome (cis)/between chromosome (trans) features. (C) Mean radial position of

LAD and non-LAD 100Kb windows from scHi-C models, normalized by the mean radial position for all windows for each cell. (D) Mean distance between sequence windows 200 Kb apart (midpoint to midpoint) and within the same LAD or non-LAD region as derived from the scHi-C models. Scores were normalized by the mean spacing across all 200 Kb-separated window pairs for each cell. (E) Exemplar models for different phases of the cell cycle, colored to show either the DamID score (1st and 3rd rows) or indicate chromosome identity (2nd and 4th rows). The top two rows show whole models while the bottom two show cross-sections of the same models.

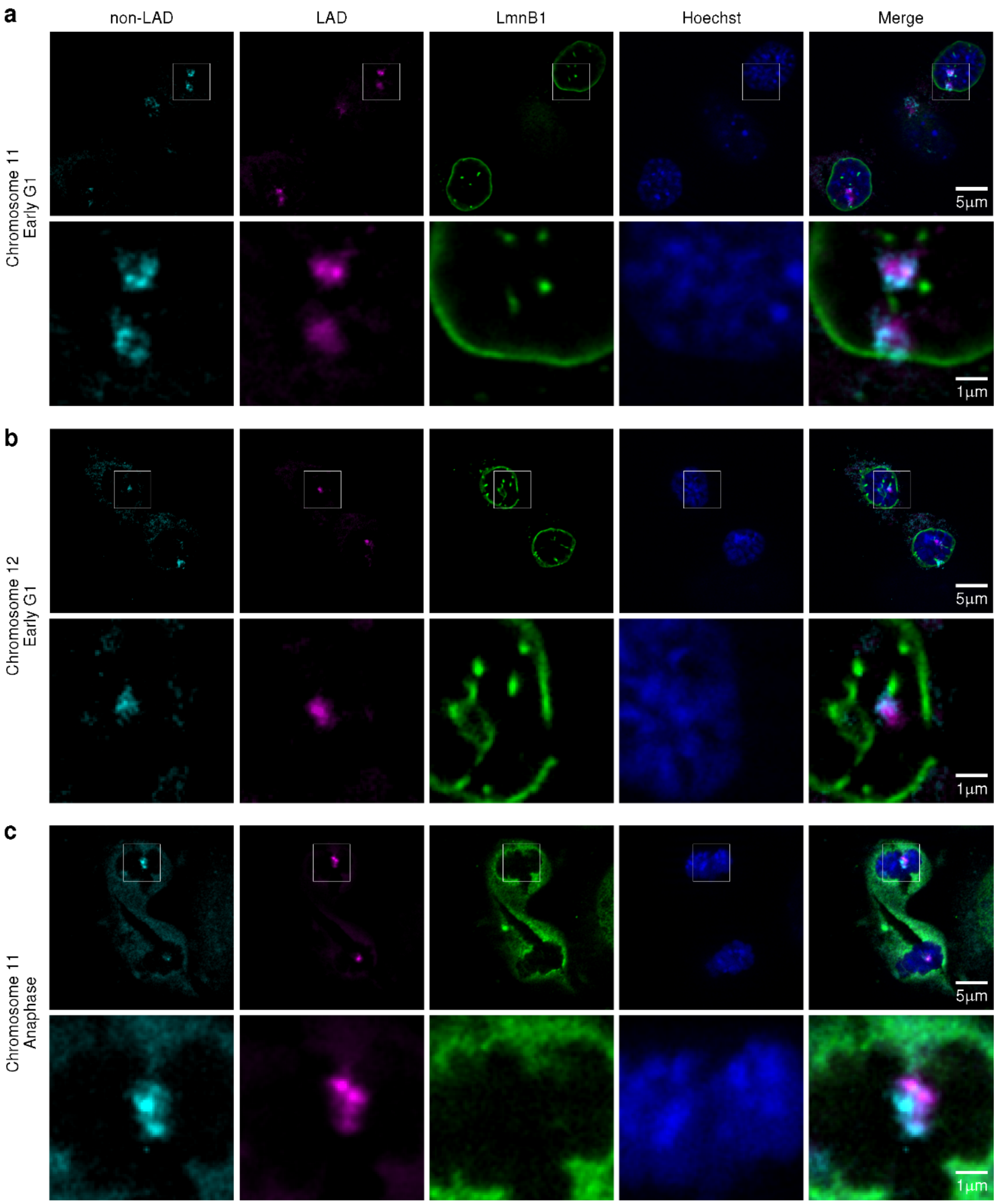

Figure 2.7. LAD/B-compartment aggregates are from single chromosomes. (A and B) Chromosome conformation paints in primary wild-type MEF cells of chromosomes 11 and 12 in early G1 and (C) chromosome 11 in anaphase primary MEF cells showing non-LADs (cyan), LADs (magenta), laminB1 (green), and DNA (Hoechst).

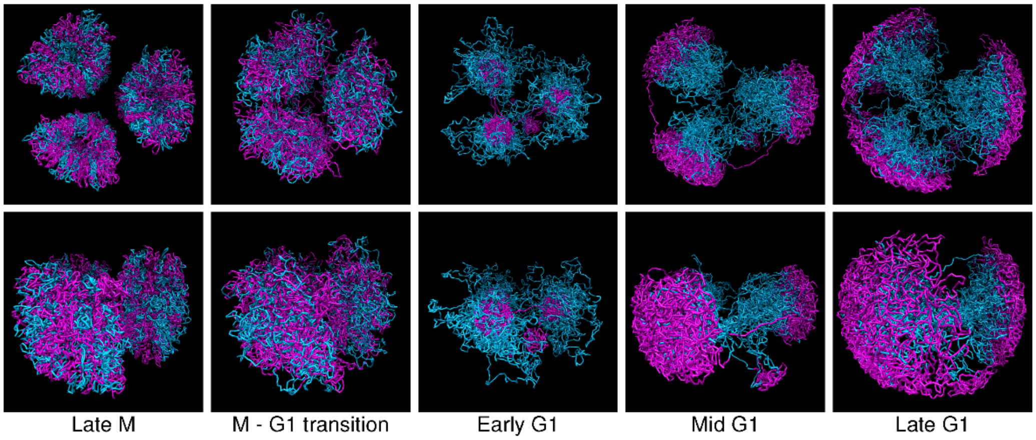

Figure 2.8. Model of compartment dynamics through mitosis and G1. A three chromosome cartoon nucleus demonstrating the proposed sequence of events following mitosis for the LAD (magenta)/non-LAD (cyan) spatial partitioning seen during the majority of the cell cycle. The two rows show a top and side view of the same process.

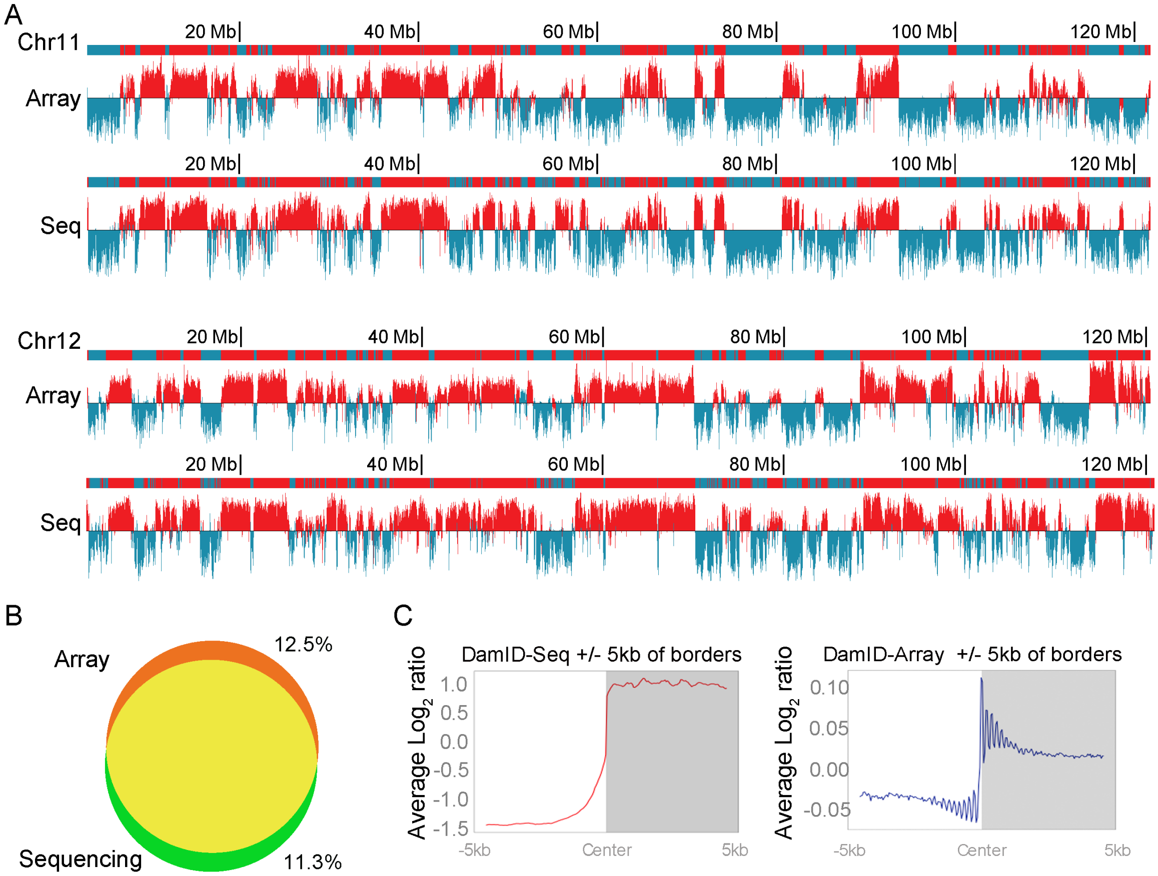

Supplemental Figure 2.1. Comparison of DamID-array and DamID-seq. (A) Lamina-chromatin contact maps derived from DamID-array (top) or DamID-seq (bottom) for chromosome 11 and 12 arranged for visual comparison. (B) Venn diagram features overlap of LADs defined by DamID-seq and DamID-array, <13% are unique between techniques, similar to differences observed between replicate experiments (see text). (C) Plots of the average log2 ratios of DamID-seq signals (red line) and DamID-array signals (blue line) outside (white box) and inside (gray box) LAD regions. Region shown is +/- 5 kb of a LAD border.

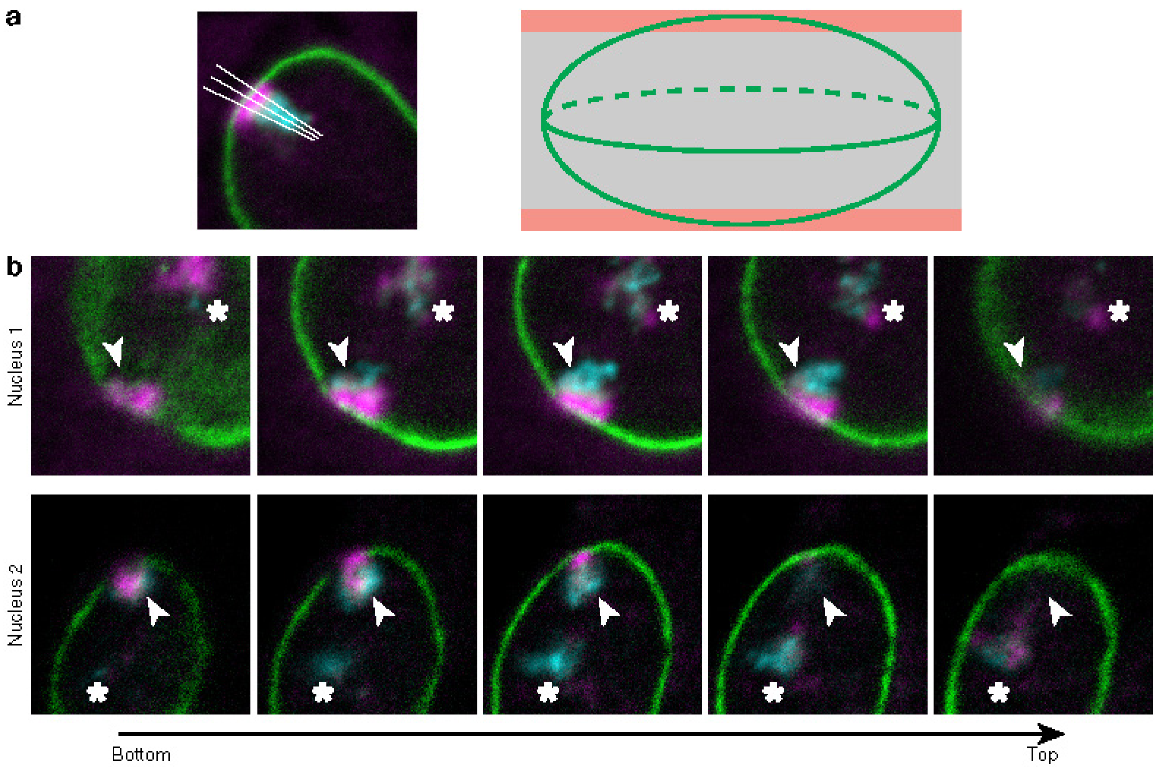

Supplemental Figure 2.2. Scoring methodology. (A) Line scan measurements to collect distribution of LAD and non-LAD sub-territories from the lamina were done by collecting three measures across the chromosome territory, from the lamina through the chromosome territory, passing through the shortest distance of lamin signal to LAD signal. Measurements were taken in the medial planes, highlighted gray shaded area of nucleus schematic. Only territories that had the majority of their LAD signal (magenta) in the medial planes were scored, since scoring of territories with the majority of signal at the top/bottom of nucleus would have required scoring in the lower resolution axial (Z) dimension, which would have skewed measurements. (B) Examples of territory disposition in the nuclear volume are shown. Two nuclei are presented as 5 slices, from top toward the bottom of the nucleus. The territory that was scored in medial planes is indicated with an arrow head. Territory that was not scored is starred, because the majority of the LAD signal was at the top or bottom of the nucleus. Line scans were done in single or multiple planes, depending upon the disposition and intensity of LAD signals.

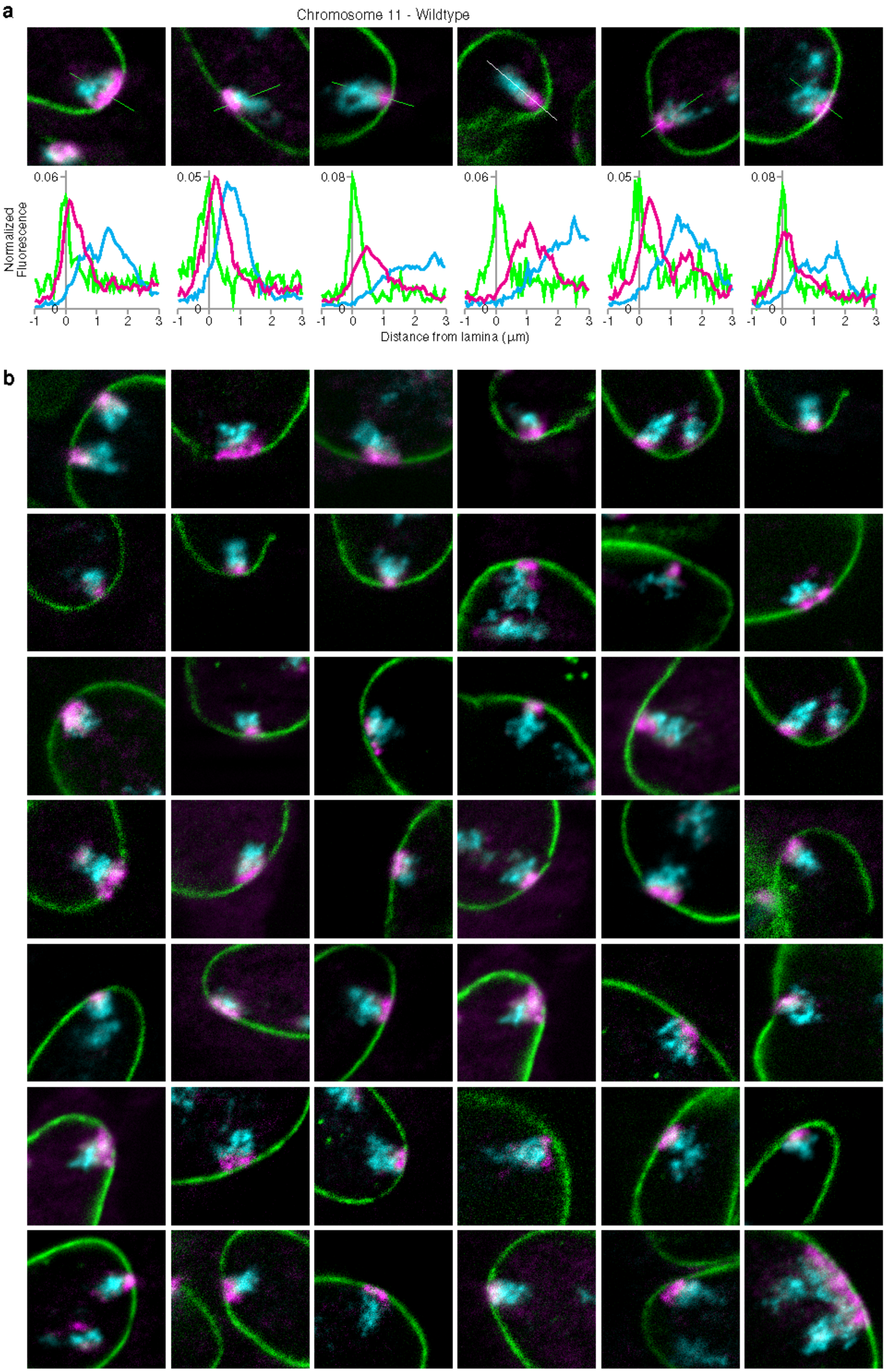
a
Chromosome 11 - Wildtype
0.06
0.05
0.08
0.06
0.05
0.08
Normalized Fluorescence
0
-1 0 1 2 3
Distance from lamina (μm)
b

Supplemental Figure 2.3. Chromosome conformation paints for chromosome 11. (A) Examples of single line scan measurements (green line overlaid on chromosome territory) with accompanying plot profiles (graphs, below) for LADs (magenta) non-LADs (cyan) and LmnB1 (green). (B) Array of chromosome 11 territories visualized by chromosome conformation paints. All images are shown at the same magnification. All graphs include measurements to 32 µm from the lamina.

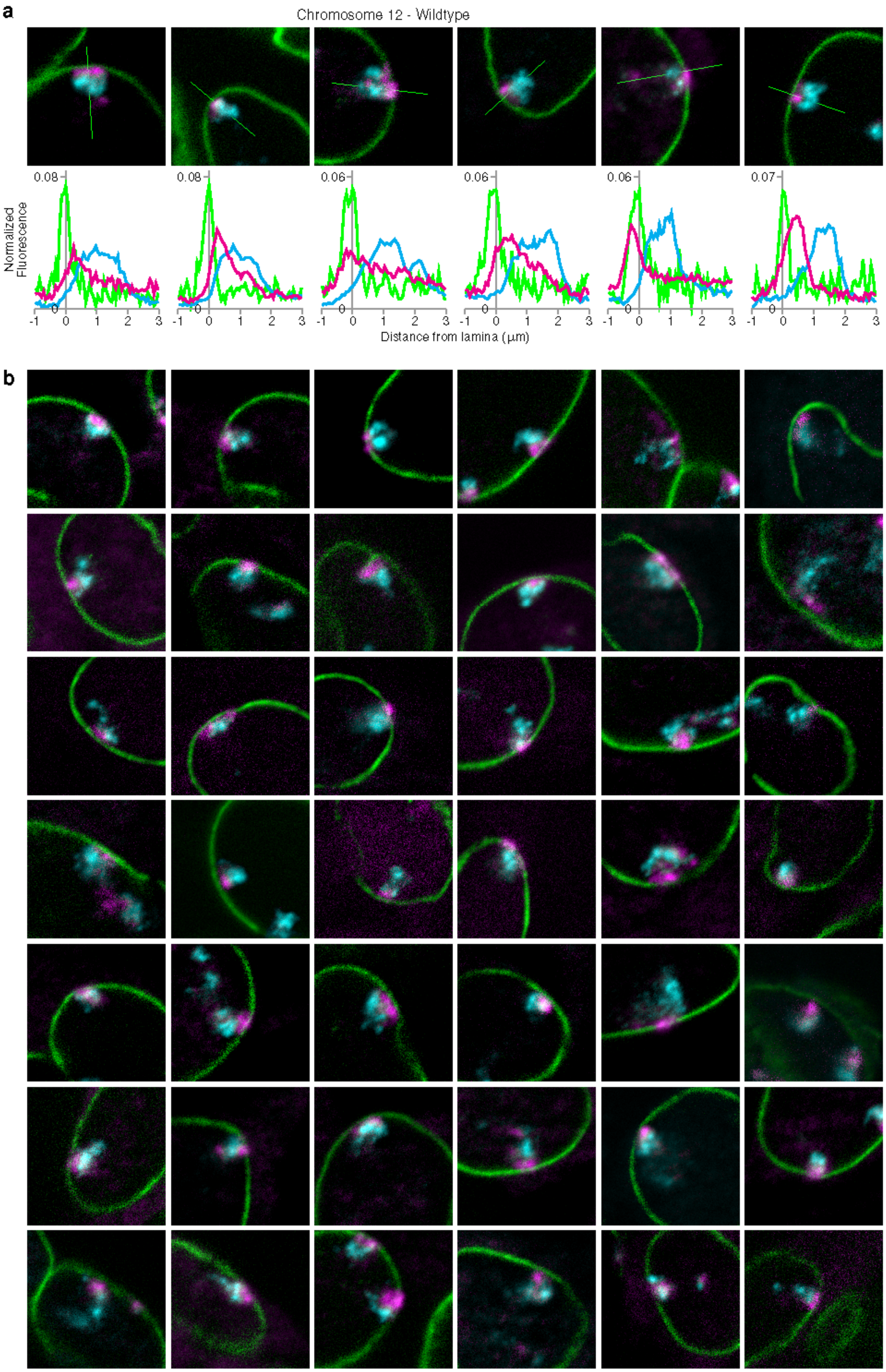
a
Chromosome 12 - Wildtype
Normalized Fluorescence
0.08
0.08
0.06
0.06
0.06
0.07
0
-1
0
1
2
3
Distance from lamina (µm)
b

Supplemental Figure 2.4. Chromosome conformation paints for chromosome 12. (A) Examples of single line scan measurements (green line overlaid on chromosome territory) with accompanying plot profiles (graphs, below) for LADs (magenta) non-LADs (cyan) and LmnB1 (green). (B) Array of chromosome 12 territories visualized by chromosome conformation paints. All images are shown at the same magnification. All graphs include measurements to 32 µm from the lamina..

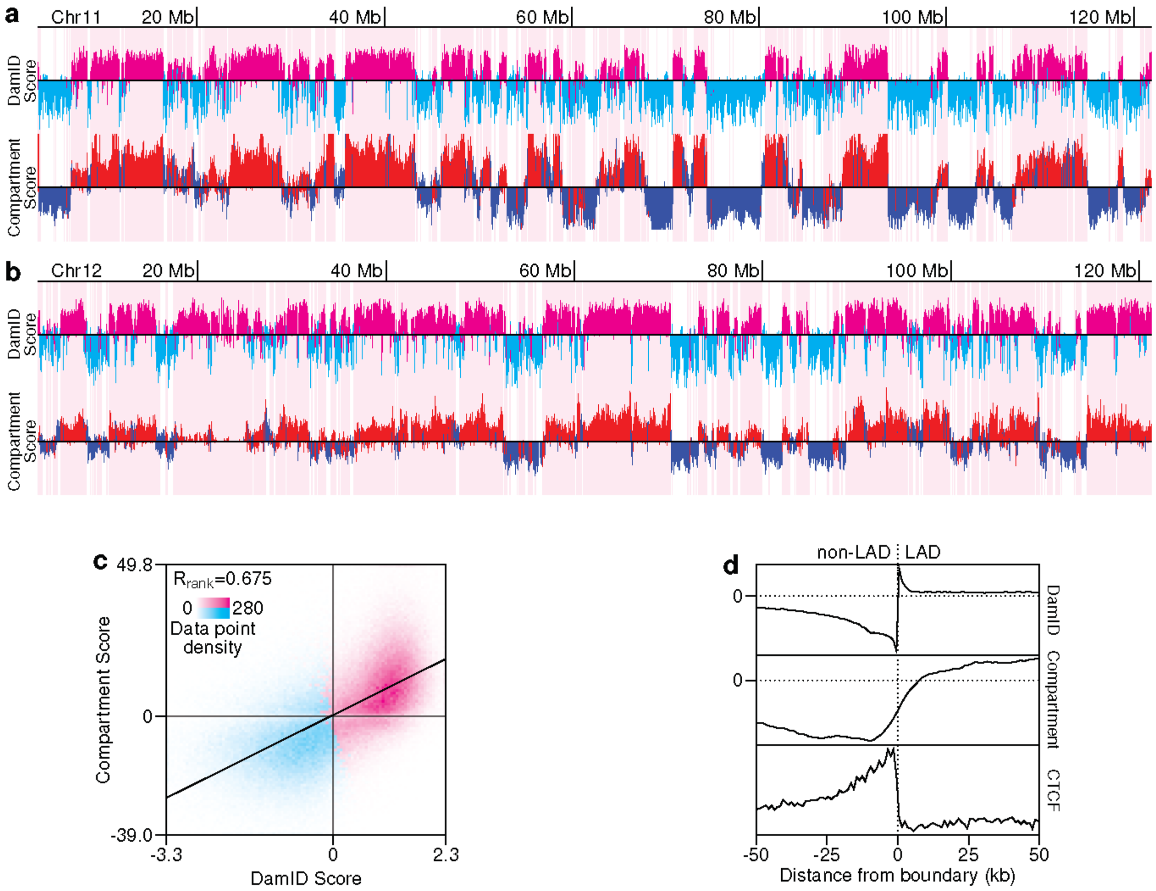

Supplemental Figure 2.5. LAD structures captured by both local and chromosome-wide metrics from Hi-C data. (A) LmnB1 DamID and Hi-C compartment score from chromosome 11 in MEF cells. LAD calls and associated data are highlighted in magenta/red (DamID/compartment scores) while data from non-LAD regions are shown in cyan/blue. (B) LmnB1 DamID and Hi-C compartment score from chromosome 12 in MEF cells. LAD calls and associated data are highlighted in magenta/red (DamID/compartment scores) while data from non-LAD regions are shown in cyan/blue. (C) Genome-wide correlation between DamID and compartment scores. Data are partitioned into a 100 by 100 grid with intensity indicating data density and color showing whether the majority of the bins data points are in LADs (magenta) or not (cyan). (D) Feature profiles anchored at all boundaries of LADs of size 100 kb or greater (excluding chromosome X) and oriented from non-LAD (left) to LAD (right). Profiles consist of data within 100 kb of each boundary binned in 1 kb intervals.

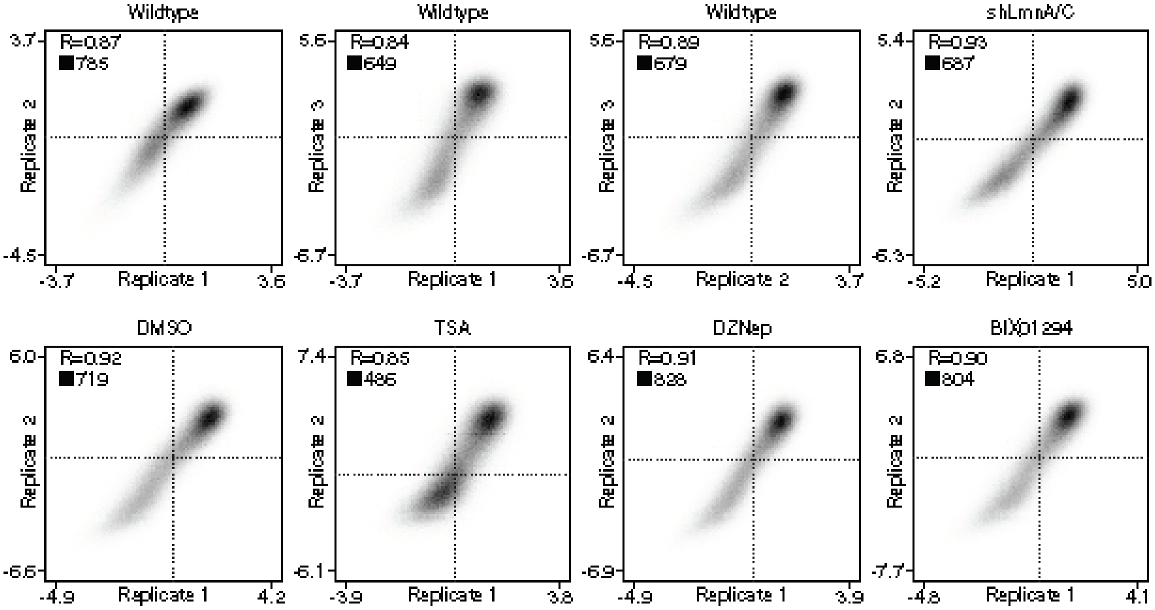

Supplemental FIgure 2.6. Correlation of DamID runs. Pairwise comparison of replicate LmnB1 DamID scores within each experimental condition. For each comparison, the Pearson correlation coefficient (R) is shown.

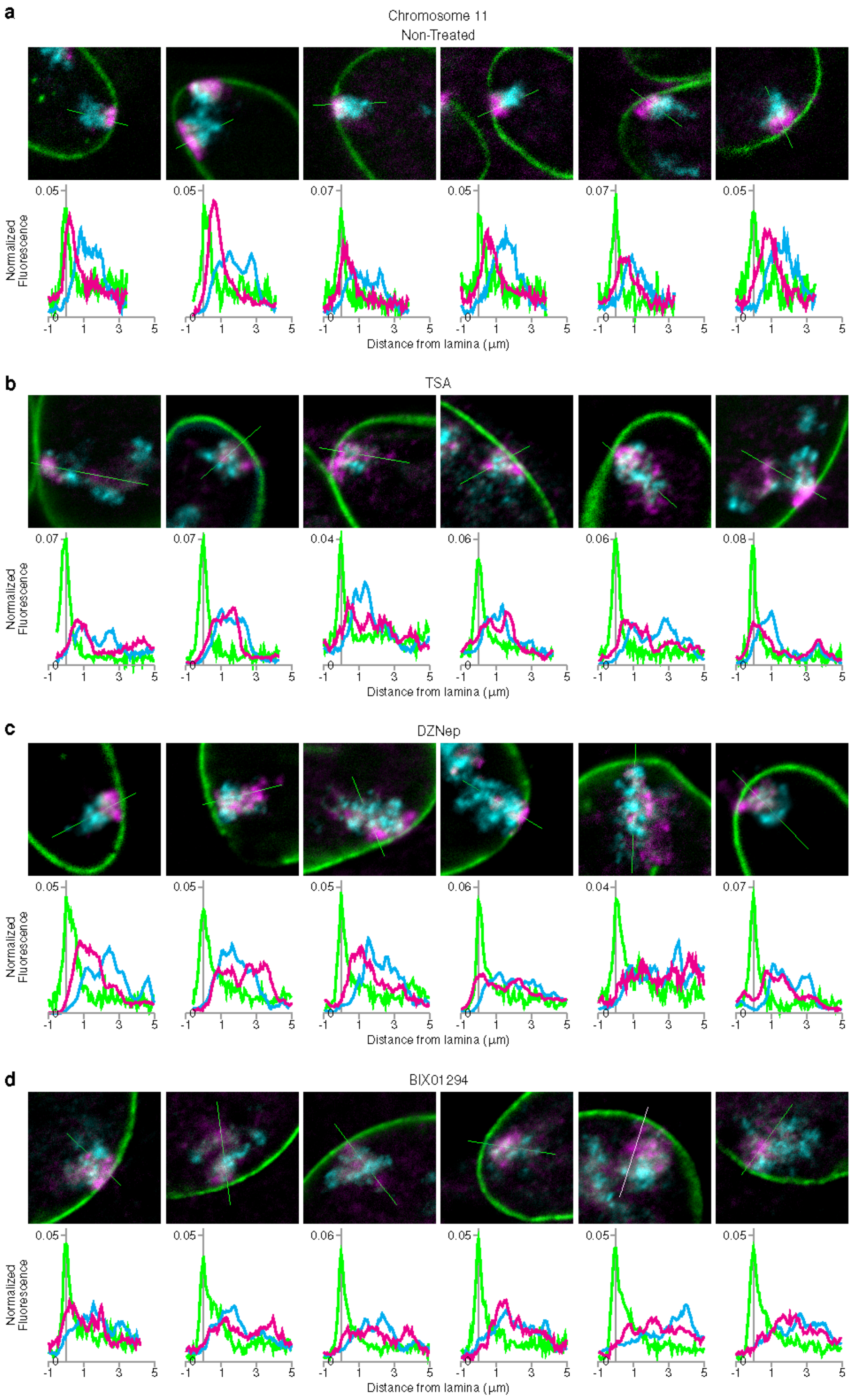
a
Chromosome 11
Non-Treated
Normalized Fluorescence
0.05
0.05
0.07
0.05
0.07
0.05
-1 0 1 3 5
Distance from lamina (μm)
b
TSA
0.07
0.07
0.04
0.06
0.06
0.08
Distance from lamina (μm)
c
DZNep
0.05
0.05
0.05
0.06
0.04
0.07
Distance from lamina (μm)
d
BIX01294
0.05
0.05
0.06
0.05
0.05
0.05
Distance from lamina (μm)

Supplemental Figure 2.7. Chromosome 11 conformation profiles after epigenetic perturbation. Example single line scans are presented for non-treated (A), TSA-treated (B), DZNep-treated (C), and BIX01294-treated (D). Region measured is indicated over the chromosome territory (green overlay line, top) and plotted distribution of LAD, non-LAD, and LmnB1 are shown below (magenta, cyan, and green lines, respectively). All images are shown at the same magnification. All graphs include measurements to 52 μm from the lamina.

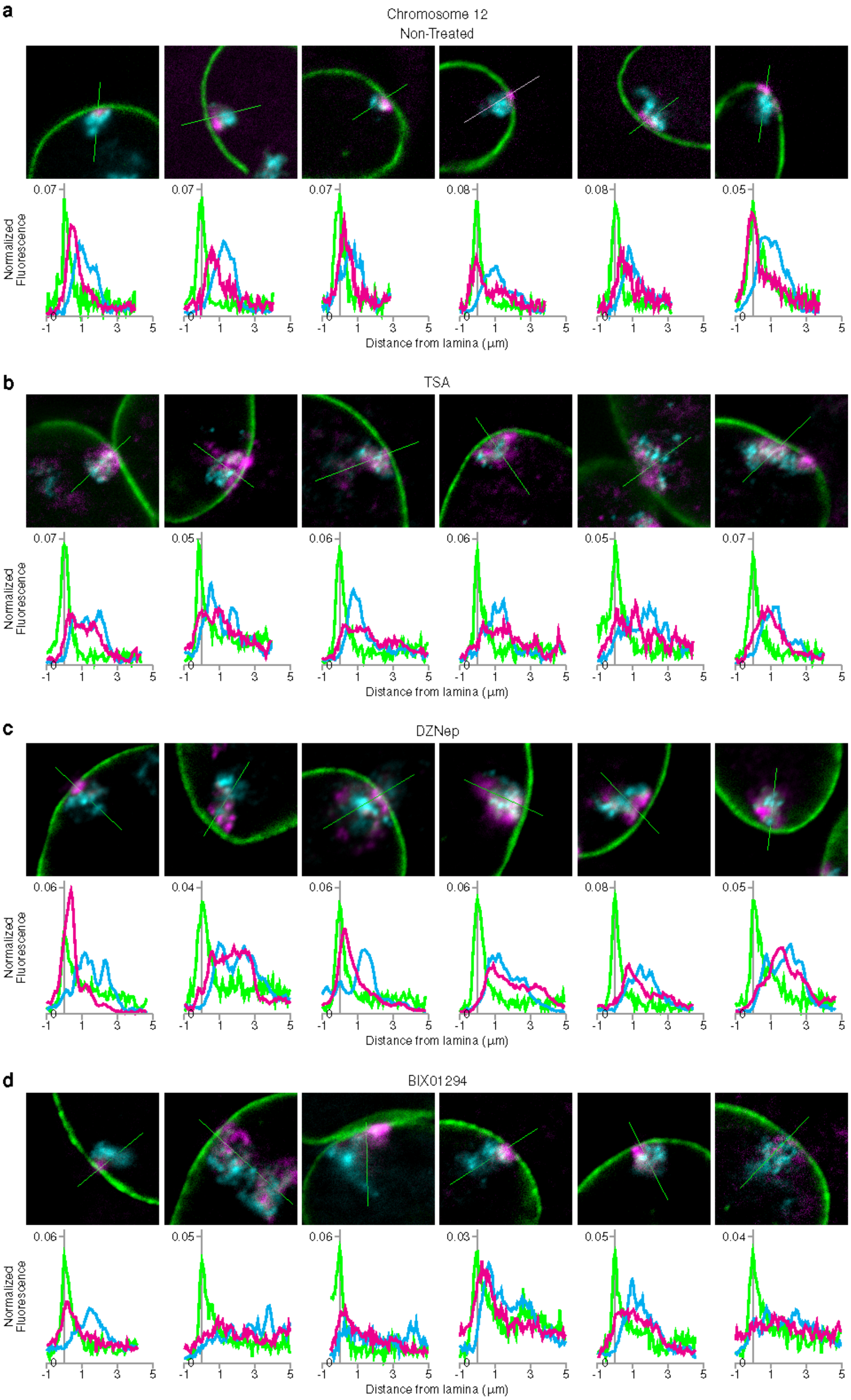
a
Chromosome 12
Non-Treated
0.07
0.07
0.07
0.08
0.08
0.05
Normalized Fluorescence
0
-1
1
3
5
Distance from lamina (μm)
b
TSA
0.07
0.05
0.06
0.06
0.05
0.07
Normalized Fluorescence
Distance from lamina (μm)
c
DZNep
0.06
0.04
0.06
0.06
0.08
0.05
Normalized Fluorescence
Distance from lamina (μm)
d
BIX01294
0.06
0.05
0.06
0.03
0.05
0.04
Normalized Fluorescence
Distance from lamina (μm)

Supplemental Figure 2.8. Chromosome 12 conformation profiles after epigenetic perturbation. Example single line scans are presented for non-treated (A), TSA-treated (B), DZNep-treated (C), and BIX01294-treated (D). Region measured is indicated over the chromosome territory (green overlay line, top) and plotted distribution of LAD, non-LAD, and LmnB1 are shown below (magenta, cyan, and green lines, respectively). All images are shown at the same magnification. All graphs include measurements to 52 μm from the lamina.

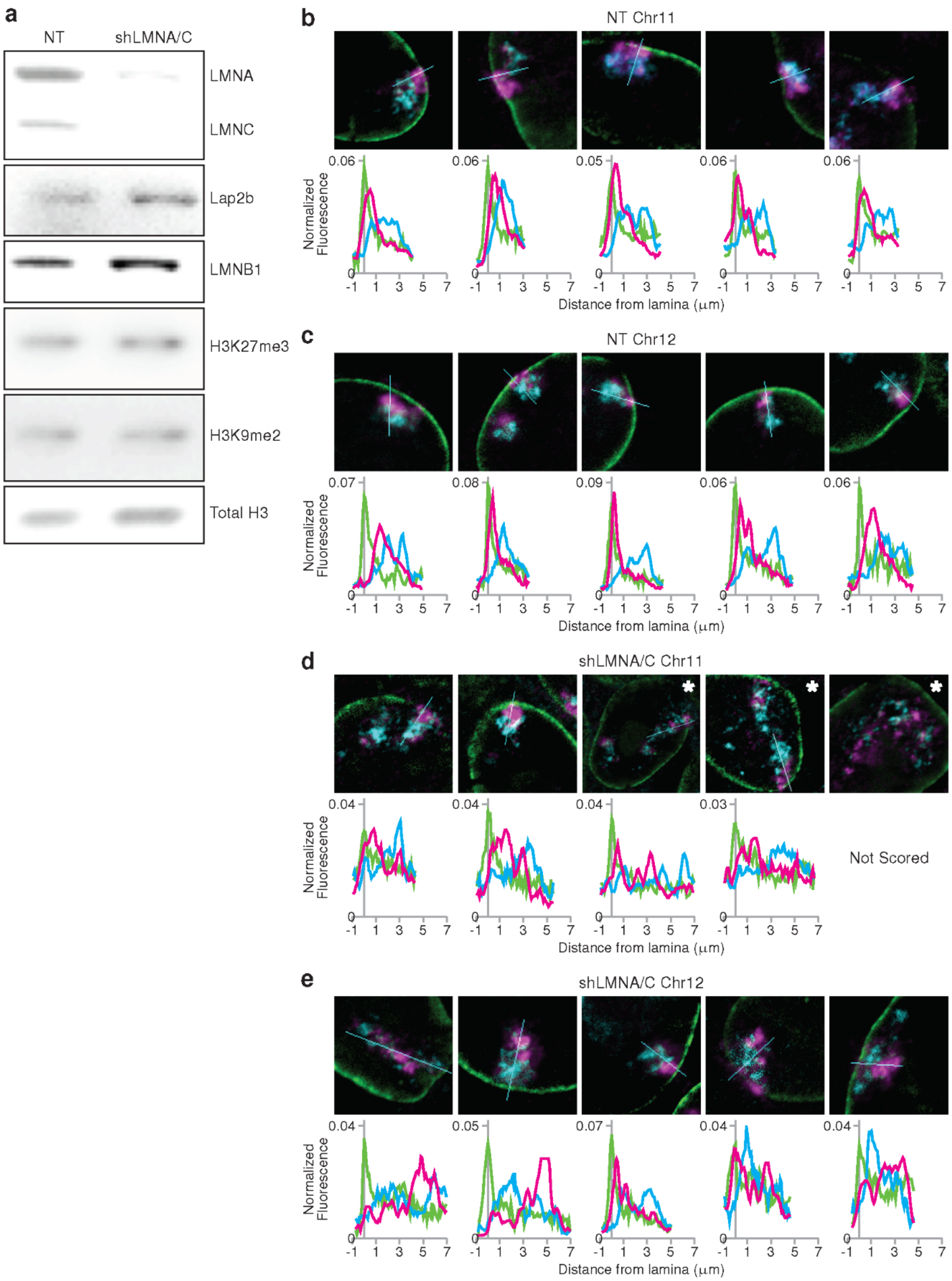

Supplemental Figure 2.9. Chromosomes 11 and 12 conformation profiles after shRNA-mediated LmnA/C knockdown. Example single line scans are presented for non-treated (NT) (BA) and shRNA-mediated LmnA/C knockdown (shLmnA/C) (CB). Region measured is indicated over the chromosome territory (green overlay line, top) and plotted distribution of LAD, non-LAD, and LmnB1 are shown below (magenta, cyan, and green lines, respectively). Images are shown at the same magnification with the exception of starred images which are 2X zoomed out to encompass the measured territory. All graphs include measurements to 72 µm from the lamina. (AC) Immunoblot for the indicated proteins or histone modifications in NT and shLmnA/C cells.

Chapter 3: Lamin C is required to establish genome organization after mitosis

3.1 Introduction

Lamins encoded by LMNA, LMNB1 and LMNB2 form networks of nuclear intermediate filaments as major components of the nucleoskeleton. Lamin filaments interact with key partners, including most nuclear membrane proteins, to form nuclear lamina networks that determine nuclear mechanics, modulate signaling and dynamically organize the genome [11,99–103]. Lamina networks interact with large regions of transcriptionally-silent heterochromatin in each cell type and customize the 3D configuration of individual chromosomes with respect to the nuclear envelope (NE). These silent heterochromatin regions, identified operationally as Lamina Associated Domains (LADs), correspond to the 'B' compartment identified via HiC and related chromatin mapping strategies [8,12,104]. Chromatin association with the lamina, and its opposite (dynamic release as active 'non-LAD' or A-compartment chromatin) are particularly important for developmentally-regulated genes needed to create or maintain cell-specific identity [8,19,22,38]. 'Silent' histone modifications including H3 lysine 9 methylation (H3K9me2/3) and H3 lysine 27 trimethylation (H3K27me3), are key components of LAD organization [11,13,71,105,106]. We previously found that A-type lamins, encoded by LMNA, establish and/or maintain interphase LAD configuration

[11,23]. In recent years there have been further advances in understanding how LADs, chromatin looping, epigenetic modifications and liquid-liquid phase transitions of chromatin during interphase are interrelated [4,11,13,16,18,71,100,101,103–109].

In contrast, the mechanisms by which nuclear 3D structural information is faithfully transmitted and re-established through cell division are of significance and remain largely unknown. During entry into mitosis, interphase spatial genome and NE organization are lost as chromosomes condense and the NE and nuclear lamina networks disassemble, yet global chromosome and 3D-genome organization is re-established in the next interphase [8,12,46,71,110–115] . As cells enter anaphase, both super-resolution imaging and single cell Hi-C (a genome-wide methods to detect chromatin contacts) showed that LAD regions of chromosomes begin to self-aggregate as globular 'compartments' prior to nuclear lamina formation [12].These LAD agglomerates slowly make their way to the nascent NE during early G1 and ultimately 'spread' across the lamina as they approach and interact with the nuclear periphery [12].

One key protein in interphase LAD organization and NE function are the A type lamins. Alternative mRNA splicing of LMNA produces two main somatic isoforms, lamin A and lamin C, the first 566 or 568 residues of which are identical in human and mice, respectively [116]. Lamin C has six unique C-terminal residues, whereas lamin A has an extended tail domain that undergoes four post-translational modification steps to achieve its final mature length of 646 or 647 residues, in humans and mice respectively [117]. Until recently lamin A and lamin C were assumed to be functionally redundant.

Super-resolution microscopy show lamins A, C, B1 and B2 form separate but structurally inter-dependent filament networks such that removing any one (e.g. lamin C) affects the distribution and geography of the other three [24,25,35].In addition to forming separate networks, several lines of evidence suggest that these isotypes might have unique roles in cellular function. For instance,lamin A specifically confers mechanical stiffness that determines when different white blood cell lineages exit the bone marrow. In contrast, in CNS neurons lamin C is the predominant A-type lamin isoform expressed due to the selective down-regulation of the prelamin A transcript by miR-9 [118–120]. Studies in mice that express only one A-type lamin (either mature lamin A, or lamin C) also highlight potential functional differences. Mice expressing mature lamin A (no lamin C) have few if any overt phenotypes with the exception of misshapen nuclei, whereas mice that express only lamin C (no lamin A) have longer lifespans, are mildly obese and are predisposed to cancer [34,121,122]. Intriguingly, both A-type lamins and the Lamin B Receptor (LBR; a nuclear membrane protein) are essential molecular tethers for heterochromatin at the NE; LBR is especially important in early development (when lamin A/C expression is low), while A-type lamins are prominent later in development, perhaps explaining why lamins are thought to be dispensable for proliferation and differentiation of mouse embryonic stem cells (mESC)[123–125]. It remains unclear if lamins are necessary for robust LAD organization in mESC[29,126]. Previously we showed in fibroblasts, which are more terminally differentiated and where LBR is only minimally expressed, interphase LAD organization is disrupted by depleting both A-type lamins (A and C), but not lamin A alone [11].

Taken together, these data suggests lamin C might be required to tether LADs at the NE in cells lacking LBR. Therefore,in this study we examine the role of lamin C in LAD organization by examining LAD and chromosome configuration in cells specifically depleted in either lamin C or lamin A. Our data strongly support the hypothesis that lamin C is uniquely required for large scale chromosome organization. Our results provide insight into the mechanisms of 3D genome organization during interphase and its dynamic re-establishment after mitosis.

3.2 LAD proximity to the nuclear envelope is maintained by Lamin C

To test our hypothesis, we developed short hairpin RNAs (shRNA) that specifically downregulate lamin A (shA) or lamin C (shC). We also used shRNAs that downregulate both lamins A and C (shAC), or lamin B1 (shB1)[11]. To characterize the efficacy of lamin depletion and global effects on mouse embryonic fibroblasts (MEFs), we assayed for the presence of lamin isotypes after four days and monitored growth of cells during the same time-frame (Fig. S1). Each shRNA specifically targeted its own lamin, as shown by western analysis (Fig. S1A). shC, shB1 and shlacZ (control) all grew at the same rate, while shA and shAC displayed reduced growth rates, suggesting a unique role for lamin A in cell growth and cycling (Fig S1B). To try to assess if these isotypes had effects on LAD organization, particularly at specific regions, we performed a global DamID-seq analysis of LAD positioning (using DamLaminB1) in shRNA treated MEFs.

Surprisingly, these analyses revealed no significant differences in cells depleted of both lamin A and lamin C compared to wild-type cells (shAC; Fig. S2). While this was initially surprising, especially given our earlier findings that lamin A/C is required to organize regions to the lamina, we realize that an inherent limitation of DamID and related techniques is that data are aggregated from millions of cells, potentially obscuring true differences that would be detectable at the level of individual cells [11,12,20]. Detailed analysis of LAD boundaries (region of transition from NE-associated to NE non-associated), which are normally quite sharp, showed that LAD boundaries also remained intact under all four conditions (control, shAC, shA, shB1, or shC); genome-wide comparisons between log2 ratios of DamID-seq signals were virtually indistinguishable (Fig. S2a,b and S3), and genome-wide bioinformatically defined LADs for all three downregulated conditions showed preservation of WT LADs (>90% by base coverage) (Fig. S2C).

To observe LAD organization in single cells, we used 3D-immunoFISH to examine individual chromosome organization in shRNA downregulated MEFs. We highlighted the NE in green using antibodies to lamin B1 (or lamin AC in the case of shB1), and the LAD and non-LAD regions of chromosome 11 were ‘painted’ red and cyan, respectively, using oligonucleotide-based Chromosome Conformation Paints (CCP) [8,12]. As previously shown, in control nuclei, each chromosome occupied its own territory (Fig. 1), with LADs clustered together near the NE and non-LADs extending into the nucleoplasm[12]. This organization was grossly disrupted in cells depleted of both lamin A and lamin C (shAC); LADs failed to co-associate, with many LADs mislocalized to the nucleoplasm, and non-

LADs dispersed to occupy a territory considerably larger than controls (Fig. 1A). This finding is consistent with another study that showed chromosome territory expansion upon removal of LaminAC and our finding that lamin AC is required for de novo LAD tethering [11,23].

We next asked what the role and contribution of each individual lamin isotype was to this organization. We observed no gross perturbations of genome organization after loss of Lamin B1. Furthermore, loss of lamin A alone had no discernible effect on LAD organization, even though loss of this isotype displayed delayed growth. Strikingly, loss of lamin C was sufficient to fully recapitulate the gross disruption of chromosome 11 organization seen with loss of both isotypes (Fig. 1A). To better visualize and describe the observed perturbations, we plotted signal intensities from individual nuclei across lines drawn through the medial plane of each chromosome territory, as previously described [12] (Fig. 1B, S4-8). This analysis confirmed the normal positioning of LADs and nonLADs in control nuclei (Fig. 1A, B, S4), lamin B-depleted nuclei (Fig. 1A,B, S5) and lamin A-depleted nuclei (Fig 1A,B and S7), and confirmed the broadening of the distribution of the LAD signal intensity and the overall dispersion of LADs away from the NE in lamin C-depleted cells (Fig. 1A, B, S8), however, because of the severity of the phenotype and the inability to discriminate between individual deranged chromosomes, we could not reliably average these data.

Therefore, to accurately account for all disrupted cells, we counted the percentage of cells with disrupted genome organization in each population (Fig. 1B). Taking a conservative approach, we scored nuclei in which the majority of the LAD signal localized near the medial plane. Nuclei were considered disrupted if one (or both) chromosomes had LADs that were either dispersed (not aggregated or loss of LAD:LAD cohesion) or gross loss of NE-association. These were scored by two independent observers (blinded). By this metric, genome organization was disrupted in 16% of wildtype control nuclei (Fig. 1B). Cells depleted of lamin A showed a similar baseline (18%; Fig. 1B). We note that these cells are unsynchronized, so any alterations in LAD organization due to cell cycle stage are encompassed in this baseline data. In contrast, genome organization was disrupted in 85% of lamin C-depleted cells ($p<0.001$) and 88% of shAC cells ($p<0.001$; Fig. 1B and S6). One possibility, that lamin C was uniquely required for cell cycle progression, is unlikely since the doubling times for shC matched control cells were the same (Fig. S1, shLacZ vs. shC). Overall, these results supported our hypothesis by showing that lamin C is required for LAD self-association (LAD:LAD cohesion), LAD retention near the NE and overall compaction of the chromosome territory (including non-LAD regions).

3.3 Lamin C (not lamin A or lamin B1) is required to maintain LAD association with the NE

To independently evaluate the role of lamin C, we used cells bearing a single 'TCIS' LAD. TCIS (Tagged Chromosomal Insertion Site) is comprised of 256 tandem copies of the lacO sequence (allowing visualization upon expression of EGFP-LacI) and a modified RMCE (recombination-mediated cassette exchange) 'cassette', allowing for insertion of ectopic sequences. We previously showed, using this system, that a single segment of DNA (lamina associated sequence or LAS) can redirect the TCIS locus to the nuclear lamina. To test if lamin C is required for localization of a de novo LAD, we used two independent MEF clones bearing one of these TCIS-LAS, specifically, the Ikzf1 (Ikaros zinc finger protein) D6 Lamin Associated Segment, as previously described [11]. When this LAS is introduced into the clonal TCIS MEF lines (clone Y or clone 12, Fig2), the TCIS-LAS locus was NE-associated in 75-80% of nuclei, compared to ~40% of nuclei with TCIS locus alone (no LAS), when visualized by 3D-immunoFISH (Fig. 2A) and quantified by colocalization with lamin B1 (or laminAC for shB1) (Fig. 2). We used this TCIS-LAS which had high association with the NE to monitor and quantify LAD organization in MEFs depleted of lamin isotypes. Removing lamin B1 alone (shB1) or lamin A alone (shA) had no significant effect (TCIS-LAS remained lamina-proximal), whereas NE-association was reduced significantly in cells depleted of both A and C (shAC; Fig. 2; $p<0.001$), or lamin C alone (shC; Fig. 2B; $p<0.001$). Without lamin C the percentage of NE-associated TCIS-LAS loci was reduced to the background seen with the LAS-less TCIS cassette (Fig. 2B). These data are consistent with our previous finding that acute shRNA-mediated removal of lamin A was insufficient to perturb LAS NE-association [11]. Given that shC treated cells showed loss of LAD organization, we next verified that this phenotype could be rescued by expression of mCherry-tagged lamin C, but not lamin A. We stably expressed either mCherry-tagged human lamin A or human lamin C in shC treated MEFS. Importantly, these constructs were not targeted by our murine-specific shRNA. TCIS-LAS localization at the NE was fully restored by mCherry-human lamin C, and not by mCherry- human lamin A (Fig. S9). These results independently support the hypothesis that lamin C, in contrast to lamin A and lamin B1, is required to maintain LAD association with the NE and nuclear lamina.

3.4 Lamin C is nucleoplasmic during telophase and early G1-phase, and is significantly delayed in its association with the reforming NE

Our results thus far show that lamin C is important for normal interphase LAD configuration in MEFs (Fig. 1, 2). After mitosis, the nuclear lamina itself must be rebuilt and organized. The major consensus is that B type lamins associate with the nascent NE prior to A type lamins, and evidence of the differential dynamics of NE incorporation for lamin A versus lamin C are conflicting. In support of lamin C incorporating at the NE after lamin A, a study using injected recombinant proteins showed lamin A exhibited much faster lamina incorporation kinetics (20min) compared to lamin C (180 min) [127]. Even at 180min post-injection, nucleoplasmic lamin C foci were still evident. However, in that study, the incorporation of lamin C into the lamina was accelerated upon co-injection with lamin A, suggesting some cross regulation, in agreement with another study suggesting lamin C localization is dependent on lamin A [128]. A drawback of this study is that the normal regulation of both A/C ratios and post-translational modifications (PTM) are lacking and other studies have the correct localization of lamin C to the NE in the absence of lamin A [35]. In support of lamin A and C arriving at the NE at the same time, a study using lamin A and lamin C overexpressed individually, found that both A type lamins post-mitosis had similar kinetics of NE localization [49]. Of interest, interphase LAD and chromatin compartment organization is also ablated during mitosis and must also be rebuilt in the next G1. with overall chromosome positions and chromatin domains faithfully reinstated[12,45,110,115]. Yet, the pathway(s) and the mechanism by which LADs reorganize and re-associate with the nuclear lamina after mitosis are still not understood.

In order to understand the role that lamin C might play in this process and given the conflicting data regarding timing of lamin C incorporation to the lamins, we first sought to evaluate post-mitotic lamin isotype NE incorporation dynamics in our MEFs. We imaged lamins A, C and B1 during exit from mitosis using a specific lamin B1 antibody in MEFs co-expressing mCherry-laminA and EYFP-laminC (Fig. 3). Localization of each lamin isotype was measured by fluorescence intensity histograms for a minimum of 20 nuclei along a line drawn through the medial plane of the nuclear volume as determined by Hoechst signal (Fig. 3). We found that all isotypes tested, lamins A, C and B1, concentrate at the NE during interphase (Fig. 3 and Fig. S10a,b), with lamin C and, to a lesser degree, lamin A also localizing diffusely in the nucleoplasm (Fig. 3 and Fig. S10a,b). Such nucleoplasmic localization was not unexpected given previous reports describing a ‘nuclear veil’ of lamin A/C [129–131]. However, during telophase, when mCherry-lamin A and lamin B1 were already highly enriched or locolize to the nascent NE, EYFP-lamin C was solely nucleoplasmic, with no detectable concentration at the NE (Fig. 3A, B and Fig. S111a,b). Similar results were obtained using a purportedly lamin C-specific antibody (Fig. S12). These results were highly reproducible from cell to cell (Fig. S11a,b), with EYFP-lamin C persisting predominantly in the nuclear interior well into early G1, and then gradually incorporating into the nuclear lamina.

This delayed arrival of lamin C at the NE during early G1-phase was reminiscent of our previous finding that LADs are initially nucleoplasmic and exhibit delayed re-incorporation at the nuclear lamina after mitosis [12,71]. LADs themselves form nucleoplasmic intra-chromosomal LAD:LAD agglomerations during telophase and early-G1, and only associate with the NE as cells progress further into G1-phase, more LADS become NE-proximal and flatten against the lamina, with a subset of LADs remaining in the nuclear interior for up to three or four hours, well into G1 phase, quite reminiscent of the timing we noted for lamin C NE incorporation[12,71].This led us to question whether lamin C might colocalize with LADs at the end of mitosis and into early G1. To test this we used a LAD-tracer system to fluorescently identify all endogenous LADs in living cells (MEFs) coexpressing EYFP-lamin C [12,41,71]. The LAD-tracer system relies on the expression of two constructs. First, a construct expressing Dam-lamin B1 enables methylation of DNA at adenine residues in proximity to the nuclear periphery (i.e. marks LADs with meA), but has two additional domains that strictly control its expression: a destabilization domain (DD) that causes degradation in the absence of the shield ligand, and a Cdc10 dependent transcript 1(CDT) regulatory domain that restricts its expression to G1[12,41,71,132]. The second construct, the LAD-tracer, is a modified mCherry-tagged version of the previously described m6A-tracer[41,71] that binds meA, the modification generated by Dam-lamin B1, thus marking LADs with mCherry. The

LAD-tracer is expressed throughout the cell cycle, and identifies meA-modified DNA (LADs) in all phases in cells where both constructs are expressed at appropriate levels. As expected, EYFP-lamin C colocalized with the LAD-tracer in interphase cells (Fig. S13). However, during telophase and early-G1 we were surprised to find that lamin C and LADs occupied distinct nuclear volumes with minimal or no colocalization (Fig.4A, B and S14). Despite their apparent separation, timelapse movies showed that EYFP-lamin C and LAD aggregates had coincident arrival to and integration with the nuclear lamina (Fig. 4C and S15). These results suggest lamin C functions distal to LADs to influence their organization.

3.5 Lamin C is required during G1 phase for LAD integrity and LAD recruitment to the NE

To test if lamin C might play a role in restoring LAD organization after mitosis, we used shRNAs to specifically deplete lamin A or lamin C for four days to allow lamin turnover in MEF cells harboring the LAD-tracer system. These shRNA-treated cells were then subjected to a single thymidine block (24hours), followed by release into enriched media for several hours and subsequently treated with the Cdk1 inhibitor RO3306 to arrest them at the G2/M transition [12,133]. After overnight block, cells were released into complete medium (without shield ligand).Cells rapidly entered mitosis and were examined at subsequent time points, up to four hours later. Because LAD targeting to the NE after mitosis is normally gradual, over several hours, we chose to assay cells four hours after release from the G2/M block, when a majority of control cells have exited mitosis and show ‘resolved’ interphase LAD organization (Fig. 5A). Nuclei were independently scored by two observers as either ‘resolved’ (all LAD-tracer signal adjacent to lamin B1) or ‘unresolved’ (if any LAD-tracer signal was not adjacent to lamin B1); nuclei were counted over groups of 5 frames and then averaged across groups of 5 (n=4 groups, >150 nuclei). Nuclei lacking LAD-tracer signal were not scored. For the shCtrl-treated cells, 44% of nuclei had unresolved LADs. We note that this background of ‘unresolved’ LADs is mainly due to timing and shortcomings inherent in two-component systems requiring coexpression of two independent components. We estimated that about 30% of LAD-tracer expressing nuclei simply underexpress Dam-lamin B1 relative to LAD-tracer, leading to accumulation of diffuse mCherry in the nucleoplasm even in Mid-G1 and, while qualitatively different, these were included in the ‘unresolved’ numbers. Cells depleted of lamin A showed a similar background, with 38% unresolved nuclei (shA; Fig. 5), again suggesting lamin A has no active role in post-mitotic LAD assembly at the NE. By contrast, in the lamin C knockdown population, 62% of nuclei had unresolved LADs, a significant increase of nearly 50% over controls (Fig. 5; $p<0.001$). Interestingly, many disrupted lamin C-depleted nuclei revealed an additional phenotype: LAD aggregates appeared to have decondensed slightly, sometimes forming string-like networks in the nucleoplasm (Fig. 5A), quite distinct from the compact NE-associated LADs in controls (Fig. S16). This conformation of the heterochromatic LADs was even visible via Hoechst stain (Fig. 5A). Such string-like networks were absent from control and shA treated cells and differed from LAD organization seen in untreated or lamin A-depleted cells immediately after mitosis, where LADs not at the NE remained in clear condensed and separated domains. It is important to note that at 4 hours post release, the percentages of cells in M, early G1 and mid-G1/S/G2 were quite similar for all treatments. However, two hours after release, while the percentages of cells in mitosis and early G1 were the same in control (shLacZ) and shC-treated cells, we note that shA and shAC treated cells displayed an apparent lag in early G1 at two hours (Fig. S1C). We indicate that this is an apparent lag since we quantify 'early G1' on morphometric measures (nuclear size, shape, and/or obvious match to a sister nucleus) and both nuclear shape and size could be influenced by loss of lamin A, since lamin A has been implicated in the mechanoregulation of nuclear morphology. The immediate post-mitosis stage, where the nuclei are still rounded up and the cytoskeleton has not yet exerted its influence on nuclear shape may be a particularly relevant point in the cell cycle for lamin A. This finding makes it even more striking that shA treated cells do not display perturbed lamin organization. Together, these findings collectively demonstrate that lamin C is required for LAD integrity and dynamic LAD recruitment and association with the NE and nuclear lamina after cell division.

3.6 Discussion

Our findings provide novel insights into 3D genome organization by showing that LAD integrity and post-mitotic association with the NE depend on lamin C, and not on lamin A. To examine the effects of removing specific A type lamin spliceoforms on LADs and overall genome organization, we employed three imaging approaches: (1)

Chromosome conformation paints (CCP), (2) Tagged Chromosomal Insertion System (TCIS), and (3) the LAD-tracer system. These three methods enable examination of genome architecture at different levels of spatial and time resolution in both normal and lamin depleted cells. In addition, these methods provide single cell metrics of organization missed by bulk DamID analyses. Our CCP differentially label LADs and non-LADs across an entire chromosome, enabling us to visualize the organization of LADs and non-LADs, relative to each other and the nuclear lamina, in the context of the entire chromosome in situ. The TCIS system, on the other hand, allows us to observe changes to the peripheral localization of a single lamina associated genomic locus (LAS) and enables more robust quantification of perturbations to lamina association through a binary measure of lamina localization. Finally, the LAD-tracer system, which tags all LADs within the nucleus, allows us to measure the dynamics of LAD organization across the genome and relative to the nuclear lamina.

While we and others have previously implicated that A type lamins in regulating LAD organization, we speculated that lamin A and lamin C might have different roles in LAD organization [11,126]. Both lamin A and lamin C are encoded by LMNA and cross-talk in their expression levels in a given cell type has been noted [127]. Several lines of evidence, from super-resolution microscopy to ectopic expression studies indicate that lamin C and lamin A form unique networks that are nonetheless inter-dependent on some level [24,25,35,127]. Lamin C depleted mice (from birth) show little overt phenotype, with the exception of perturbed nuclear shapes, while mice expressing only lamin C (depleted of A) have longer lifespans [34,121,122]. Taken together, these data suggest that lamin A and C do indeed have differential roles in the nucleus. One such difference is in how lamin A and C form networks at the lamina, both in timing of association with the NE and in protein:protein interactions. For instance, lamin C preferentially interacts with nuclear pore complexes and altered A/C ratios change the mechanical properties of the nucleus [31,35]. In this study, we identified a critical role for lamin C in genome organization. In particular, lamin C is critical for both organizing LADs to the nuclear lamina and for LAD sub-chromosomal domain integrity, since acute depletion of this isotype caused derangement and inter-mixing of LAD/non-LAD (A/B compartment) chromatin (Fig. 1).

Interphase genome organization, including LAD and lamin organization, is ablated during mitosis and re-established in the subsequent G1 phase [8,12,46,71,110,113,114,134]. Previous studies suggest that A-type lamins organize to the reforming nuclear envelope with different kinetics, although there is some discrepancy on how lamin A and C might differ in their timing of association [31,49,127,128]. We find, in agreement with previous studies, that lamin B1 incorporates into the reforming NE at anaphase, preceding both lamin A and C incorporation. Our results, using both fluorescent proteins as well as immunofluorescence, indicate that lamin A associated with the NE prior to lamin C in MEFs, with the majority of lamin C remaining nucleoplasmic well into early G1 (Fig. 3, S10-S11a,b). This is intriguing given that lamin C appears to be critical for LAD organization (Fig. 1 and 2) and we had previously shown that LADs are also nucleoplasmic during this stage of the cell cycle [12].

To further define the spatial and temporal relationship between LAD organization and lamin C organization during the critical transition from mitosis into G1, we used the LAD-tracer system to demarcate LADs in EYFP-lamin C. Strikingly, lamin C was excluded from the heterochromatic LADs at mitotic exit well into early G1 (3 hours), suggesting that lamin C predominantly interacts with euchromatic regions of the genome or is excluded from heterochromatic regions in early G1 (Fig. 4, S13 and S14). Overall our data suggests that A-type lamin isotype bound to euchromatic regions is predominantly lamin C, which we find to be present at higher levels relative to lamin A in the nucleoplasm where euchromatin is enriched in interphase. We suggest that these interactions are established at the end of mitosis and persist into interphase (Fig, S11). Our conclusion that lamin C colocalizes with euchromatic regions at mitotic exit is particularly intriguing given a recent study that found that interphase nucleoplasmic A-type lamins, and in particular lamin C, preferentially interact with enhancers and promoters of active genes [135]. The lamins bound to these euchromatic regions remain phosphorylated on Serine 22 (a known mitotic PTM) even after mitotic exit. Intriguingly, the sites at which pS22-lamin C binds is altered in Hutchinson Gilford Progeria Syndrome (HGPS) and is correlated with upregulation of genes. Previous studies also found nucleoplasmic lamins bound to euchromatic regions that are reliant on the nucleoplasmic LAP2 (lamina associated peptide 2) isoform lap2α [39,136]. It is unknown how the interaction between lamin C and LAP2α are mediated, but such associations could be the result of PTM regulation on A type lamins. In addition, as demonstrated by altered pS22-lamin C chromatin binding and gene activation in HGPS, which results from a lamin A specific mutation, the interdependence of the lamin networks in regulating gene activity (and other processes) is likely an important aspect of these diseases. Finally, a previous proteomics study found that lamin C preferentially interacts with components of the NPC, a complex associated with euchromatin and depleted in heterochromatin [35]. Taken together these studies and our new results describe a role for lamin C independent of lamin A and acting through interactions with the euchromatic compartment of the genome.

Thus, as important as lain C is for organization of LADS, the post mitotic organization of these heterochromatic domains to the lamina via guided transit towards the NE through direct interactions with lamin C, is unlikely. What role might lamin C be playing during the transition from mitosis into G1? If lamin C is not directly interacting with LADs, how can it be such an important regulator of LAD organization? We find that, in the absence of lamin C (but not lamin A), LAD aggregates are delayed or prevented in their association with the NE. Importantly, the LADs appear to form string-like networks of interconnected aggregates (Fig. 5), strongly suggesting that there is a problem in spatially segregating the forming LAD /non-LAD (A/B) chromatin compartments. This is supported by our CCP studies (Fig. 1), in which we observe gross disruption of spatial organization of LAD:LAD interactions, loss of clear A/B intra-chromosomal domain organization, and loss of LAD association with the NE. Our findings therefore suggest that lamin C is dynamically spatially regulated during exit from mitosis to promote novel associations needed for LAD control, and/or to block aberrant interactions and premature reassembly at the NE.

3.7 Speculations and a model

We postulate that the temporal separation of incorporation of lamin isotypes at the nuclear periphery post mitosis allows for the formation of separate, but interdependent, lamina meshworks, as has been reported[35]. Our data suggests that lamin B1 NE meshworks are formed first, followed by lamin A and, lastly, lamin C, much of which remains nucleoplasmic throughout interphase. We speculate that the Serine 22 phosphorylation blocks or alters polymerization of A-type lamins, and enables a control in timing and level of incorporation into the NE[25,128,131]. The late recruitment of lamin C to the NE post-mitosis is strikingly coincident with LAD accumulation to this region, suggesting a coordinated regulation which is supported by LAD disruption in the absence of lamin C. We further speculate that, prior to its accumulation at the nascent NE, lamin C surrounds but is excluded from LADs and might 'instruct' genome reorganization by promoting robust LAD-LAD self-association within each chromosome and preventing LAD aggregation between chromosomes; a potential danger since euchromatin and heterochromatin are each capable of self-aggregating via phase partitioning [108]. Without a mechanism to prevent wide-spread self-aggregation, (or accretion), heterochromatin might globally cluster, leading to chromosome entanglement and difficulty accessing appropriate genes. In support of this, regulated wholesale agglomeration of heterochromatin in the center of the nucleus is reported in cell types that lack A-type lamins and LBR, such as rod photoreceptor cells [137]. We therefore propose a gross overall schema (Figure 6) outlining a suggested role for lamin C in the reorganization of the genome post-mitosis. We propose that lamin C might directly associate with euchromatin or interact with chromosome scaffolding proteins (such as CTCF) which are enriched on promoters, enhancers, and borders of compartments and LADs [12,13]. From a recent study, we propose that lamin C with phosphorylated Ser22 , a mitotic modification, will be retained in the nucleoplasm and interact with euchromatin, potentially through its interactions with LAP2α or NPC components [138]. In this model, a heterochromatin (LAD) core would be surrounded by lamin C monomers or short polymers which would serve as a 'buffer' between chromosomes. These interactions would also reinforce the separation between A- and B-compartment chromatin in each chromosome and prevent aberrant 'sticky' heterochromatin interactions between chromosomes. Lastly, this dual purposed segregation mechanism persists as both LADs and lamin C accumulate at the nuclear periphery, with the latter potentially dependent on or enriched in interactions with NPCs and their associated underlying euchromatin[139,140].

In summary, we discovered that lamin C is uniquely required to efficiently target LADs to the NE after cell division and to maintain the integrity of A/B compartments and overall gross 3D genome organization. We propose that lamin C promotes intra-chromosomal LAD aggregation and prevents aberrant trans-chromosomal heterochromatin interactions. Our results bring up several additional questions, particularly the role these proteins have in organizing and regulating the genome during development and how our findings might impact how we think and investigate laminopathies that do not directly affect lamin C. To fully understand the molecular pathway by which cells re-establish tissue-specific 3D genome architecture after mitosis, it will be important to establish both the role of post-mitotic PTMs of lamin C and the lamin C protein interactome during exit from mitosis.

3.8 Methods

Generation and maintenance of primary murine embryonic fibroblast (MEFs)

For primary MEFs, wild-type eight-week-old C57BL/6J mice were bred and embryos were harvested at E13.5. Individual embryos were homogenized using a razor blade, and cells were dissociated in 3 mL 0.05% trypsin for 20 min at 37°C, then 2 mL of 0.25% trypsin was added and incubated again at 37°C for 5 min. Cells were pipetted vigorously to establish single cells, passed through a 70 µm cell strainer, pelleted and then plated in 10 cm dishes and labeled as P0. MEFs were cultured DMEM High Glucose with 10% FBS, penicillin/streptomycin, L-glutamine and non-essential amino acids. Cells were cultured for no longer than 5 passages before harvesting for experiments. For initial DamID and m6A tracer experiments, longer term-culture C57BL/6 MEFs were purchased from ATCC (American Tissue Culture Collection, CRL-2752) and cultured according to their established protocols, in medium containing DMEM High, 10% FBS, Penicillin/Streptomycin and L-glutamine.

Lamin A/C knockdown

shRNA-mediated knockdown was carried out as described previously. Specifically, virus for knockdowns were generated in HEK 293T/17 cells (ATCC CRL-11268) by co-transfecting VSV-G, delta 8.9, and a plko.1 vector driving the expression of control shRNAs - shluciferase (5’-CGCTGAGTACTTCGAAATGTC-3’) or shLacz (5’-CGCTAAATACTGGCAGGCGTT-3’), shLmnA/C(Sigma clone NM_001002011.2-901s21c, 5’-GCGGCTTGTGGAGATCGATAA-3’), shLmnA (produced in our lab), shLmnC (produced in our lab, 5’-TCTCCCACCTCCATGCCAAAG-3’) or shLmnB1 (Sigma clone NM_010721.1-956s1c1, 5’-GCGTCAGATTGAGTATGAGTA-3’) with Fugene 6 transfection reagent (Promega E2691). 10 mM sodium butyrate was then added to the transfected cells 3 hours post transfection for an overnight incubation at 37°C, 5% CO2. The transfection media containing sodium butyrate was removed the following day and the cells were washed with 1X PBS. Opti-MEM was then added back to the cells which were then incubated at 37°C, 5% CO2. Viral supernatant was collected every 12 hours up to 3 collections and the supernatant of all 3 collections were pooled. Primary MEFs were cultured as described and incubated overnight with different shRNA viruses per condition supplemented with 4 μg/mL polybrene and 10% FBS for 12-14 hours. Fresh MEF media was then added to the cells after the virus was removed and selected with 20 μg/ml blasticidin or 2ug/ml puromycin. For DamID profiling, cells were infected with DamID virus 4 days post shRNA transduction and cultured for an additional 48 hours.

DamID Infection

DamID was performed as described previously[11,13,103,141,142]. Cells were transduced with lentiviruses harboring the Dam constructs. Lentiviral vectors pLGW-Dam and pLGW Dam-LmnB1 were co-transfected with VSV-G and delta 8.9 into HEK 293T/17 packaging cells using the Fugene 6 transfection reagent in DMEM High glucose complete media (DMEM High glucose supplemented with 10% FBS, Penicillin/Streptomycin, L-glutamine). 10 mM sodium butyrate was added to the transfected cells 3 hours post-transfection and left overnight. The following day this media was removed and the cells were washed briefly with 1X PBS before Opti-MEM media was added. Supernatants containing viral particles were collected every 12 hours between 36-72 hours after transfection, and these collections were pooled, filtered through 0.45 µM SFCA or PES, and then concentrated by ultracentrifugation. For infection with lentivirus, MEFs were incubated overnight with either Dam-only or Dam-LmnB1 viral supernatant and 4 µg polybrene. Cells were allowed to expand for 2-4 days then pelleted for harvest.

DamID protocol

MEFs were collected by trypsinization and DNA was isolated using QIAamp DNA Mini kit (Qiagen, 51304), followed by ethanol precipitation and resuspension to 1 µg/ul in 10 mM Tris, pH 8.0. Digestion was performed overnight using 0.5-2.5 µg of this genomic DNA and restriction enzyme DpnI (NEB, R0176) and then heat-killed for 20 minutes at 80°C. Samples were cooled, then double stranded adapters of annealed oligonucleotides (IDT, HPLC purified) AdRt (5′-CTAATACGACTCACTATAGGGCAGCGTGGTCGCGGCCGAGGA-3′) and AdRb (5′-TCCTCGGCCG-3′) were ligated to the DpnI digested fragments in an overnight reaction at 16°C using T4 DNA ligase (Roche, 799009). After incubation the ligase was heat-inactivated at 65°C for 10 minutes, samples were cooled and then digested with DpnII for one hour at 37°C (NEB, R0543). These ligated pools were then amplified using AdR_PCR oligonucleotides as primer (5′-GGTCGCGGCCGAGGATC-3′) (IDT) and Advantage cDNA polymerase mix (Clontech, 639105). Amplicons were electrophoresed in 1% agarose gel to check for amplification and the size distribution of the library and then column purified (Qiagen, 28104). Once purified, material was checked for LAD enrichment via qPCR (Applied Biosystems, 4368577 and StepOne Plus machine) using controls specific to an internal Immunoglobulin heavy chain (Igh) LAD region (J558 1, 5′-AGTGCAGGGCTCACAGAAAA-3′, and J558 12, 5′-CAGCTCCATCCCATGGTTAGA-3′) for validation prior to sequencing.

DamID-seq Library Preparation

In order to ensure sequencing of all DamID fragments, post-DamID amplified material was randomized by performing an end repair reaction, followed by ligation and sonication. SpecificallyBriefly, 0.5-5 µg of column purified DamID material (from above) was end-repaired using the NEBNext End Repair Module (NEB E6050S) following manufacturer's recommendations. After purification using the QIAquick PCR Purification Kit (Qiagen, 28104), 1µg of this material was then ligated in a volume of 20 µL with 1µl of T4 DNA ligase (Roche, 10799009001) at 16°C to generate a randomized library of large fragments. These large fragments were sonicated (in a volume of 200µL, 10mM Tris, pH 8.0) to generate fragments suitable for sequencing using a Bioruptor® UCD-200 at high power, 30 seconds ON, 30 seconds OFF for 1 hour in a 1.5 mL DNA LoBind microfuge tube (Eppendorf, 022431005). The DNA was then transferred to 1.5 ml TPX tubes (Diagenode, C30010010-1000) and sonicated for 4 rounds of 10 minutes (high power, 30 seconds ON and 30 seconds OFF). The DNA was transferred to new TPX tubes after each round to prevent etching of the TPX plastic. The sonication procedure yielded DNA sizes ranging from 100-200 bp. After sonication, the DNA was precipitated by adding 20 µl of 3M sodium acetate pH 5.5, 500 µl ethanol and supplemented with 3 µl of glycogen (molecular biology grade, 20 mg/ml) and kept at -80°C for at least 2 hours. The DNA mix was centrifuged at full speed for 10 min to pellet the sheared DNA with the carrier glycogen. The pellet was washed with 70% ethanol and then centrifuged again at full speed. The DNA pellet was then left to air dry. 20 µl of 10 mM Tris-HCl was used to resuspend the DNA pellet. 1 µl was quantified using the Quant-iT PicoGreen dsDNA kit (Invitrogen, P7589). Sequencing library preparation was performed using the NEBNext Ultra DNA library prep kit for Illumina (NEB, E7370S), following manufacturer instructions. Library quality and size was determined using a Bioanalyzer 2100 with DNA High Sensitivity reagents (Agilent, 5067-4626). Libraries were then quantified using the Kapa quantification Complete kit for Illumina (Kapa Biosystems, KK4824) on an Applied Biosystems 7500 Real Time qPCR system. Samples were normalized and pooled for multiplex sequencing.

DamID-seq data processing

DamID-seq reads were processed using LADetector (https://github.com/thereddylab/pyLAD), an updated and packaged version of the circular binary segmentation strategy previously described for identifying LADs from either array or sequencing data (https://github.com/thereddylab/LADetector)[11,103]. LADs separated by less than 25 kb were considered to be part of a single LAD. All other parameters were left at default values. LADs were post-filtered to be greater than 100 kb, complementary genomic regions to LADs were defined as non-LADs. Bed files were generated for visualization using the pyLAD LADetector.

LAD and non-LAD chromosome-wide probe design and labeling

LADs from murine embryonic fibroblasts were defined through the LADetector algorithm, and complementary regions to Chromosomes 11 and 12 were defined as non-LADs[12]. Data provided Geo GSE56990. Centromeres were excluded, and LAD and non-LADs were repeat masked. Probes were selected in silico based on TM and GC content, and those with high homology to off target loci were specifically removed. 150 base pair oligos were chemically synthesized using proprietary Agilent technology and probes were labeled with either Cy3 or Cy5 dyes using the Genomic DNA ULS Labeling Kit (Agilent, 5190-0419). 40 ng of LAD and non-LAD probes were combined with hybridization solution (10% dextran sulfate, 50% formamide, 2X SSC) then denatured at 98°C for 5 minutes and pre-annealed at 37°C.

3D-ImmunoFISH and immunofluorescence

3D-immunoFISH was performed as described previously[11,142]. Briefly, primary mouse embryonic fibroblast cells were plated on poly-L-lysine coated slides overnight. Cells on slides were fixed in 4% paraformaldehyde (PFA)/1X PBS for 16 minutes, then subjected to 3-5 minute washes in 1X PBS. After fixation and washing, cells were permeabilized in 0.5% TritonX-100/0.5% saponin for 15-20 minutes. The cells were washed 3 times 5 minutes each wash in 1X PBS, then acid treated in 0.1N hydrochloric acid for 12 minutes at ro[11,142]om temperature. After acid treatment, slides were placed directly in 20% glycerol/1X PBS and then incubated at least one hour at room temperature or overnight at 4°C. After soaking in glycerol, cells were subjected to 4 freeze/thaw cycles by immersing glycerol coated slides in a liquid nitrogen bath. Cells were treated with RNAse (100 µg/ml) for 15 min in 2X SSC at room temperature in a humidified chamber. DNA in cells was denatured by incubating the slides in 70% formamide/2X SSC at 74°C for 3 min, then 50% formamide/2X SSC at 74°C for 1 min. After this denaturation, cells were covered with a coverslip containing chromosome conformation paints in hybridization solution and sealed. After overnight incubation at 37°C, slides were washed three times in 50% formamide/2X SSC at 47°C, three times with 63°C 0.2X SSC, one time with 2X SSC, and then two times with 1X PBS before blocking with 4% BSA in PBS for 30-60 min in a humidified chamber. Slides were then incubated with anti-LmnB1 primary antibody (1:200 dilution; Santa Cruz, SC-6217) in blocking medium overnight at 4°C. Slides were washed three times with 1X PBS/0.05% Triton X-100 and then incubated with secondary antibody in blocking medium Alexa Fluor 488 (1:200 dilution; A32814) for 1 hour at room temperature. Post incubation, slides were washed three times with 1X PBS/0.05% Triton X-100, and then DNA counterstained with 1 µg/ml Hoechst. Slides were then washed, mounted with SlowFade Gold (Life Technologies, S36936).

Live Cell imaging

Immortalized C57Bl/6 MEFs (ATCC CRL-2752) cells were infected to stably express ddDam-LaminB1-CDT, eGFP-Lamin C and m6A tracer. ddDam-LaminB1-CDT is a destabilized version of the previously described DamID construct that has incorporated the CDT domain from the Fucci system to ensure its expression is restricted to interphase[12,41,71,132]. The m6A-tracer is comprised of a catalytically inactive version of DpnI, that retains its ability to bind DNA, in frame with an mCherry red fluorescent protein [41,71]. For cell cycle experiments, these cells were grown in the presence of shield ligand (AOBIOUS, AOB6677), which stabilizes the ddDam-LaminB1-CDT, along with 1mM thymidine (Sigma) block for 24 hours to enable synchronization of cells at G1/S. This arrest was followed by release into complete DMEM medium (DMEM high glucose, +10%FBS, 100 U/mL Penicillin and 100 µg/mL Streptomycin) containing 25µM 2’-Deoxycytidine for 4 hours. Cells were then blocked at G2/M by incubation by replacing media with complete media containing 10uM R0-3306 (AOBIOUS, AOB2010) for 16-20 hours[133]. Cells were released from this block by washing 3 times with warm Fluorobrite DMEM +10% FBS with 100 U/mL Penicillin and 100 µg/mL Streptomycin. 1-4 hours after release cells were imaged live every 1-5 using a 3i spinning disc confocal microscope. Interphase cells were not synchronized and were imaged every 1-5 minutes.

TCIS

The two TCIS clones, clone Y and clone 12, harboring a LAS corresponding to a fragment of the Ikzf1 gene was generated as previously described[11]. C57BL/6 fibroblasts were transfected, using Fugene 6 (Promega), with a linearized TCIS construct described previously[11]. Cells were selected for hygromycin resistance (500 µg/ml), and clones were isolated and expanded. Single integration clones were screened for by qPCR and transfection with EGFP-LacI retroviral vector to visualize the insert site. Clones 12 and Y had single integrations of the TCIS system at a chromosomal position away from the nuclear lamina, as determined by microscopy and either the presence or lack of an overlap in LMNB1 and EGFP-LacI accumulation at the lacO insert site. Site-specific recombination was obtained by cotransfection of TCIS clones with a DNA fragment corresponding to the LAS (Ikzf1) cloned into a switch vector and Cre recombinase. Switched cells were then seeded at low density with 10,000 cells per well of a 6-well tissue culture dish and treated with 1 µM ganciclovir for 24 h. TCIS cells require a short treatment with ganciclovir and to be treated at low confluence. Negative ganciclovir selection occurs when the nonswitched thymidine kinase gene cassette expresses thymidine kinase, which in turn phosphorylates ganciclovir. Phosphorylated ganciclovir is toxic to the cells. Once released into the media, it can affect neighboring cells if not maintained at low confluence and if media is removed after 24 h. Cells that have successfully switched cannot phosphorylate ganciclovir and are therefore resistant. Cells resistant to ganciclovir (1 µM) were then expanded for nuclear positioning analysis. Transfections for specific recombination in TCIS clones were performed with the electroporation system (Amaxa Nucleofector 4; Lonza), to ensure essentially 100% transfection efficiency. Ingenio Electroporation Products (MIR 50111; Mirus Bio LLC) were used in combination with the Amaxa nucleofector. All cell lines were maintained in

DMEM high with 10% FBS (U.S. Defined Fetal Bovine Serum; Hyclone) in the presence of 500 µg/ml hygromycin (50 mg/ml; Hygromycin B; Corning/CellGro) and 1 mM IPTG when EGFP-LacI was present. To enable binding of EGFP-LacI, IPTG was removed from the cultures, and cells were analyzed after 24–36 h in fresh media.

Fluorescent tagged lamin overexpression

Lentiviral vectors containing fluorescently tagged lamin A or C were co-transfected with VSV-G and delta 8.9 into HEK 293T/17 packaging cells using the Fugene 6 transfection reagent in DMEM High glucose complete media (DMEM High glucose supplemented with 10% FBS, Penicillin/Streptomycin, L-glutamine). 10 mM sodium butyrate was added to the transfected cells 3 hours post-transfection and left overnight. The following day this media was removed and the cells were washed briefly with 1X PBS before Opti-MEM media was added. Supernatants containing viral particles were collected every 12 hours between 36-72 hours after transfection, and these collections were pooled, filtered through 0.45 µM SFCA or PES, and then concentrated by ultracentrifugation. For infection, MEFs were incubated overnight with either mCherry-LmnA or eYFP Lamin C viral supernatant and 4 µg polybrene. Cells were allowed to expand in selection media containing 2ug/mL puromycin or 20ug/mL blasticidin respectively for 2-4 days followed by a second round of transduction with the other fluorescent tagged lamin viral supernatant followed by expansion in selection media containing both 2ug/ml puromycin and 20ug/ml blasticidin.

3.9 Figures

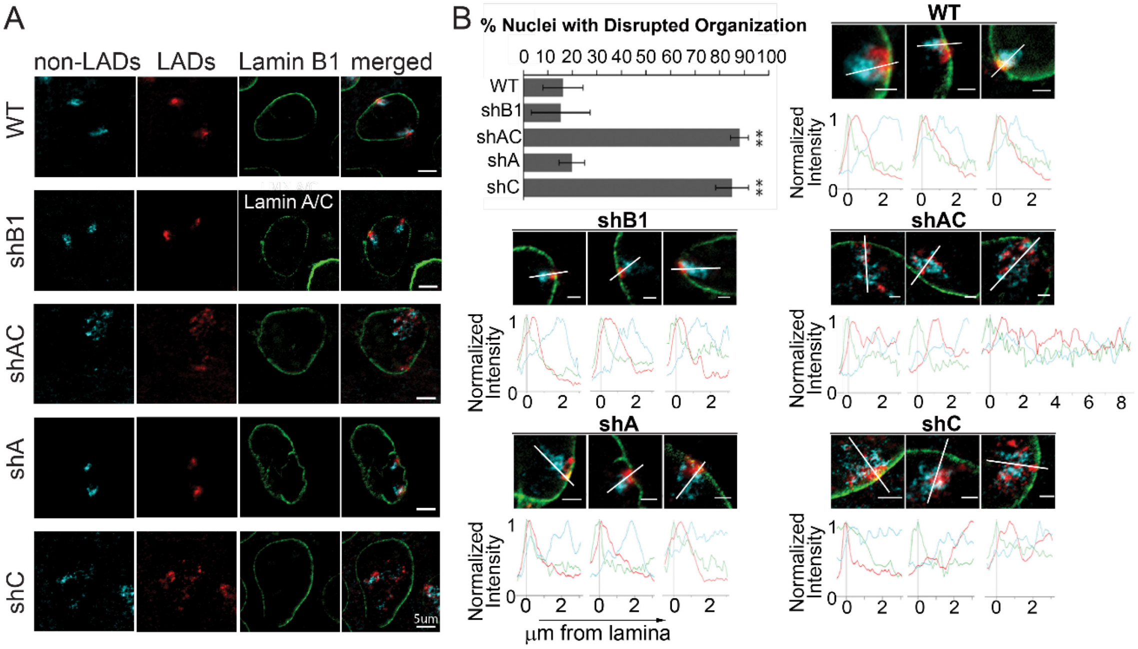

Figure 3.1: Lamin C is important for chromosomal sub-domain organization. (A) Representative images showing the organization of chromosome 11 with nonLADs in cyan, LADs in red and lamin B1 (or lamin A/C for shB1 treated cells) in green. (B) Quantification of nuclei with disrupted organization for each knockdown condition. Error bars represent 1 standard deviation. $**$ indicates t-test p value <0.001 (n>200 nuclei per condition). Representative images of chromosome conformation paints to chromosome non-LADs (cyan) LADs (red) Lamin B1 (green; lamin A/C for shB1 treated cells) in primary MEFs. Images were chosen to represent the spectrum of phenotypes for each knockdown. Normalized fluorescence intensity histogram plots: from nuclear lamina (0μm) to 3μm into the nucleus, were plotted for all chromosome 11 territories (except territory 3 of shAC, which was expanded to display the extent of LAD disruption

for that nucleus). The line each plot travels through is represented by a white line. Scale bar = 2μm.

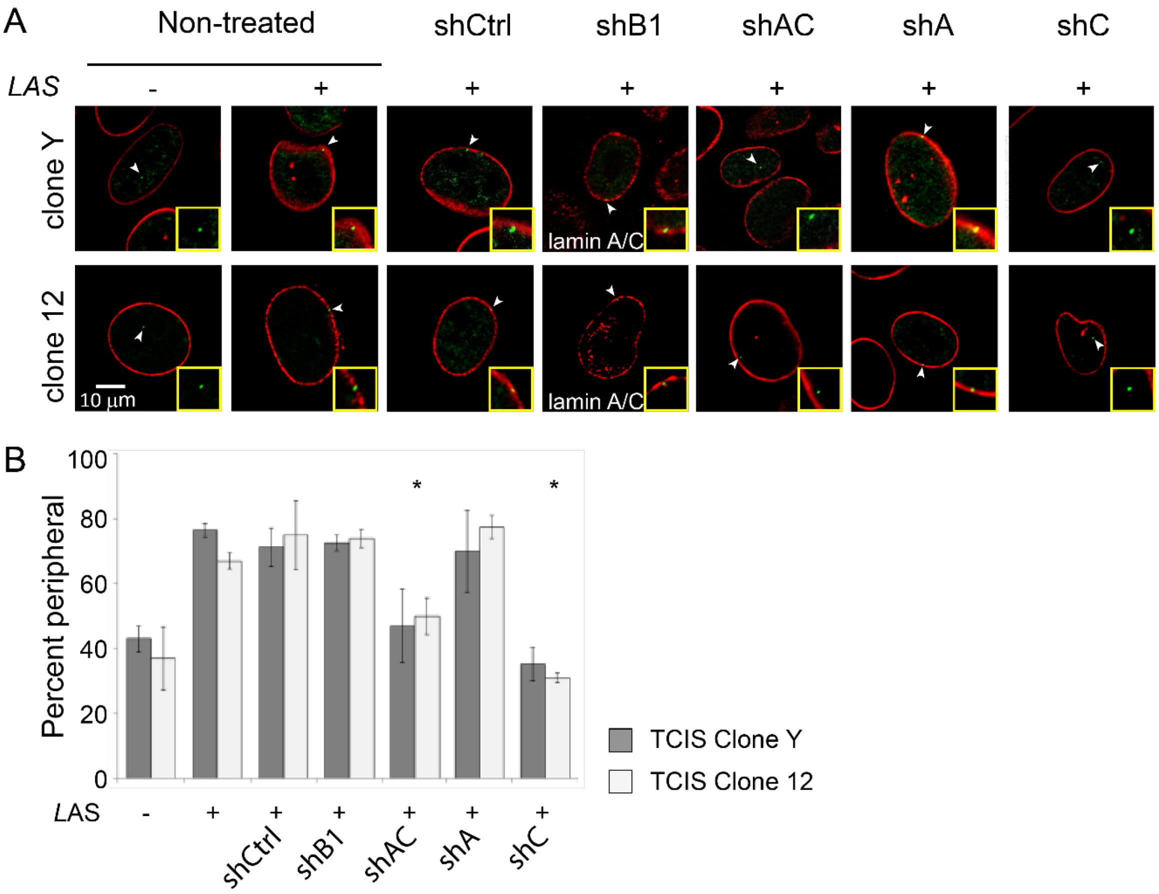

Figure 3.2: Lamin C is required for recruitment of chromatin to the lamina. (A) Representative images showing the disposition of lacO arrays (arrowheads, green) and lamin B1 (red, lamin A/C in shB1 treated cells) in the TCIS clones Y (top) and 12 (bottom) pre- and post- ‶switching” in of the Ikzf LAS and the effects of specific lamin depletion on the position of the lacO arrays. The inset shows 300× magnification. (B) Quantification of peripheral association was determined by overlap of EGFP-LacI foci and Lamin B1 (n ≥ 50). Error bars indicate SD. $p \leq 0.001$ is indicated by asterisks.

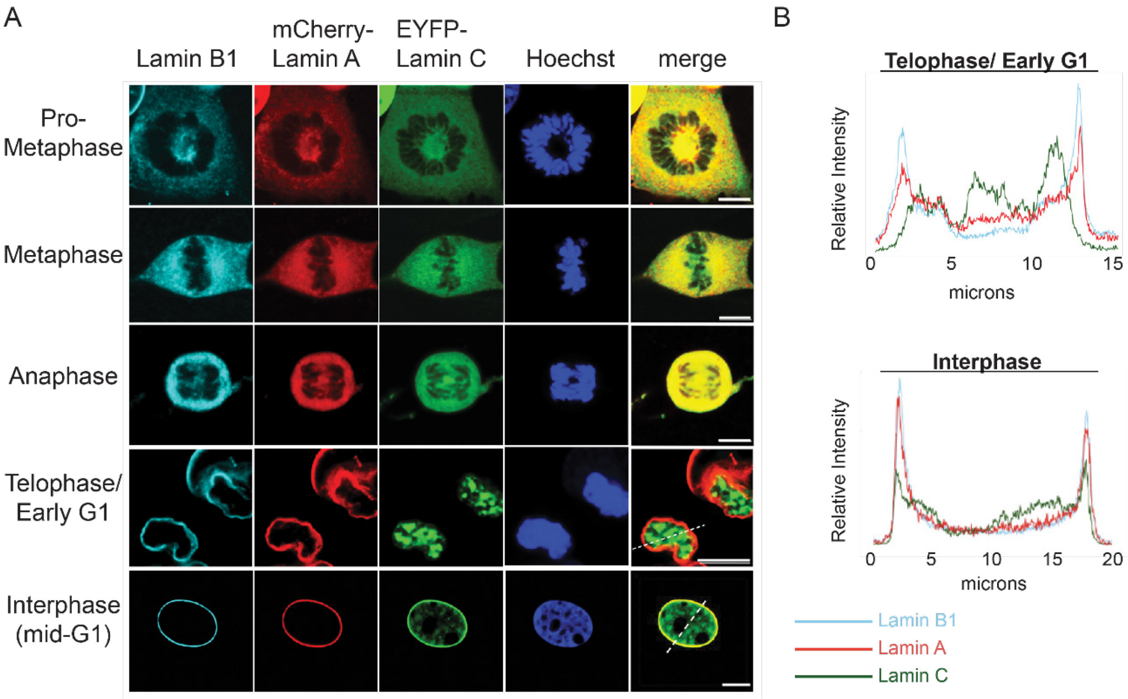

Figure 3.3: Lamin C persists in the nucleoplasm after mitosis. (A) Representative images of lamin B1 (cyan), lamin A (red), lamin C (green) and chromatin (blue) in different stages of the cell cycle. Merged images show lamins A and C localization. Dotted lines on the merged images for telophase/early G1 and G1 indicate the segment used for line scan displays shown in (B). (B) shows representative plots of intensities of lamin B1 (cyan), lamin A (red) and lamin C (green) along the dotted lines (from left to right) as shown in the merged images in (A) for the telophase/early G1 transition stage of the cell cycle and the mid-G1 (interphase) stage. Scale bar is 10μm.

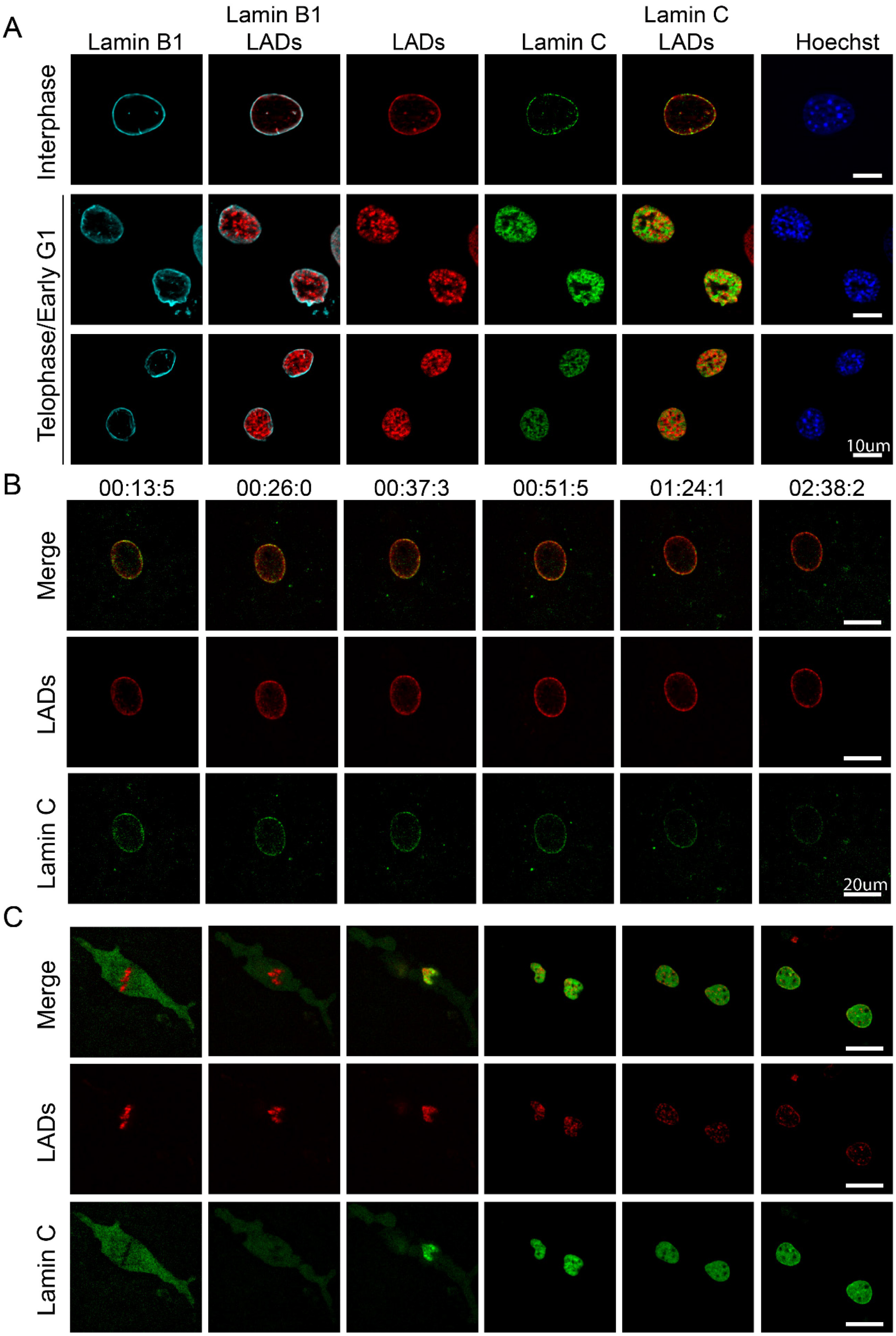
A
Lamin B1
Lamin B1 LADs
LADs
Lamin C
Lamin C LADs
Hoechst
Interphase
Telophase/Early G1
10um
B
00:13:5
00:26:0
00:37:3
00:51:5
01:24:1
02:38:2
Merge
LADs
Lamin C
20um
C
Merge
LADs
Lamin C

Figure 3.4: Lamin C and LADs are recruited to the NE in G1, but are not co-localized in the nucleoplasm (A)Representative images of interphase and early G1 nuclei with anti-lamin B1 (cyan), LAD-tracer (red), and lamin C (green), DNA (blue). (B) Still images from time-lapse movie 1 of LADs (red) EYFP-lamin C (green) during interphase. Scale Bar is 20μm (C). Still images from time lapse movie 3 of LADs (red) EYFP-Lamin C (green) during mitosis. Scale bar is 20μm. Images were chosen to exemplify certain stages (metaphase, anaphase, telophase, early G1, partially resolved, fully resolved).

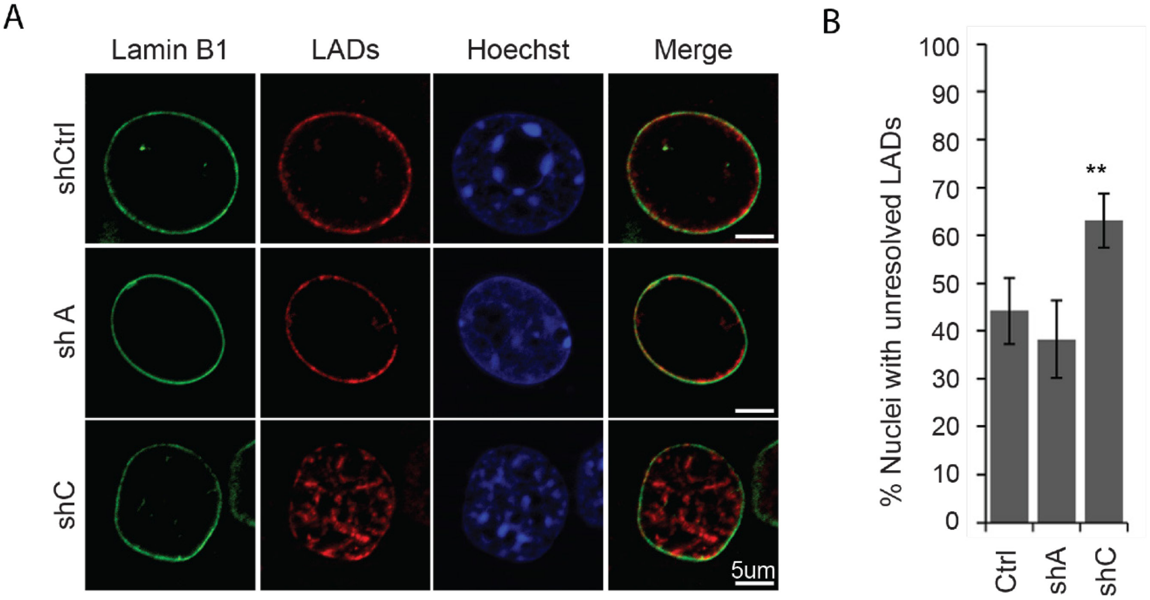

Figure 3.5: Depletion of lamin C leads to aberrant LAD accretion and localization to the NE. (A) Cells shown 4 hours after release from G2/M border. Anti-lamin B1 (green) LAD-tracer (red) Hoechst (blue) (B) Quantification (blind analysis) of nuclei with unresolved LADs (nuclei with LADs not at the periphery) 4 hours after release from the G2/M border ($n \geq 120$). Error bars indicate SD. $p \leq 0.001$ is indicated by asterisks.

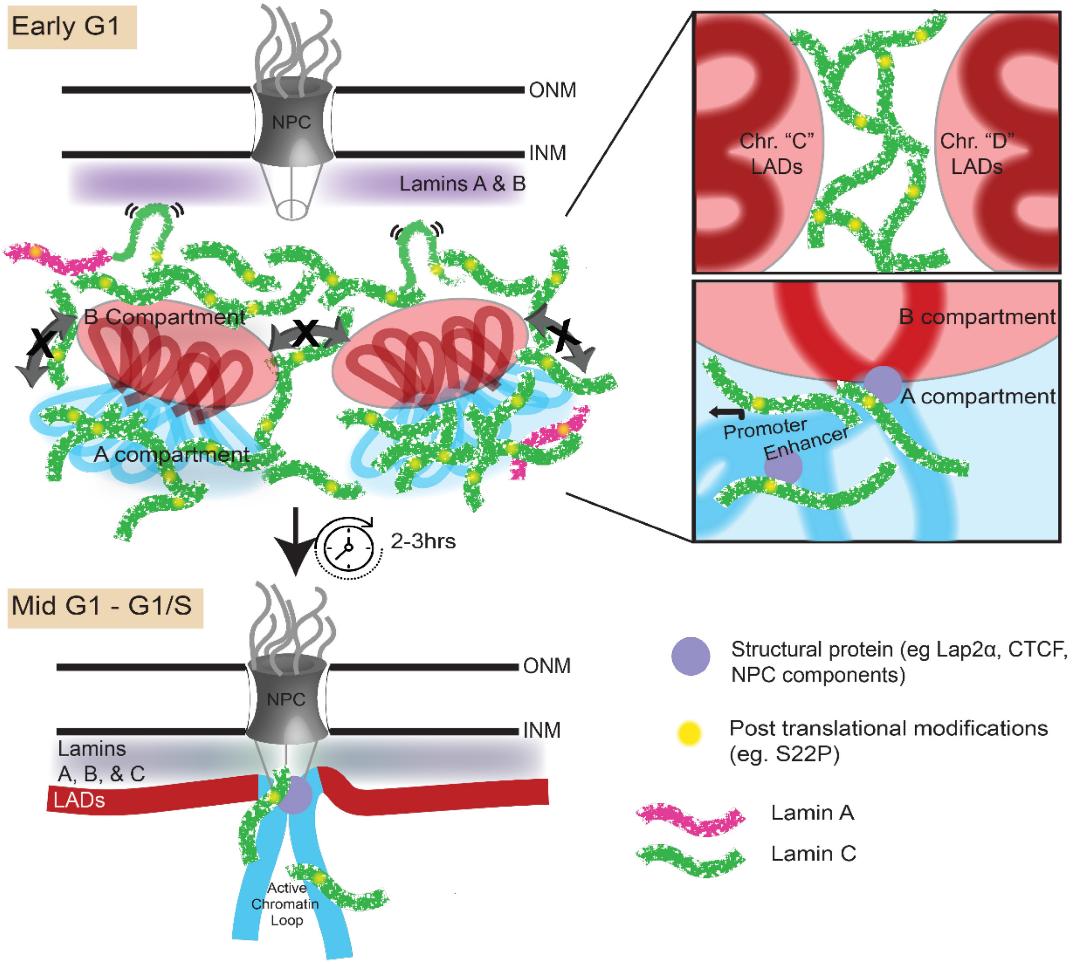

Figure 3.6: Speculative model of the role of lamin C in genome organization. Post translational modifications (e.g. Phosphoserine 22) of lamin C allows its nucleoplasmic localization during mitotic exit and into early G1. During this phase lamin C is spatially excluded from LADs potentially by binding to structural proteins such as CTCF, LAP2α etc on euchromatin and/or phase separation phenomena thereby physically hindering aberrant inter-chromosomal LAD interactions (Top inset) and reinforcing intra-chromosomal A-B compartmentalization (Bottom inset).

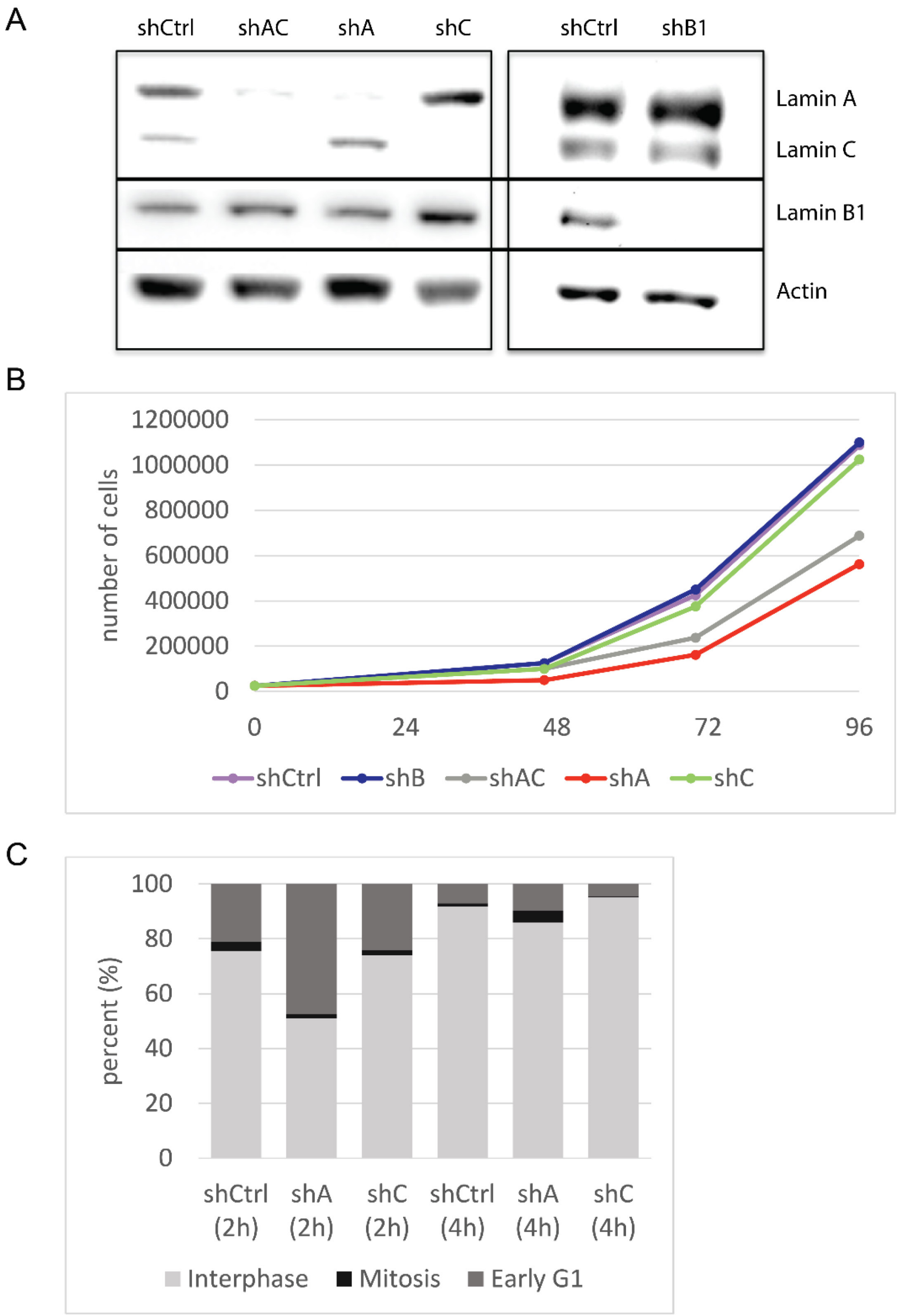

Supplemental

Figure 3.1: Analysis of shRNA knockdown cells. (A) Representative western blots showing specificity of the various knockdown constructs. (B) 25,000 cells were plated at 0 hours. Graph represents the number of cells on each plate after a given number of hours for each shRNA treatment indicated (shCtrl, shB1, shAC, shA, shC). (C) Graph

indicates the percentage of synchronized cells in either interphase, mitosis or G1 as assessed from nuclear lamina morphology at either 2hours or 4hours after release into mitosis for each condition (shCtrl, shA or shC).

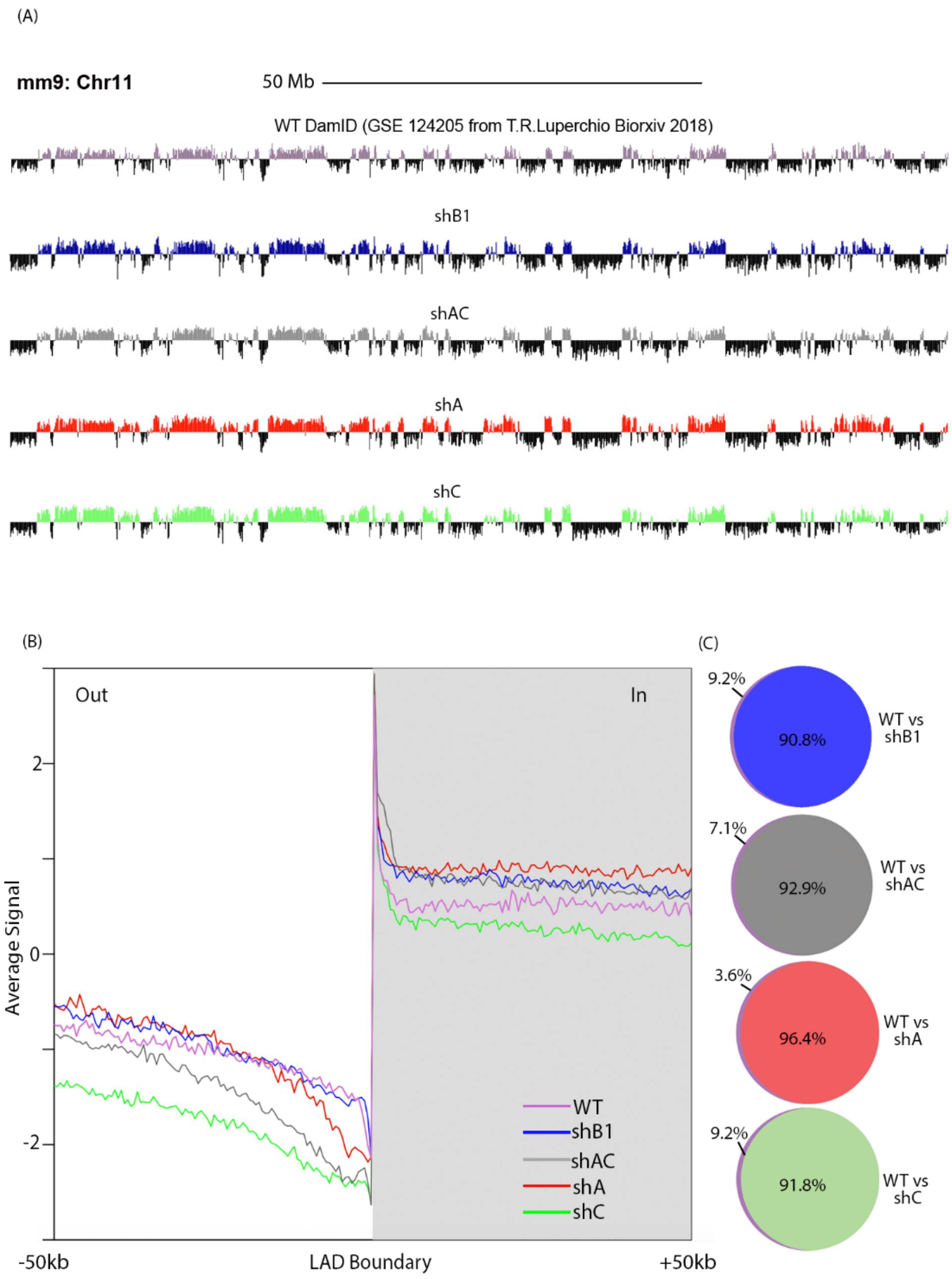

Supplemental Figure 3.2: DamID analysis of shRNA treated cells. (A) Chromosome wide DamID traces (chromosome 11; chr 11) for wild-type (purple), lamin B1 depleted (blue), lamin A/C depleted (gray), lamin A depleted (red), and lamin C depleted (green) samples. Vertical axes are of log2 scale and traces above 0 (in indicated color), depict a higher than expected frequency of peripheral association. (B)Profiles of aligned LAD border regions (left and mirrored right border regions combined) are shown for lamin B1 interactions with chromatin (DNA). To align LAD borders, genome-wide positions of lamin B1 interactions were converted to coordinates relative to the nearest border. Gray area and positive coordinates, inside LADs; white area and negative coordinates, outside LADs. (C)Venn Diagram showing the proportion of wild type LAD domains preserved in the absence of lamin B1 or lamin A or C alone or both lamins A and C.

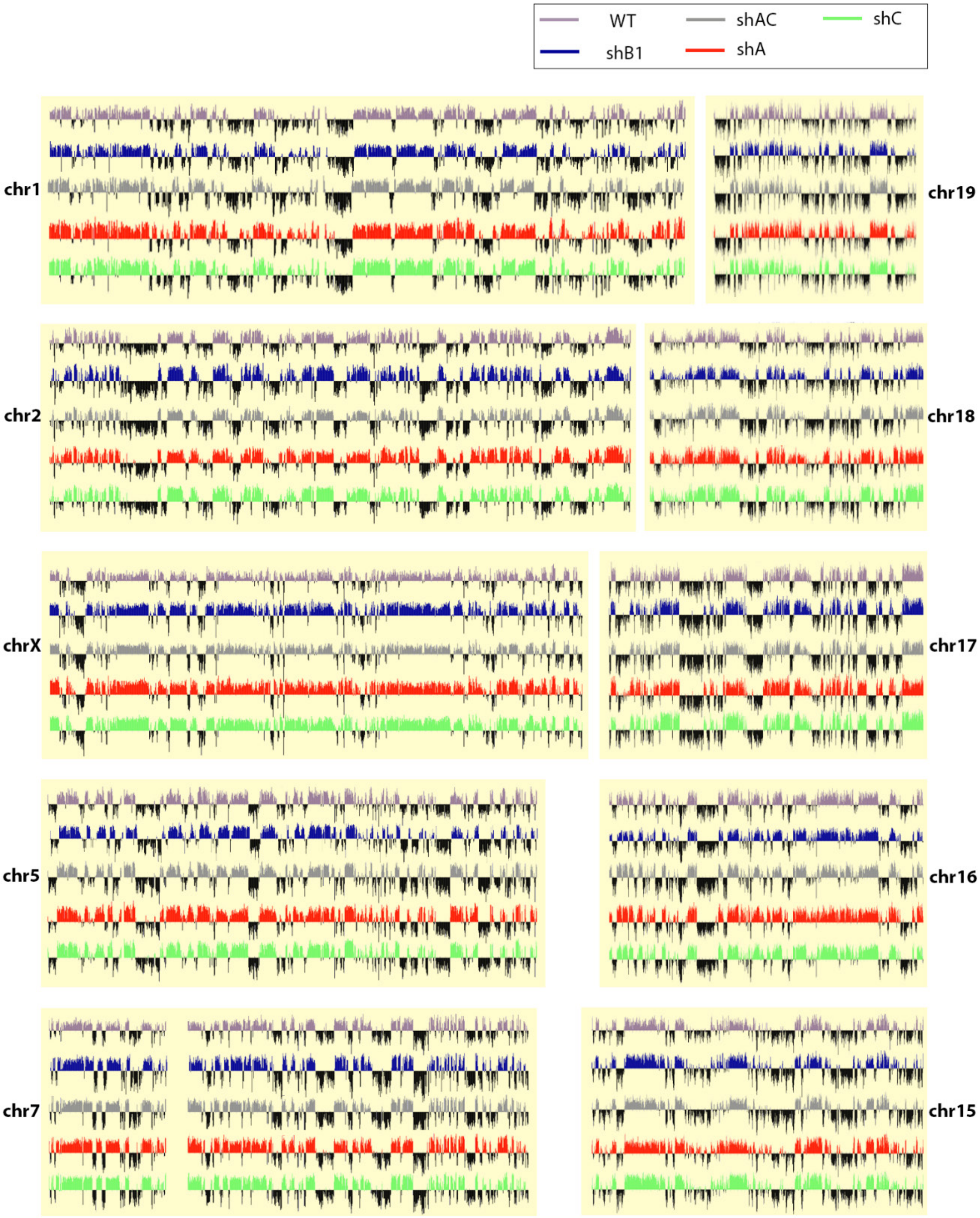
WT
shB1
shAC
shA
shC
chr1
chr19
chr2
chr18
chrX
chr17
chr5
chr16
chr7
chr15

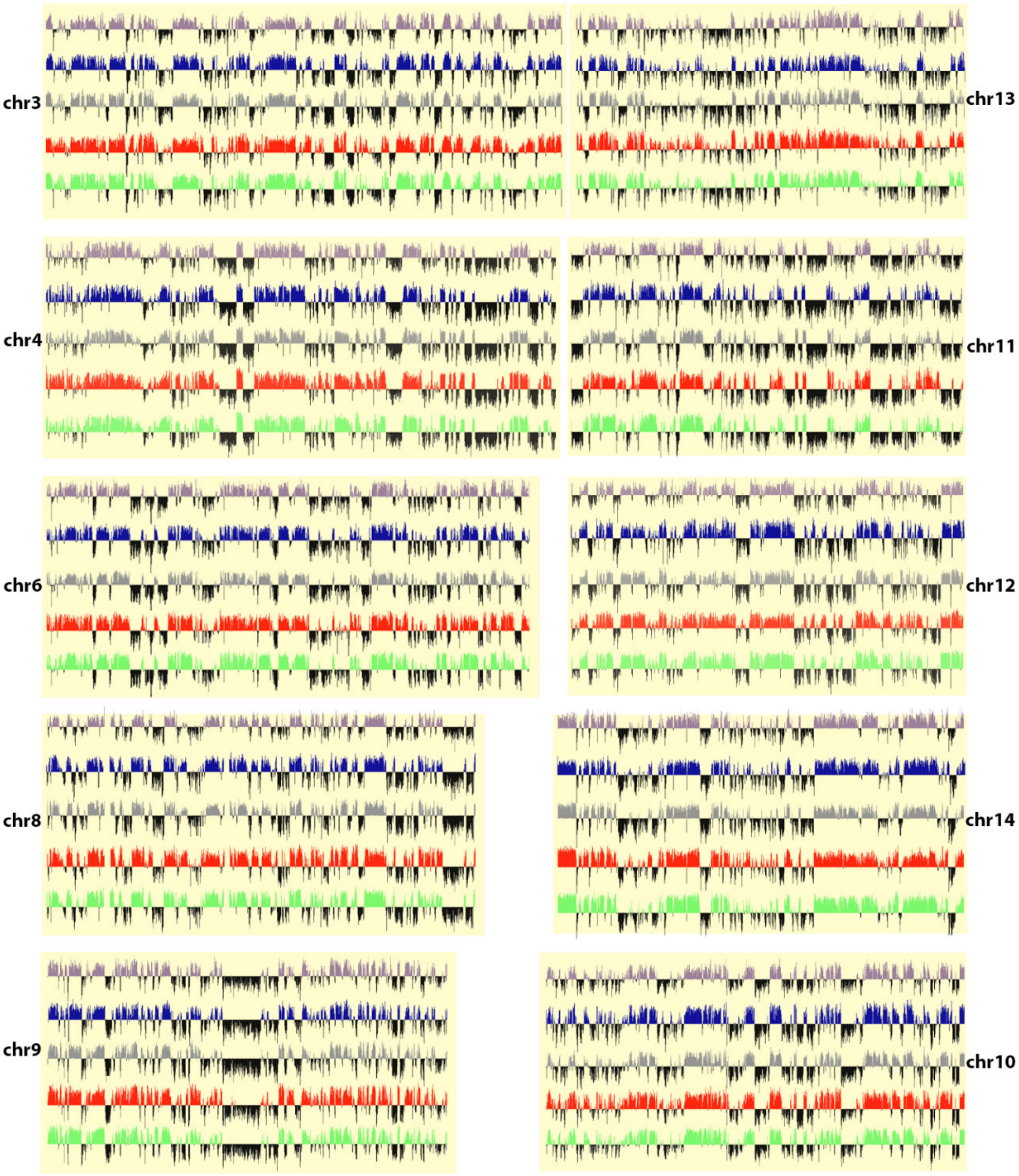

Supplemental Figure 3.3: Genome-wide normalized DamID signal. Chromosome wide DamID traces for wild-type (purple), lamin B1 depleted (blue), lamin A/C depleted (gray), lamin A depleted (red), and lamin C depleted (green) samples. Vertical axes are of log2 scale and traces above 0 (in indicated color), depict a higher than expected frequency of peripheral association.

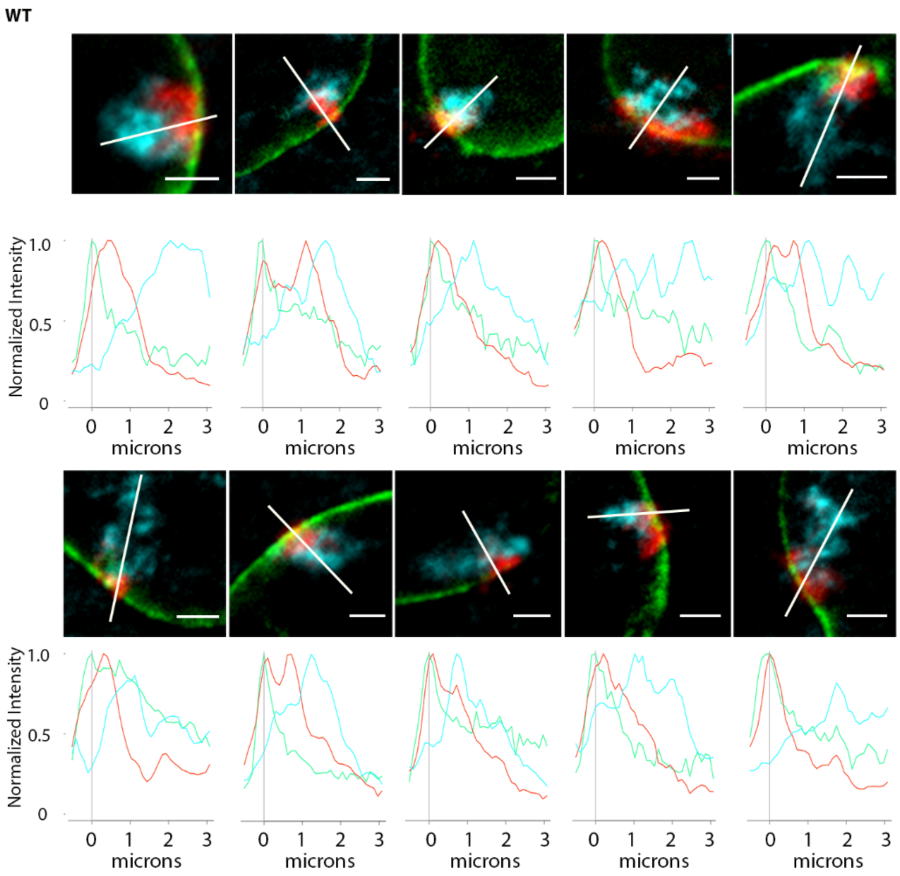

Supplemental Figure 3.4: *Chromosome conformation paints for chromosome 11 in WT (untreated) MEFs*. Representative images of chromosome 11 conformation paints to chromosome nonLADs (cyan) LADs (red) lamin B1 (green). Normalized fluorescence intensity histogram plots for chromosome 11 territories in wild type MEFs, plotted from the nuclear lamina (0μm) to 3μm into the nucleus. The line each plot travels through is represented by a white line. Scale bar = 2μm.

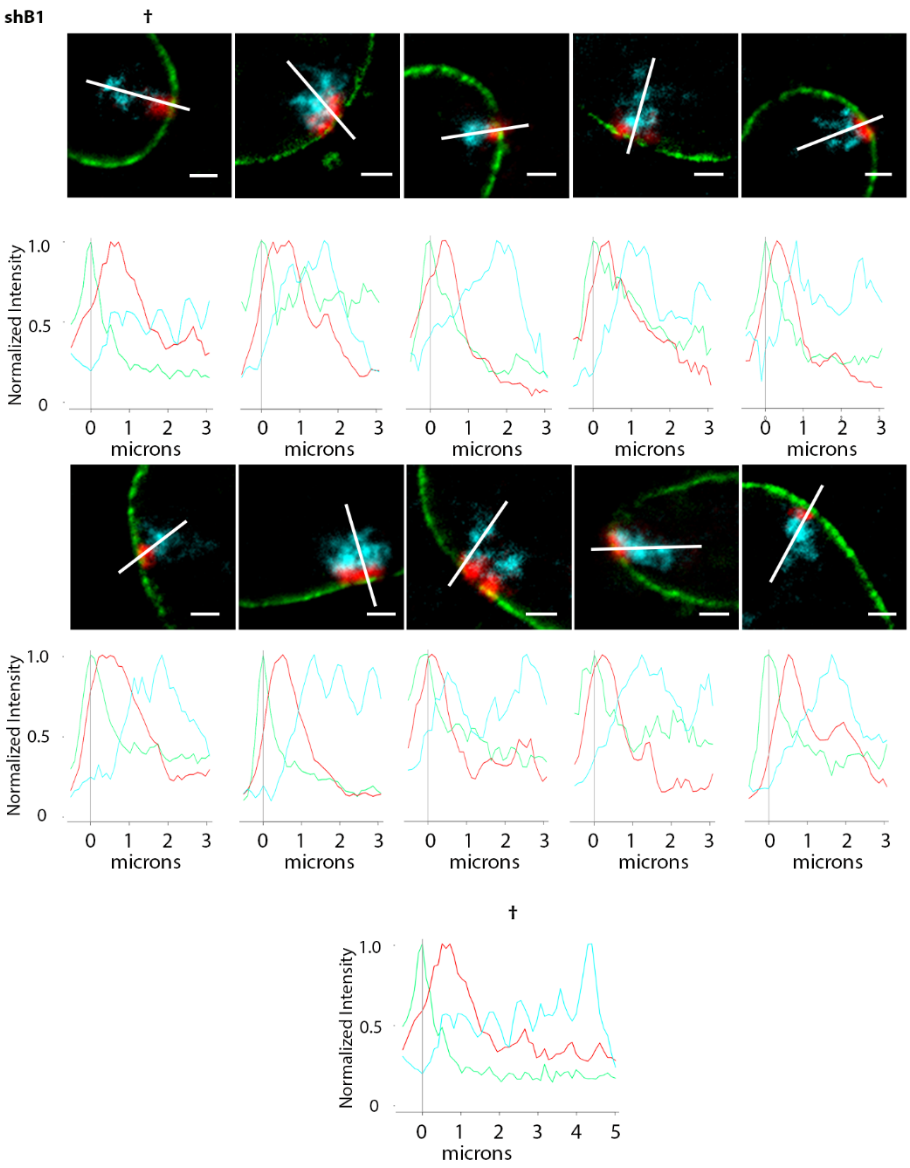

Supplemental Figure 3.5: Lamin B1 depleted cells have normal LAD/nonLAD configuration. Representative images of chromosome 11 conformation paints to chromosome nonLADs (cyan) LADs (red) lamin A/C (green). Normalized fluorescence intensity histogram plots for chromosome 11 territories in shLB1 treated MEFs, plotted from the nuclear lamina (0μm) to 3μm into the nucleus. The line each plot travels through is represented by a white line. Scale bar = 2μm.

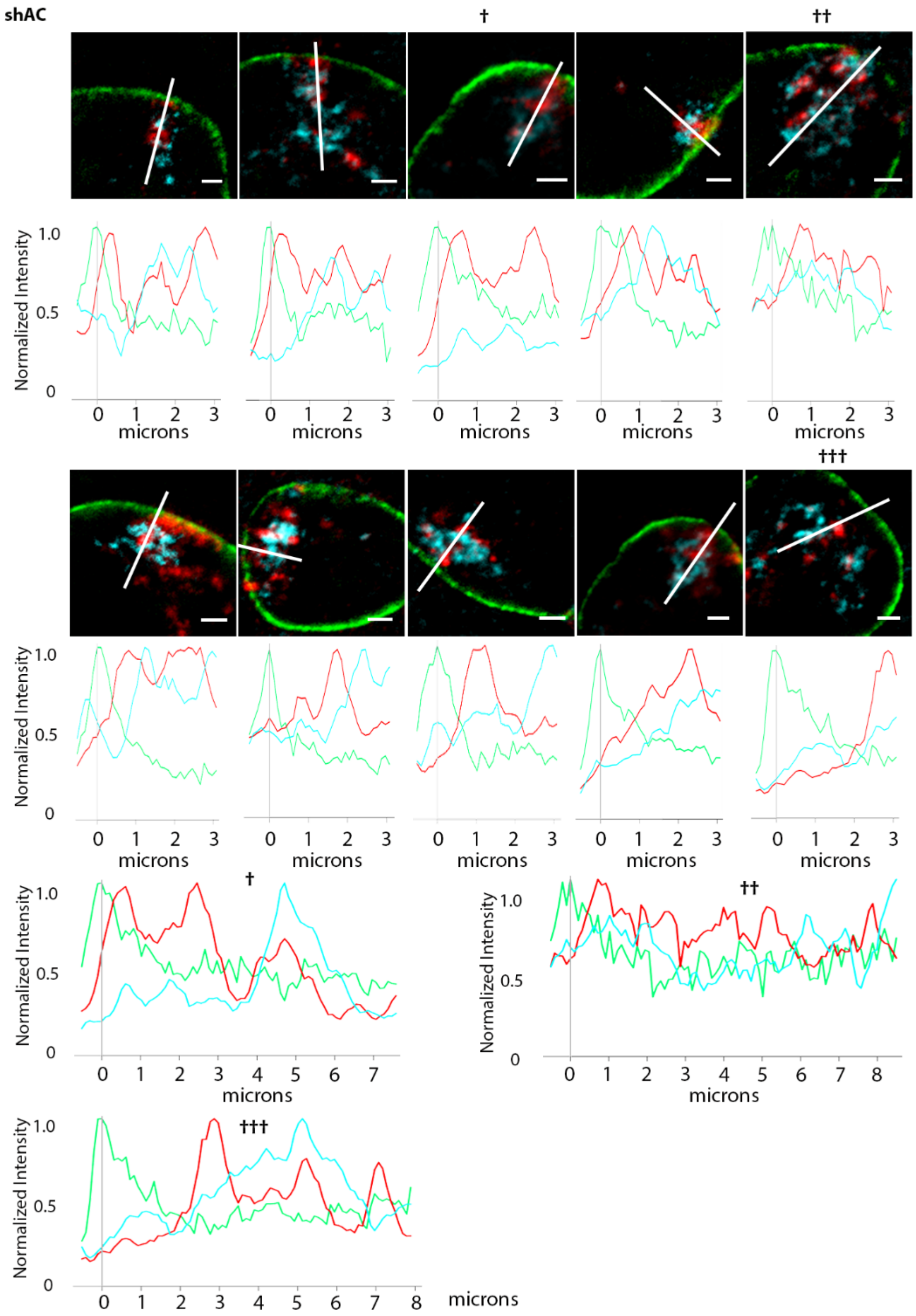

Supplemental Figure 3.6: Lamin A/C depleted cells show wide-spread disruption of LAD and nonLAD organization. Representative images of chromosome 11 conformation paints to chromosome nonLADs (cyan) LADs (red) lamin B1 (green). Normalized fluorescence intensity histogram plots for chromosome 11 territories in shAC treated MEFs, plotted from the nuclear lamina (0μm) to 3μm into the nucleus. The territories marked with †, †

† , or † † † were plotted beyond 3μm to better capture the disposition of LADs/nonLADs. The line each plot travels through is represented by a white line. Scale bar = 2μm.

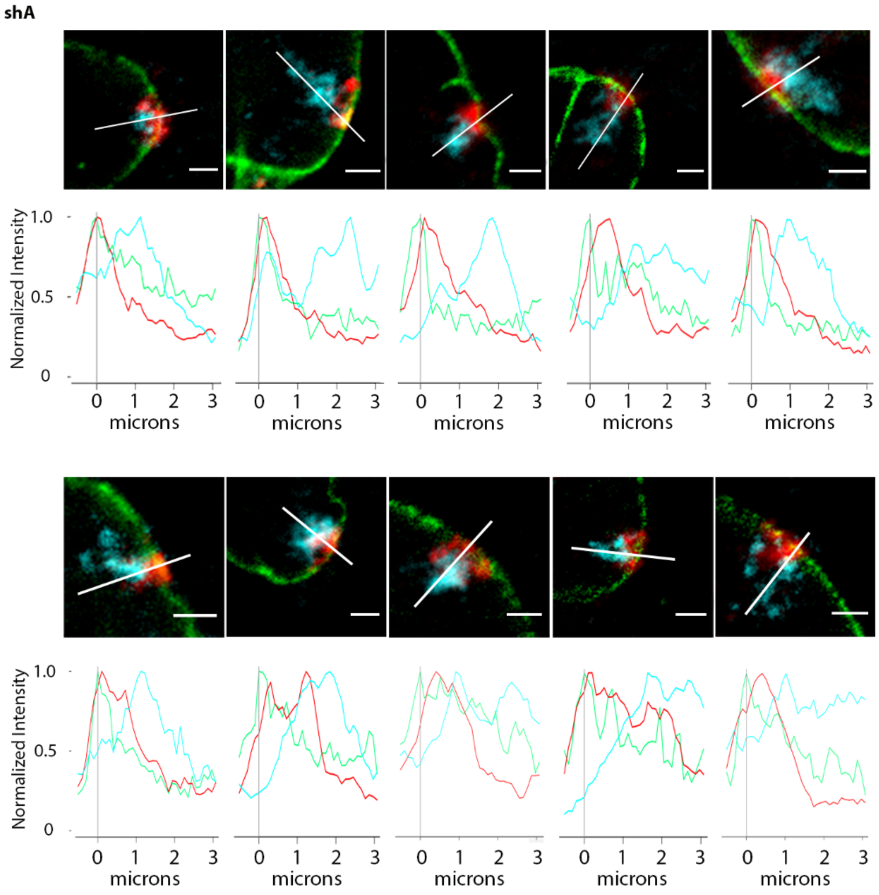

Supplemental Figure 3.7: Lamin A (only) depleted cells have normal LAD/nonLAD configuration. Representative images of chromosome 11 conformation paints to chromosome nonLADs (cyan) LADs (red) lamin B1 (green). Normalized fluorescence intensity histogram plots for chromosome 11 territories in shA treated MEFs, plotted from the nuclear lamina (0μm) to 3μm into the nucleus. The line each plot travels through is represented by a white line. Scale bar = 2μm.

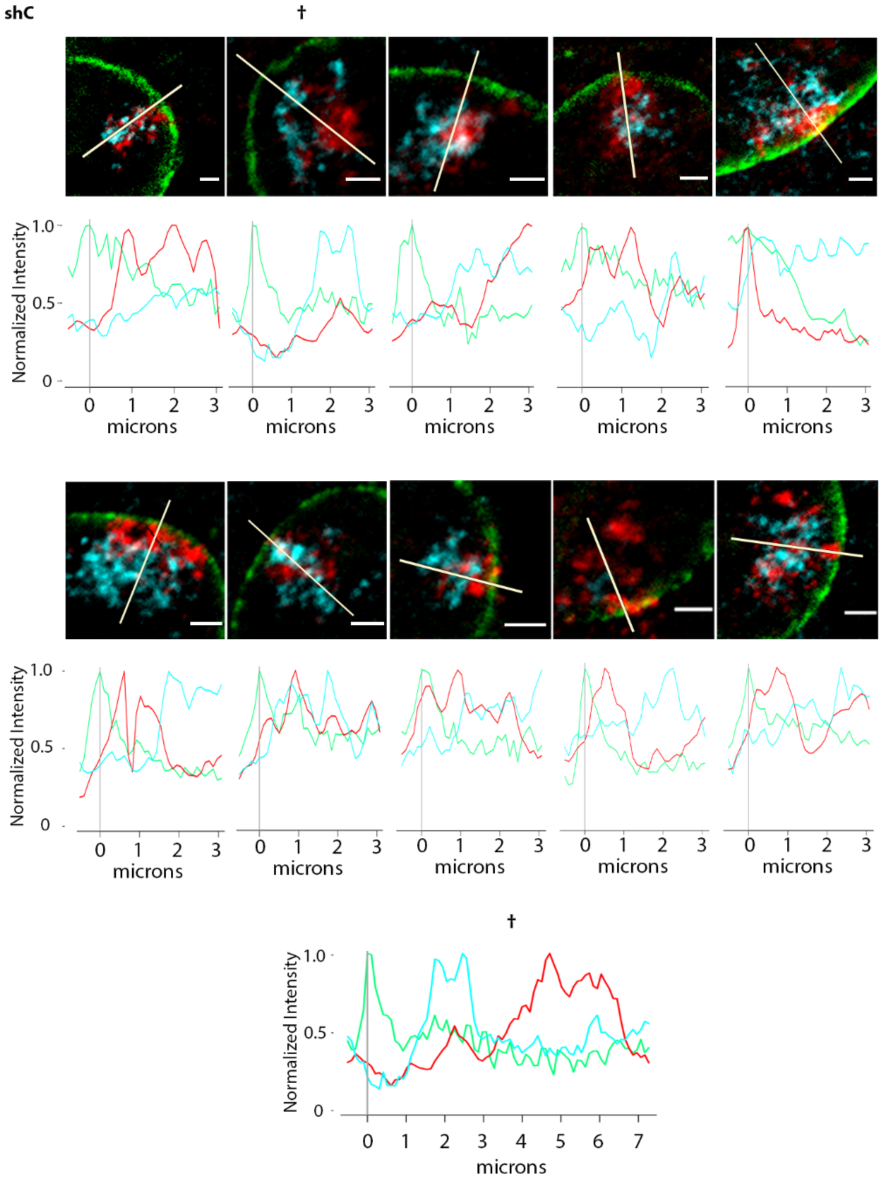

Supplemental Figure 3.8: Lamin C (only) depleted cells show wide-spread disruption of LAD and nonLAD organization. Representative images of chromosome 11 conformation paints to chromosome nonLADs (cyan) LADs (red) lamin B1 (green). Normalized fluorescence intensity histogram plots for chromosome 11 territories in shC treated MEFs, plotted from the nuclear lamina (0μm) to 3μm into the nucleus. The territory marked with † was plotted beyond 3μm to better display LAD and nonLAD signals. The line each plot travels through is represented by a white line. Scale bar = 2μm.

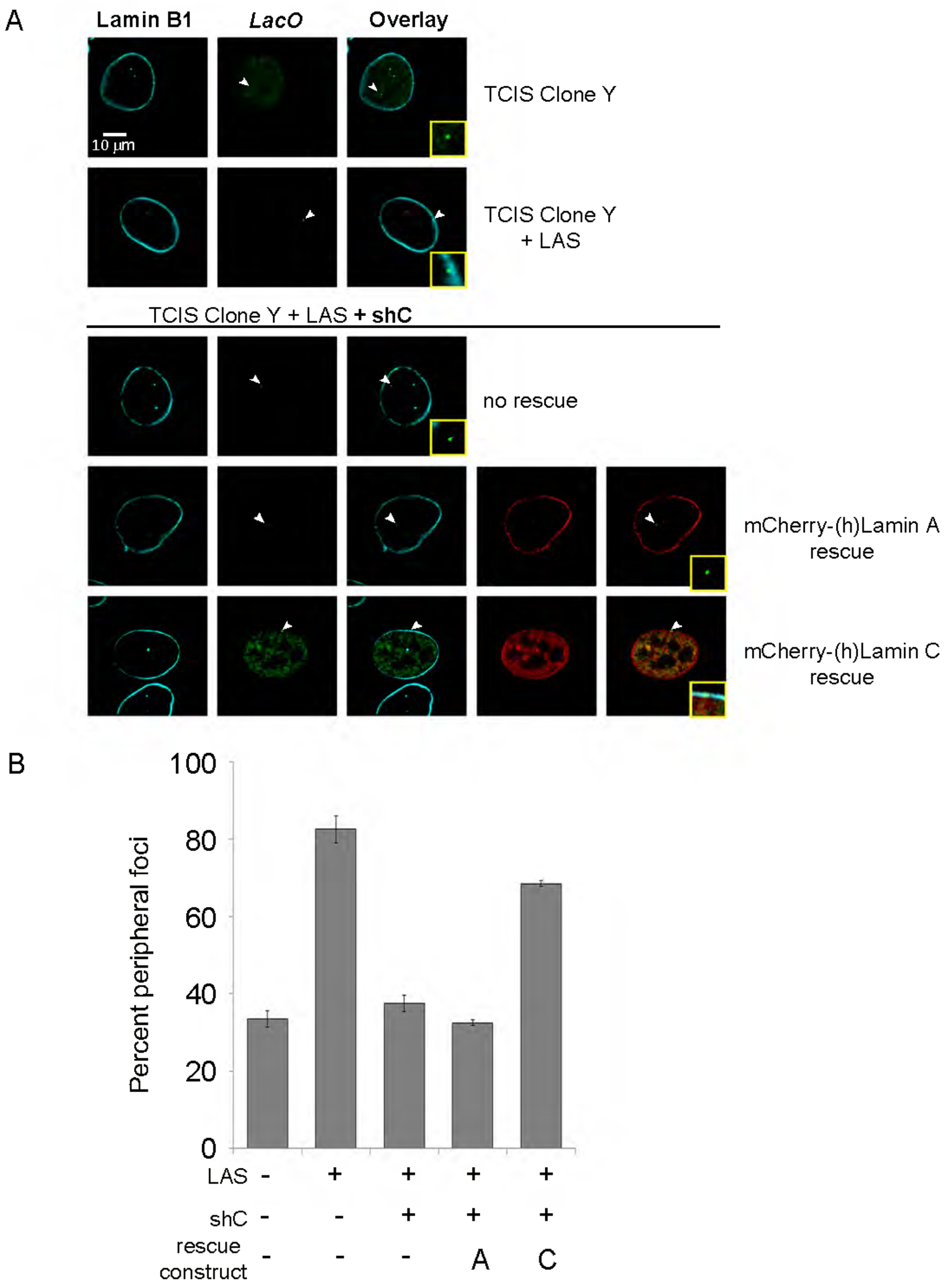

Supplemental Figure 3.9: LAS localization can be rescued by expression of human lamin C (A) Representative images showing the disposition of lacO arrays (arrowheads, green), lamin A or C respectively (red), and lamin B1 (cyan) in the TCIS clone Y. The inset shows

300× magnification. (B) Quantification of peripheral association was determined by the overlap of EGFP-LacI foci and lamin B1 ($n \geq 50$). Error bars indicate SD. Asterisks for rescue experiment indicate significance of $p \leq 0.001$, not significant is indicated by n.s.

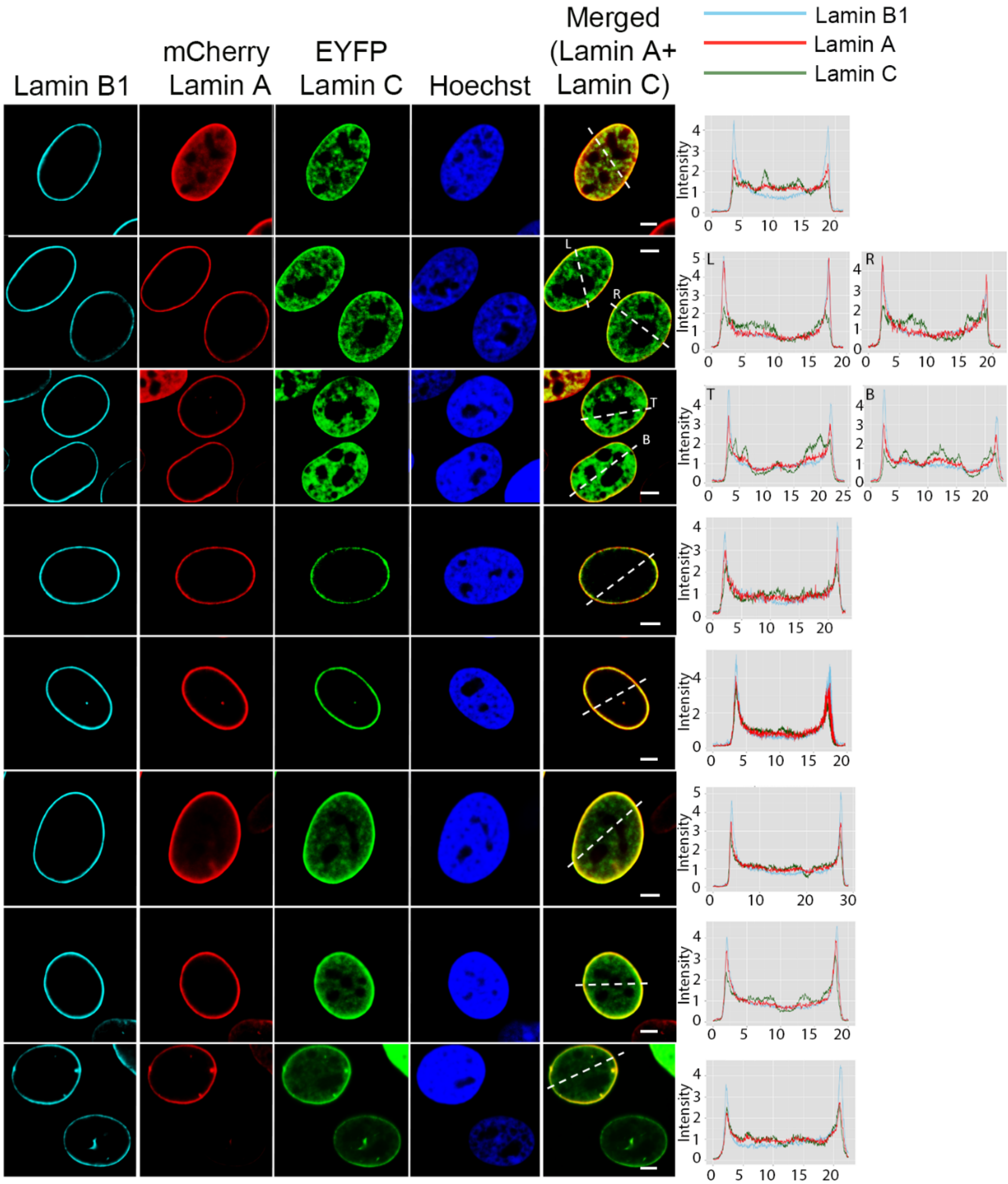
Lamin B1
mCherry Lamin A
EYFP Lamin C
Hoechst
Merged (Lamin A+ Lamin C)
Lamin B1
Lamin A
Lamin C
L
R
T
B
Intensity
0 5 10 15 20
0 5 10 15 20 25
0 10 20 30

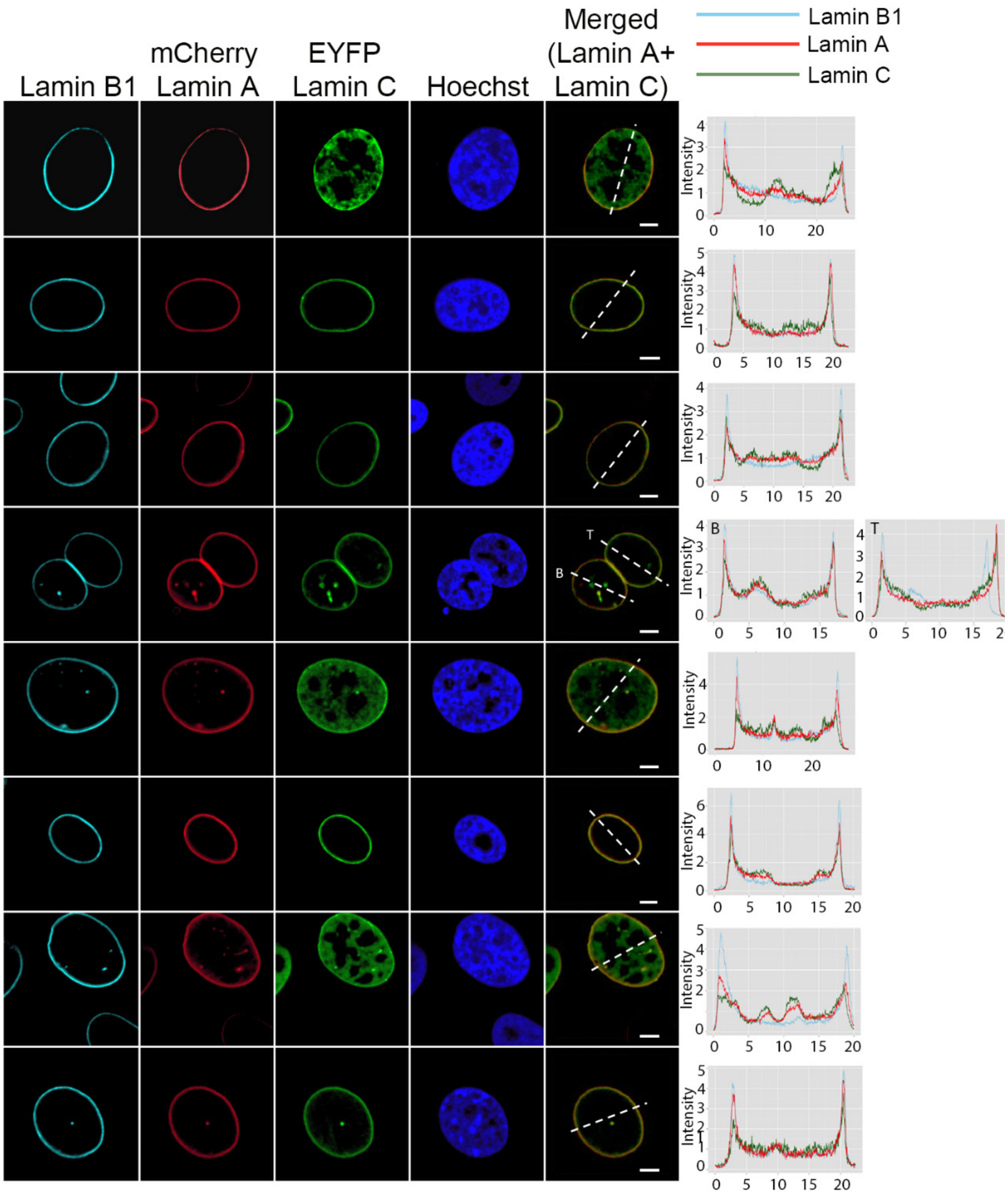

Supplemental Figure 3.10: All 3 lamin isotypes localize to the periphery during interphase. Representative images of interphase nuclei anti-lamin B1 (cyan) mCherry-lamin A(red) EYFP-lamin C (green) Hoechst (blue). Fluorescence intensity histogram plots for lamin B1 (cyan), lamin A (red) and lamin C (green) along the indicated white dotted line in merge. Scale bar = 5μm.

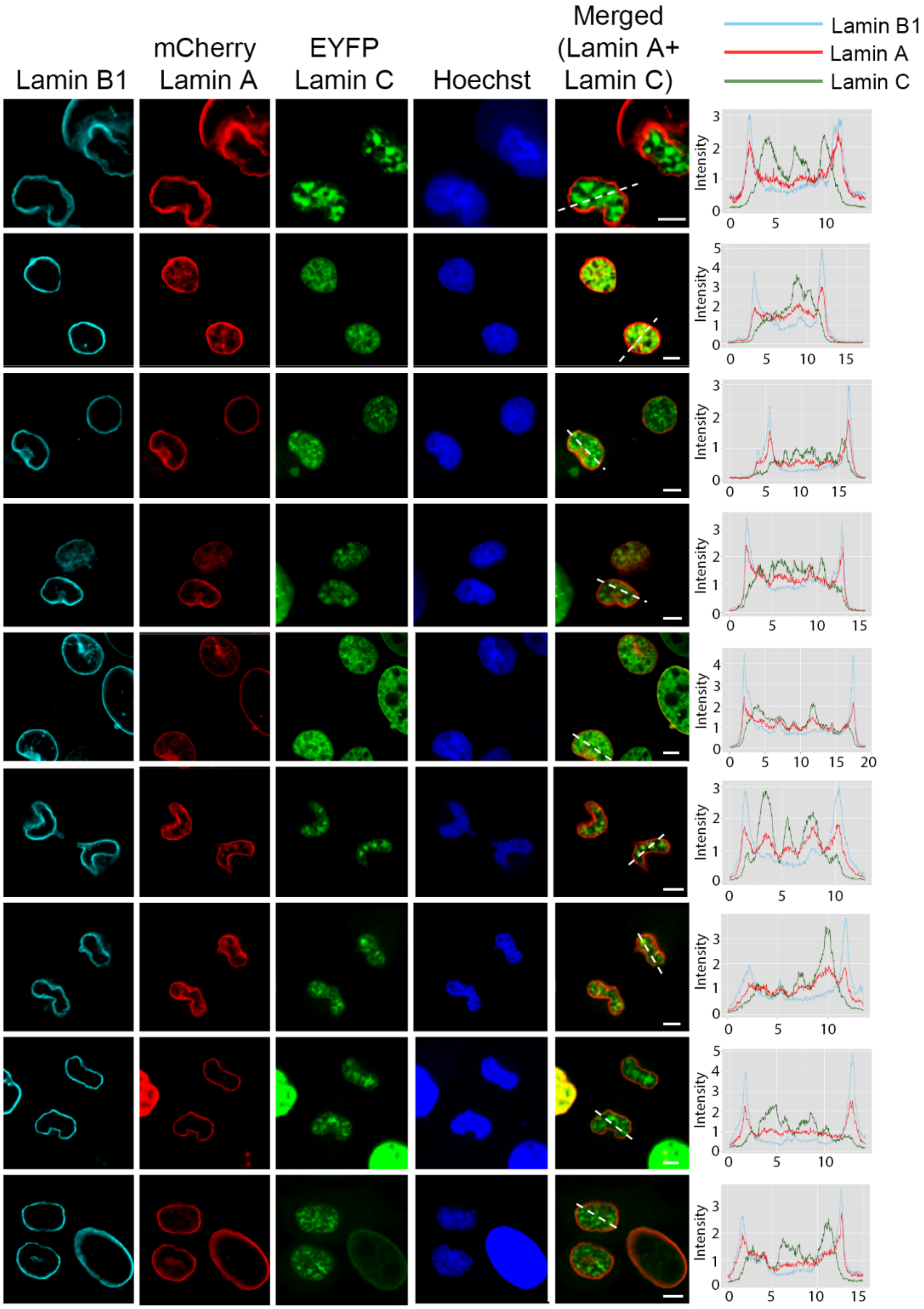
Lamin B1
mCherry Lamin A
EYFP Lamin C
Hoechst
Merged (Lamin A+ Lamin C)
Lamin B1
Lamin A
Lamin C
Intensity
0 1 2 3
0 5 10
Intensity
0 1 2 3 4 5
0 5 10 15
Intensity
0 1 2 3
0 5 10 15
Intensity
0 1 2 3
0 5 10 15
Intensity
0 1 2 3 4
0 5 10 15 20
Intensity
0 1 2 3
0 5 10
Intensity
0 1 2 3
0 5 10
Intensity
0 1 2 3 4 5
0 5 10
Intensity
0 1 2 3
0 5 10 15

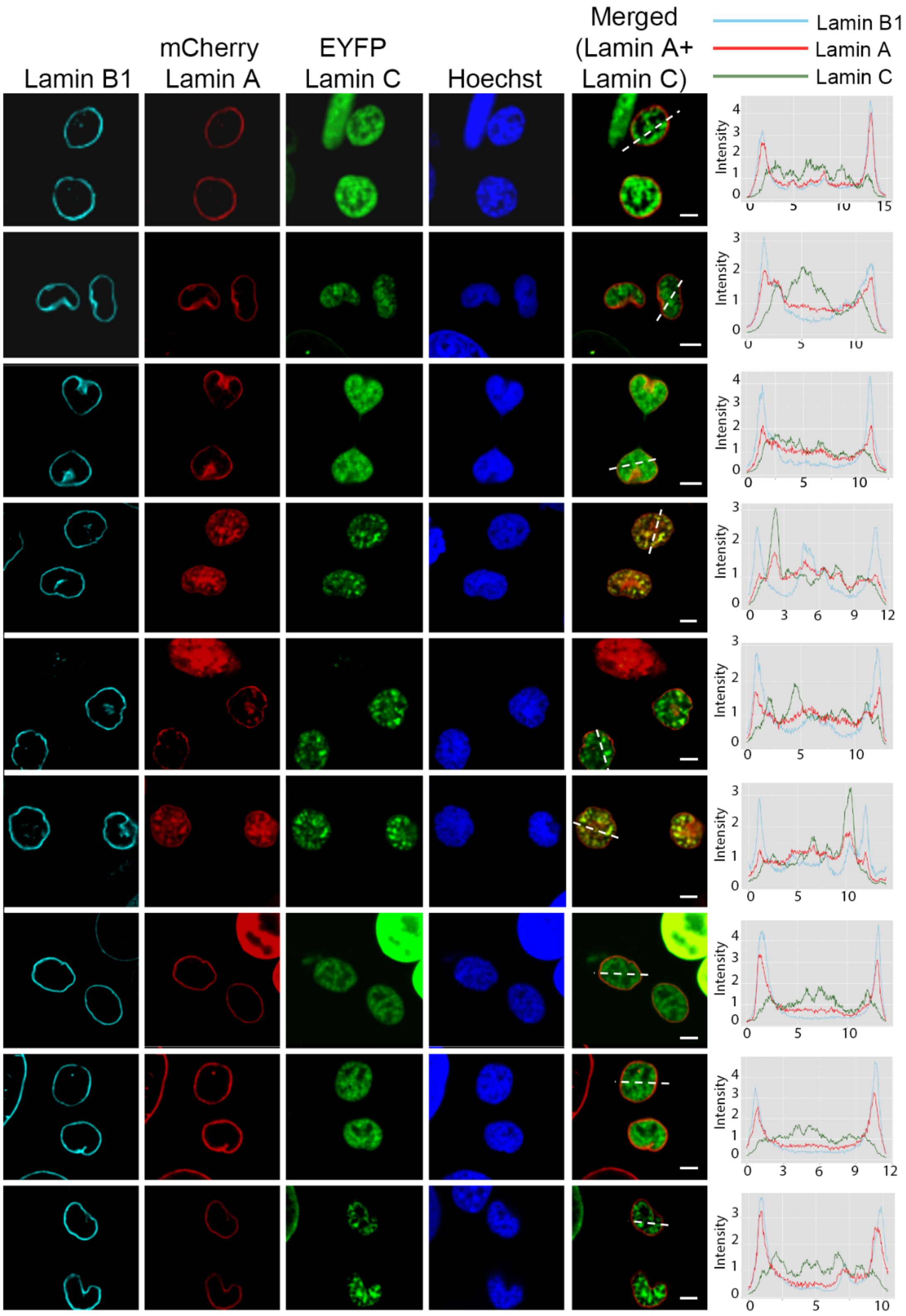

Supplemental Figure 3.11: Differential localization of lamin B1, lamin A and lamin C at mitotic exit (telophase and early G1). Representative images of telophase and early G1 nuclei anti-lamin B1 (cyan) mCherry-lamin A (red) EYFP-lamin C (green) Hoechst (blue). Fluorescence intensity histogram plots for lamin B1 (cyan), lamin A (red) and lamin C green) along the indicated white dotted line in merge. Scale bar = 5μm.

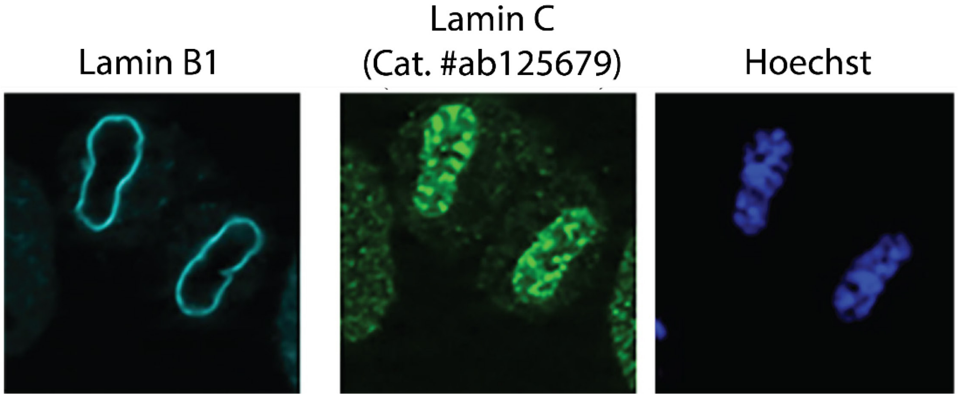

Supplemental Figure 3.12: Antibody staining for lamin C shows the same localization as fluorescently tagged construct. Representative image of telophase/early G1 nucleus stained using antibody to lamin C (green, ab125679), antibody to lamin B1 (cyan) and Hoechst (blue).

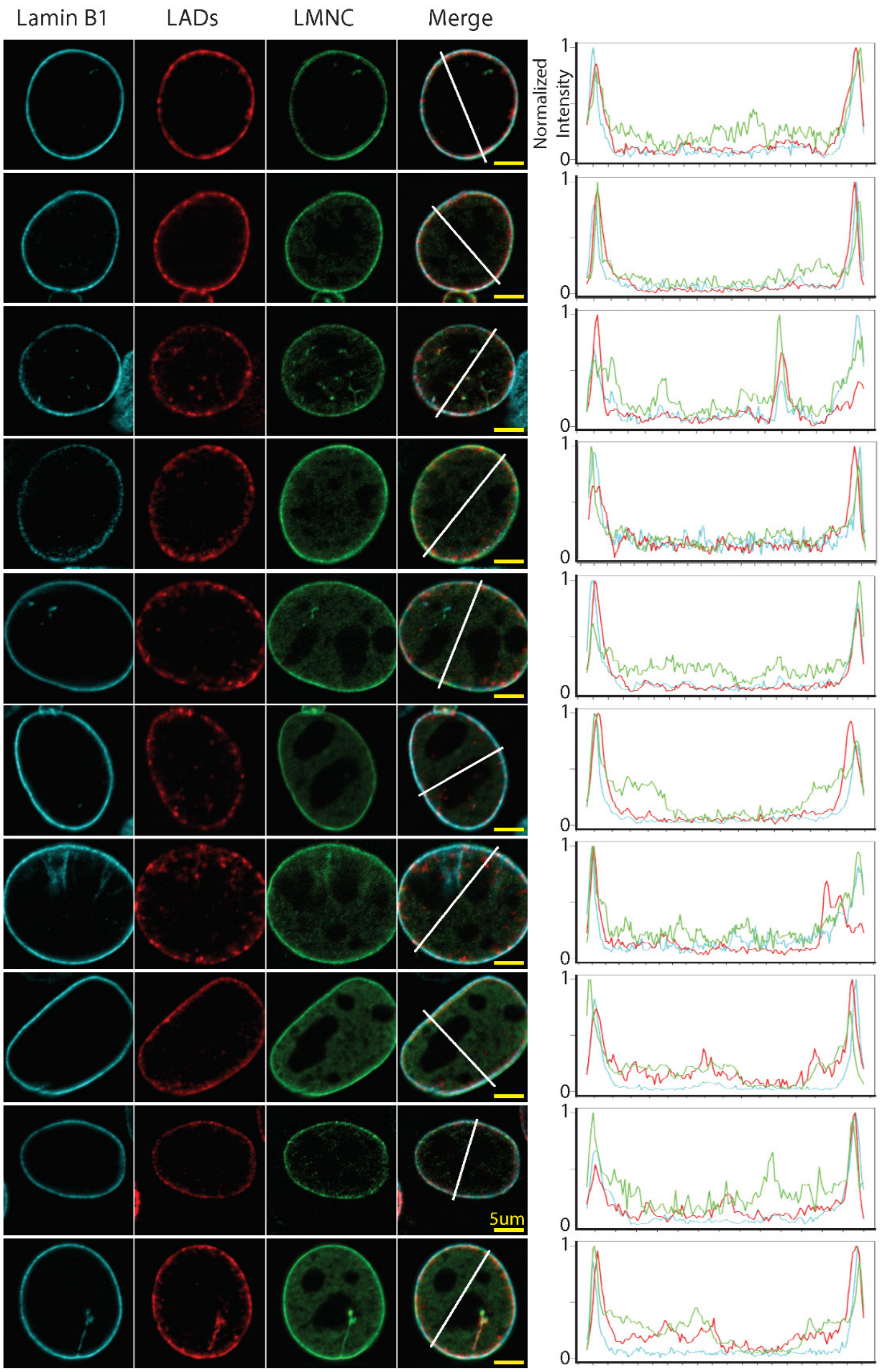

Supplemental Figure 3.13: LADs and lamin C show peripheral localization during interphase. Representative images of interphase nuclei anti-lamin B1 (cyan) LAD-tracer (red) EYFP-lamin C (green). Normalized fluorescence intensity histogram plots for lamin

B1 (cyan), LADs (red) and lamin C (green) along the indicated white line. Yellow scale bar = 5μm.

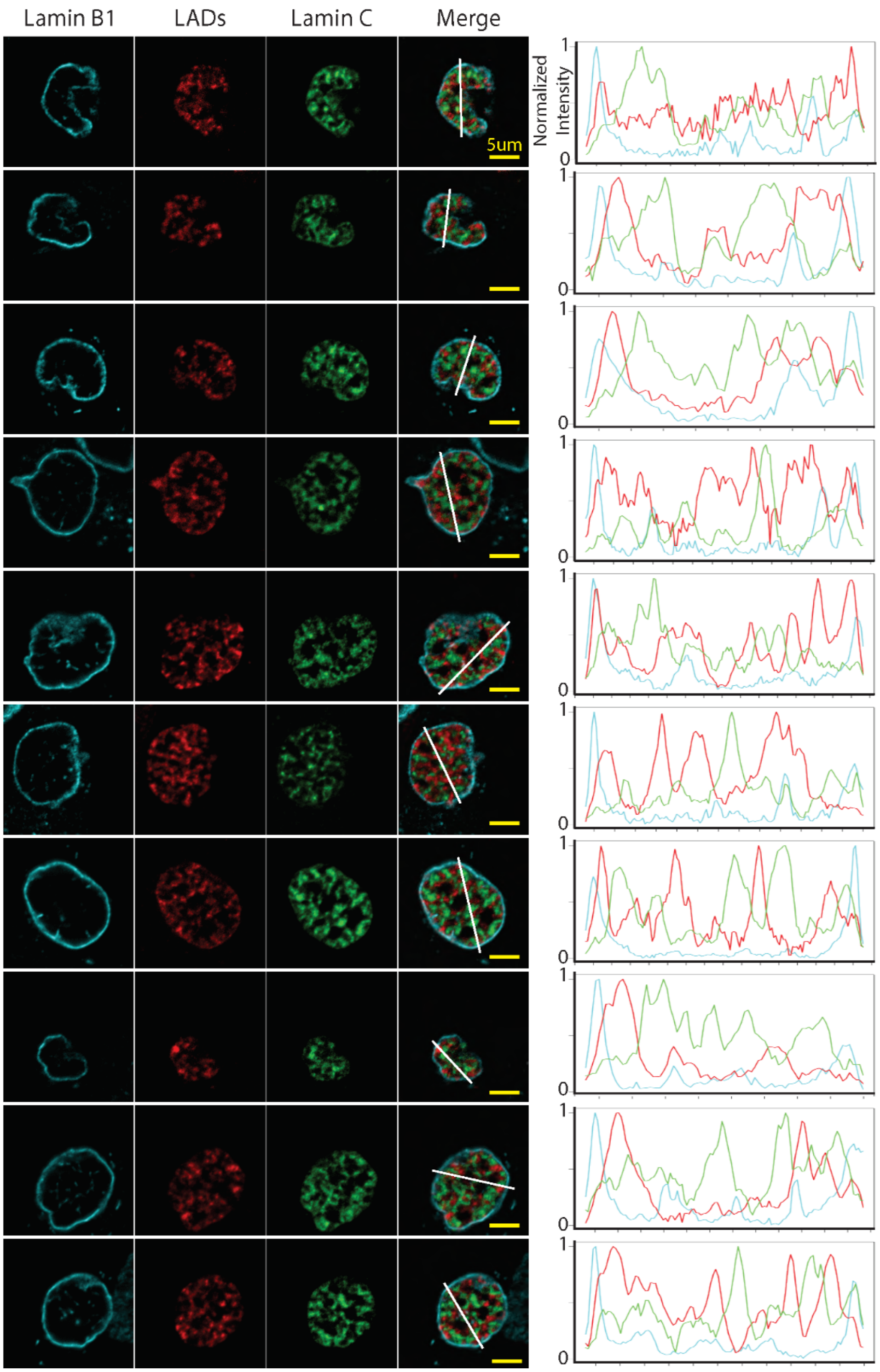
Lamin B1
LADs
Lamin C
Merge
5um
Normalized Intensity
1
0

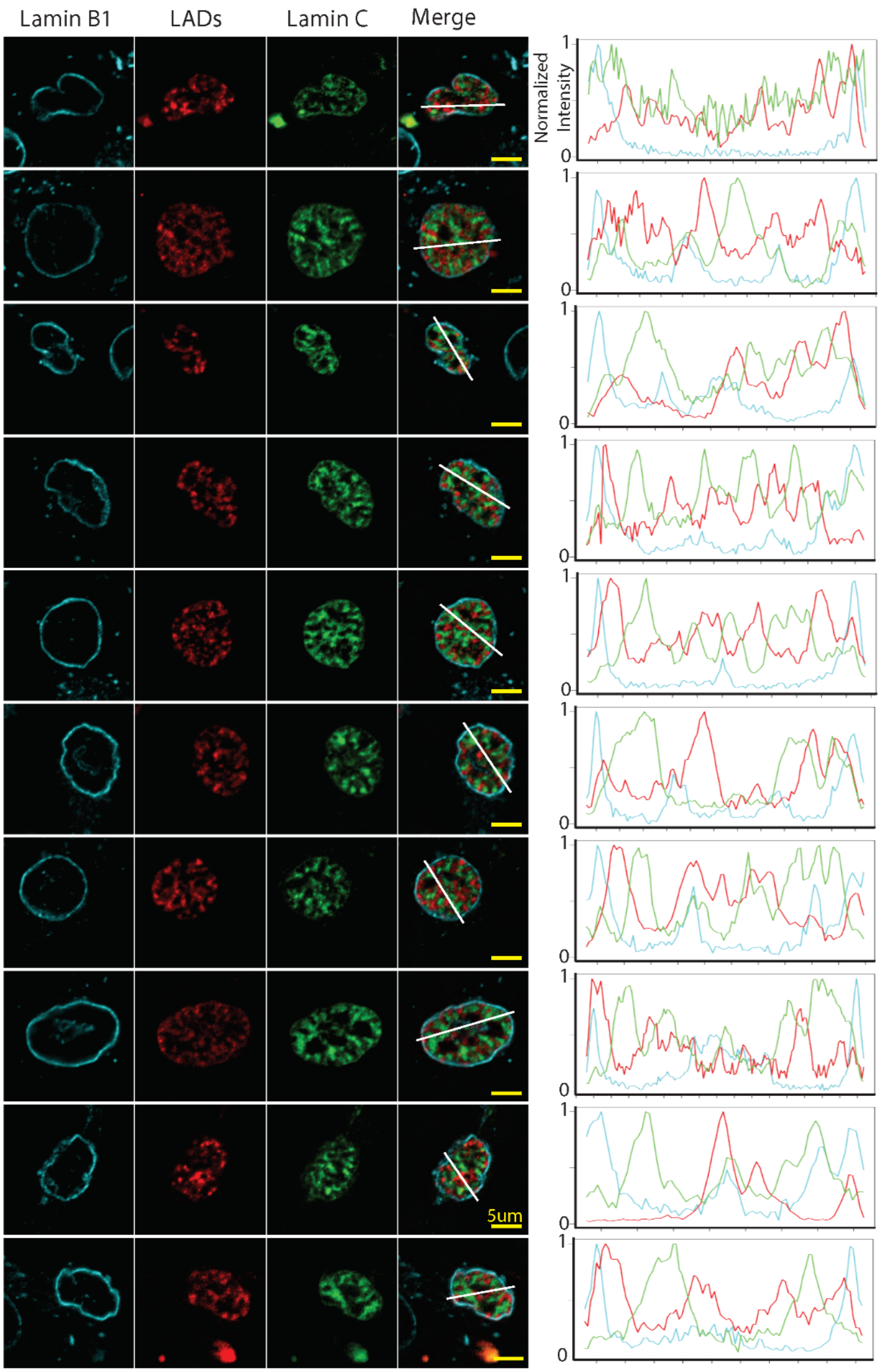

Supplemental Figure 3.14: LADs and lamin C show nucleoplasmic localization during telophase/early G1 but do not colocalize. Representative images of telophase or early G1 nuclei anti-lamin B1 (cyan) LAD-tracer (red) EYFP-lamin C (green). Normalized fluorescence intensity histogram plots for lamin B1 (cyan), LADs (red) and lamin C (green) along the indicated white line. Yellow scale bar = 5μm.

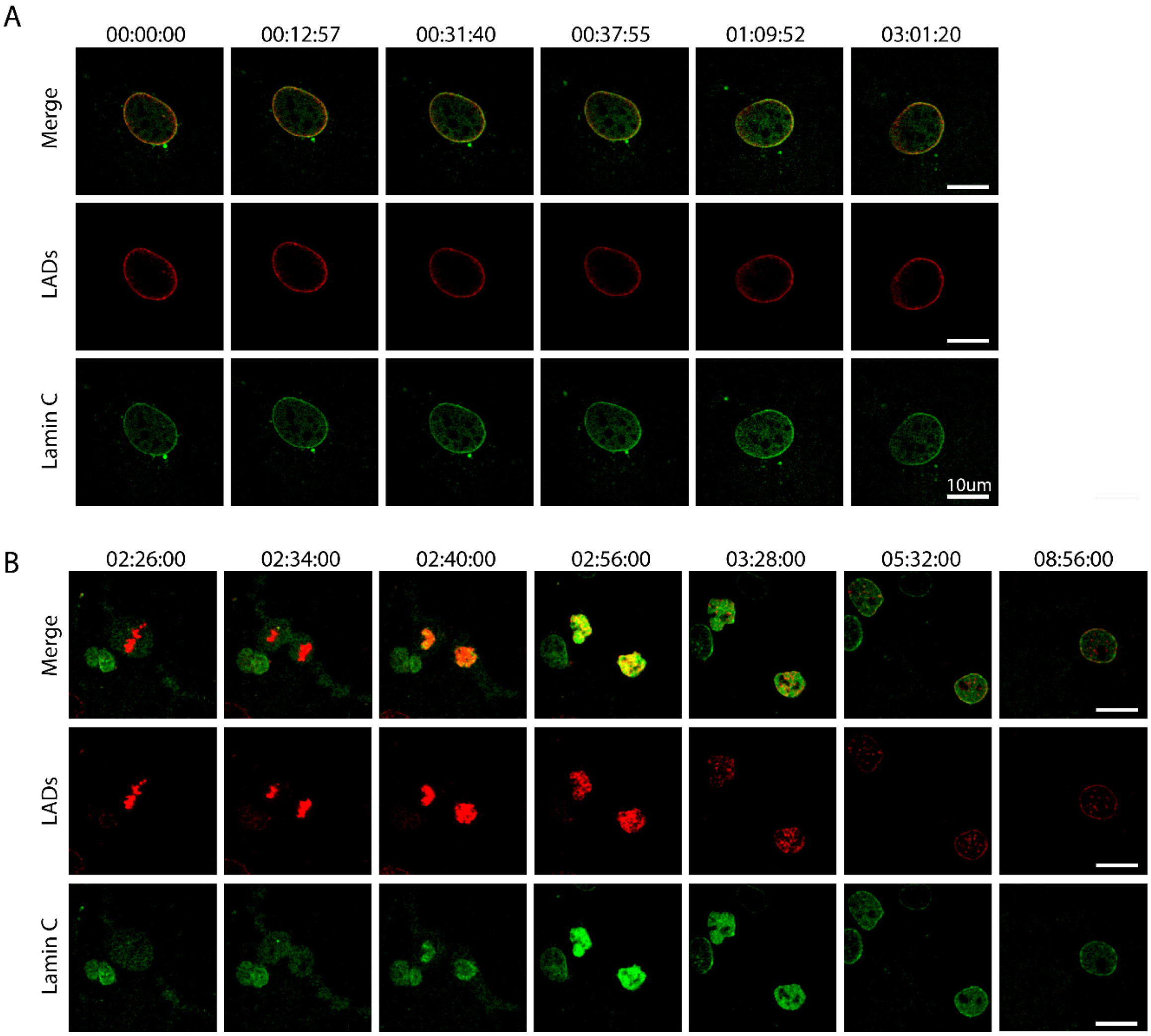

Supplemental Figure 3.15: Lamin C and LADs resolve concurrently during G1. (A) Still images from time lapse movie 2 of LADs (red) EYFP-lamin C (green) during interphase shown over a similar time scale to movies 1 and 3. Scale Bar is 20μm. (B) Still images from time lapse movie 4 of LADs (red) EYFP-lamin C (green) during mitosis. Scale bar is 20μm. Images were chosen to exemplify certain stages (metaphase, anaphase, telophase, early G1, partially resolved, fully resolved, mid G1). This movie extends further in time than other movies showing how LAD configuration continues to become tighter to the lamina well into G1 phase.

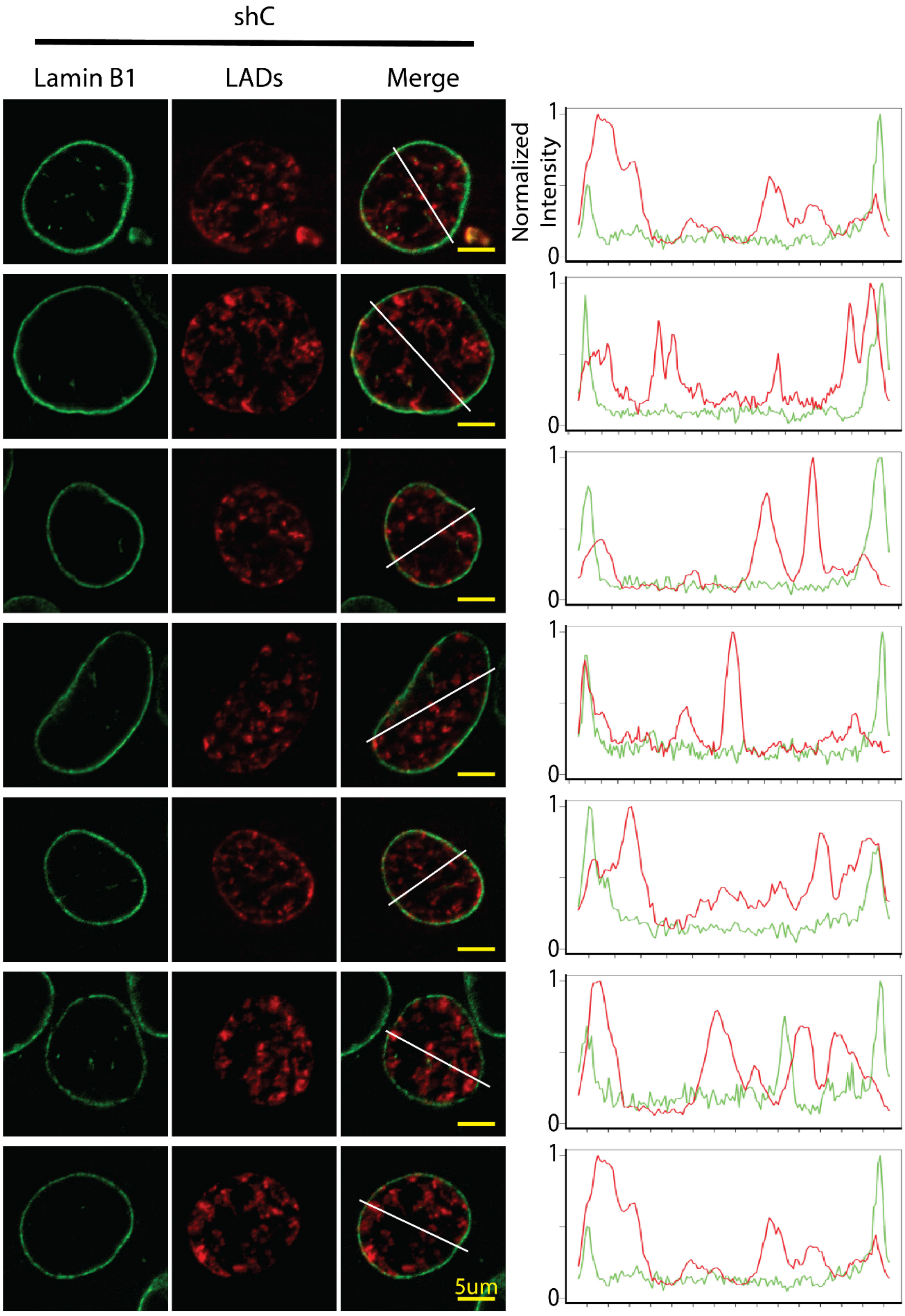
shC
Lamin B1
LADs
Merge
Normalized Intensity
1
0
5um

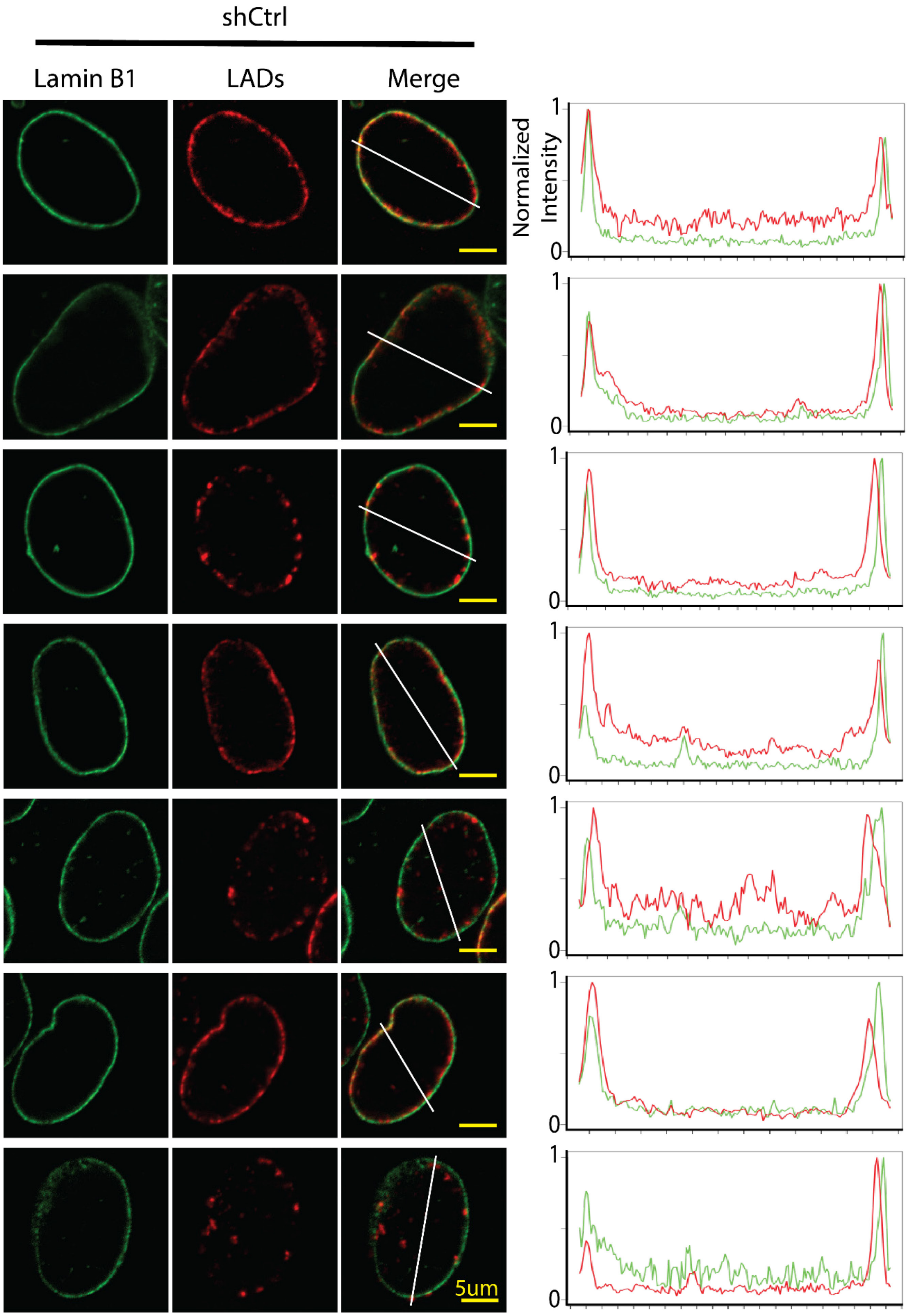
shCtrl
Lamin B1
LADs
Merge
Normalized Intensity
1
0
5um

Supplemental Figure 3.16: LADs form network-like structures after cell division in the absence of lamin C. Representative images of cells harboring the LAD-tracer system that were transduced with a either a control short hairpin RNA or a short hairpin RNA to lamin C. Lamin B1 (green) LADs (red). Normalized fluorescence intensity histogram plots for lamin B1 (green) and LAD-tracer (red) along the indicated white line. Yellow scale bar = 5μm.

Bibliography

1. Greil F, Moorman C, van Steensel B. DamID: mapping of in vivo protein-genome interactions using tethered DNA adenine methyltransferase. Methods Enzymol. 2006;410: 342–359.

2. Vogel MJ, Peric-Hupkes D, van Steensel B. Detection of in vivo protein–DNA interactions using DamID in mammalian cells. Nat Protoc. 2007;2: 1467–1478.

3. Dekker J, Rippe K, Dekker M, Kleckner N. Capturing chromosome conformation. Science. 2002;295: 1306–1311.

4. Dixon JR, Selvaraj S, Yue F, Kim A, Li Y, Shen Y, et al. Topological domains in mammalian genomes identified by analysis of chromatin interactions. Nature. 2012;485: 376–380.

5. Lieberman-Aiden E, van Berkum NL, Williams L, Imakaev M, Ragoczy T, Telling A, et al. Comprehensive mapping of long-range interactions reveals folding principles of the human genome. Science. 2009;326: 289–293.

6. Rao SSP, Huntley MH, Durand NC, Stamenova EK, Bochkov ID, Robinson JT, et al. A 3D map of the human genome at kilobase resolution reveals principles of chromatin looping. Cell. 2014;159: 1665–1680.

7. Phillips-Cremins JE, Sauria MEG, Sanyal A, Gerasimova TI, Lajoie BR, Bell JSK, et al. Architectural Protein Subclasses Shape 3D Organization of Genomes during Lineage Commitment. Cell. 2013;153: 1281–1295.

8. Luperchio TR, Sauria MEG, Wong X, Gaillard M-C, Tsang P, Pekrun K, et al. Chromosome Conformation Paints Reveal the Role of Lamina Association in Genome Organization and Regulation. bioRxiv. 2017. p. 122226. doi:10.1101/122226

9. Falk M, Feodorova Y, Naumova N, Imakaev M, Lajoie BR, Leonhardt H, et al. Heterochromatin drives compartmentalization of inverted and conventional nuclei. Nature. 2019. pp. 395–399. doi:10.1038/s41586-019-1275-3

10. Schwarzer W, Abdennur N, Goloborodko A, Pekowska A, Fudenberg G, Loe-Mie Y, et al. Two independent modes of chromatin organization revealed by cohesin removal. Nature. 11 02, 2017;551: 51–56.

11. Harr JC, Luperchio TR, Wong X, Cohen E, Wheelan SJ, Reddy KL. Directed targeting of chromatin to the nuclear lamina is mediated by chromatin state and A-type lamins. J Cell Biol. 2015;208: 33–52.

12. Luperchio TR, Sauria MEG, Hoskins VE, Wong X, DeBoy E, Gaillard M-C, et al. The repressive genome compartment is established early in the cell cycle before forming the lamina associated domains. bioRxiv. 2018. p. 481598. doi:10.1101/481598

13. Guelen L, Pagie L, Brasset E, Meuleman W, Faza MB, Talhout W, et al. Domain organization of human chromosomes revealed by mapping of nuclear lamina interactions. Nature. 2008;453: 948–951.

14. Towbin BD, González-Aguilera C, Sack R, Gaidatzis D, Kalck V, Meister P, et al. Step-wise methylation of histone H3K9 positions heterochromatin at the nuclear periphery. Cell. 2012;150: 934–947.

15. Falk M, Feodorova Y, Naumova N, Imakaev M, Lajoie BR, Leonhardt H, et al. Heterochromatin drives compartmentalization of inverted and conventional nuclei. Nature. 2019. pp. 395–399. doi:10.1038/s41586-019-1275-3

16. Larson AG, Elnatan D, Keenen MM, Trnka MJ, Johnston JB, Burlingame AL, et al. Liquid droplet formation by HP1α suggests a role for phase separation in heterochromatin. Nature. 2017;547: 236–240.

17. Strom AR, Emelyanov AV, Mir M, Fyodorov DV, Darzacq X, Karpen GH. Phase separation drives heterochromatin domain formation. Nature. 2017;547: 241–245.

18. Bian Q, Khanna N, Alvikas J, Belmont AS. β-Globin cis-elements determine differential nuclear targeting through epigenetic modifications. J Cell Biol. 2013;203: 767–783.

19. Peric-Hupkes D, Meuleman W, Pagie L, Bruggeman SWM, Solovei I, Brugman W, et al. Molecular maps of the reorganization of genome-nuclear lamina interactions during differentiation. Mol Cell. 2010;38: 603–613.

20. Kind J, Pagie L, de Vries SS, Nahidiazar L, Dey SS, Bienko M, et al. Genome-wide maps of nuclear lamina interactions in single human cells. Cell. 2015;163: 134–147.

21. Leemans C, van der Zwalm MCH, Brueckner L, Comoglio F, van Schaik T, Pagie L, et al. Promoter-Intrinsic and Local Chromatin Features Determine Gene Repression in LADs. Cell. 2019;177: 852–864.e14.

22. Chen S, Luperchio TR, Wong X, Doan EB, Byrd AT, Roy Choudhury K, et al. A Lamina-Associated Domain Border Governs Nuclear Lamina Interactions, Transcription, and Recombination of the Tcrb Locus. Cell Rep. 2018;25: 1729–1740.e6.

23. Zheng X, Hu J, Yue S, Kristiani L, Kim M, Sauria M, et al. Lamins Organize the Global Three-Dimensional Genome from the Nuclear Periphery. Mol Cell. 2018;71: 802–815.e7.

24. Turgay Y, Eibauer M, Goldman AE, Shimi T, Khayat M, Ben-Harush K, et al. The molecular architecture of lamins in somatic cells. Nature. 2017;543: 261–264.

25. Shimi T, Kittisopikul M, Tran J, Goldman AE, Adam SA, Zheng Y, et al. Structural organization of nuclear lamins A, C, B1, and B2 revealed by superresolution microscopy. Mol Biol Cell. 2015;26: 4075–4086.

26. Solovei I, Wang AS, Thanisch K, Schmidt CS, Krebs S, Zwerger M, et al. LBR and lamin A/C sequentially tether peripheral heterochromatin and inversely regulate differentiation. Cell. 2013;152: 584–598.

27. Simon DN, Wilson KL. Partners and post-translational modifications of nuclear lamins. Chromosoma. 2013;122: 13–31.

28. Wong X, Hoskins VE, Harr JC, Gordon M, Reddy KL. Lamin C regulates genome organization after mitosis. doi:10.1101/2020.07.28.213884

29. Amendola M, van Steensel B. Nuclear lamins are not required for lamina-associated domain organization in mouse embryonic stem cells. EMBO Rep. 2015-5;16: 610–617.

30. Pascual-Reguant L, Blanco E, Galan S, Le Dily F, Cuartero Y, Serra-Bardenys G, et al. Lamin B1 mapping reveals the existence of dynamic and functional euchromatin lamin B1 domains. Nat Commun. 2018;9: 3420.

31. González-Cruz RD, Dahl KN, Darling EM. The Emerging Role of Lamin C as an Important LMNA Isoform in Mechanophenotype. Front Cell Dev Biol. 2018;6: 151.

32. Falk M, Feodorova Y, Naumova N, Imakaev M, Lajoie BR, Leonhardt H, et al. Heterochromatin drives compartmentalization of inverted and conventional nuclei. Nature. 2019. pp. 395–399. doi:10.1038/s41586-019-1275-3

33. Mattioli E, Andrenacci D, Garofalo C, Prencipe S, Scotlandi K, Remondini D, et al. Altered modulation of lamin A/C-HDAC2 interaction and p21 expression during oxidative stress response in HGPS. Aging Cell. 2018;17: e12824.

34. Fong LG, Ng JK, Lammerding J, Vickers TA, Meta M, Coté N, et al. Prelamin A and lamin A appear to be dispensable in the nuclear lamina. J Clin Invest. 2006;116: 743–752.

35. Xie W, Chojnowski A, Boudier T, Lim JSY, Ahmed S, Ser Z, et al. A-type Lamins Form Distinct Filamentous Networks with Differential Nuclear Pore Complex Associations. Curr Biol. 2016;26: 2651–2658.

36. de Toledo M, Lopez-Mejia IC, Cavelier P, Pratlong M, Barrachina C, Gromada X, et al. Lamin C Counteracts Glucose Intolerance in Aging, Obesity, and Diabetes Through β-Cell Adaptation. Diabetes. 2020;69: 647–660.

37. Santi S, Cenni V, Capanni C, Lattanzi G, Mattioli E. PCAF Involvement in Lamin A/C-HDAC2 Interplay during the Early Phase of Muscle Differentiation. Cells. 2020;9. doi:10.3390/cells9071735

38. Rønningen T, Shah A, Oldenburg AR, Vekterud K, Delbarre E, Moskaug JØ, et al. Prepatterning of differentiation-driven nuclear lamin A/C-associated chromatin domains by GlcNAcylated histone H2B. Genome Res. 2015;25: 1825–1835.

39. Gesson K, Rescheneder P, Skoruppa MP, von Haeseler A, Dechat T, Foisner R. A-type lamins bind both hetero- and euchromatin, the latter being regulated by lamina-associated polypeptide 2 alpha. Genome Res. 2016;26: 462–473.

40. Ikegami K, Secchia S, Almakki O, Lieb JD, Moskowitz IP. Phosphorylated Lamin A/C in the Nuclear Interior Binds Active Enhancers Associated with Abnormal Transcription in Progeria. Dev Cell. 2020;52: 699–713.e11.

41. Cutler JA, Wong X, Hoskins VE, Gordon M, Madugundu AK, Pandey A, et al. Mapping the micro-proteome of the nuclear lamina and lamin associated domains. bioRxiv. 2019. p. 828210. doi:10.1101/828210

42. Santi S, Cenni V, Capanni C, Lattanzi G, Mattioli E. PCAF Involvement in Lamin A/C-HDAC2 Interplay during the Early Phase of Muscle Differentiation. Cells. 2020;9. doi:10.3390/cells9071735

43. Fišerová J, Maninová M, Sieger T, Uhlířová J, Šebestová L, Efenberková M, et al. Nuclear pore protein TPR associates with lamin B1 and affects nuclear lamina organization and nuclear pore distribution. Cell Mol Life Sci. 2019;76: 2199–2216.

44. Gibcus JH, Samejima K, Goloborodko A, Samejima I, Naumova N, Nuebler J, et al. A pathway for mitotic chromosome formation. Science. 2018;359. doi:10.1126/science.aao6135

45. Nagano T, Lubling Y, Várnai C, Dudley C, Leung W, Baran Y, et al. Cell-cycle dynamics of chromosomal organization at single-cell resolution. Nature. 2017;547: 61–67.

46. Naumova N, Imakaev M, Fudenberg G, Zhan Y, Lajoie BR, Mirny LA, et al. Organization of the mitotic chromosome. Science. 2013;342: 948–953.

47. Abramo K, Valton A-L, Venev SV, Ozadam H, Fox AN, Dekker J. A chromosome folding intermediate at the condensin-to-cohesin transition during telophase. Nat Cell Biol. 2019;21: 1393–1402.

48. Oneill C. Evidence for two distinct mechanisms of anchorage stimulation in freshly explanted and 3T3 Swiss mouse fibroblasts. Cell. 1986. pp. 489–496. doi:10.1016/0092-8674(86)90470-8

49. Moir RD, Yoon M, Khuon S, Goldman RD. Nuclear lamins A and B1: different pathways of assembly during nuclear envelope formation in living cells. J Cell Biol. 2000;151: 1155–1168.

50. van Schaik T, Vos M, Peric-Hupkes D, van Steensel B. Cell cycle dynamics of lamina associated DNA. bioRxiv. 2019. p. 2019.12.19.881979. doi:10.1101/2019.12.19.881979

51. McCord RP, Nazario-Toole A, Zhang H, Chines PS, Zhan Y, Erdos MR, et al. Correlated alterations in genome organization, histone methylation, and DNA-lamin A/C interactions in Hutchinson-Gilford progeria syndrome. Genome Res. 2013;23: 260–269.

52. Taimen P, Pfleghaar K, Shimi T, Möller D, Ben-Harush K, Erdos MR, et al. A progeria mutation reveals functions for lamin A in nuclear assembly, architecture, and chromosome organization. Proc Natl Acad Sci U S A. 2009;106: 20788–20793.

53. Bronshtein I, Kepten E, Kanter I, Berezin S, Lindner M, Redwood AB, et al. Loss of lamin A function increases chromatin dynamics in the nuclear interior. Nat Commun. 2015;6: 8044.

54. Perovanovic J, Dell'Orso S, Gnochi VF, Jaiswal JK, Sartorelli V, Vigouroux C, et al. Laminopathies disrupt epigenomic developmental programs and cell fate. Sci Transl Med. 2016;8: 335ra58.

55. Oldenburg A, Briand N, Sørensen AL, Cahyani I, Shah A, Moskaug JØ, et al. A lipodystrophy-causing lamin A mutant alters conformation and epigenetic regulation of the anti-adipogenic MIR335 locus. Journal of Cell Biology. 2017. pp. 2731–2743. doi:10.1083/jcb.201701043

56. Mio M, Sugiki T, Matsuda C, Mitsuhashi H, Kojima C, Chan SY, et al. Structural instability of lamin A tail domain modulates its assembly and higher order function in Emery-Dreifuss muscular dystrophy. Biochem Biophys Res Commun. 2019;512: 22–28.

57. Bolzer A, Kreth G, Solovei I, Koehler D, Saracoglu K, Fauth C, et al. Three-dimensional maps of all chromosomes in human male fibroblast nuclei and prometaphase rosettes. PLoS Biol. 2005;3: e157.

58. Boyle S, Gilchrist S, Bridger JM, Mahy NL, Ellis JA, Bickmore WA. The spatial organization of human chromosomes within the nuclei of normal and emerin-mutant cells. Hum Mol Genet. 2001;10: 211–219.

59. Cremer M, Grasser F, Lanctôt C, Müller S, Neusser M, Zinner R, et al. Multicolor 3D fluorescence in situ hybridization for imaging interphase chromosomes. Methods Mol Biol. 2008;463: 205–239.

60. Cremer T, Cremer M. Chromosome Territories. Cold Spring Harb Perspect Biol. 2010-3;2. doi:10.1101/cshperspect.a003889

61. Cremer T, Cremer M, Dietzel S, Müller S, Solovei I, Fakan S, et al. Chromosome territories–a functional nuclear landscape. Curr Opin Cell Biol. 2006;18: 307–316.

62. Dixon JR, Selvaraj S, Yue F, Kim A, Li Y, Shen Y, et al. Topological domains in mammalian genomes identified by analysis of chromatin interactions. Nature. 2012;485: 376–380.

63. Luperchio TR, Sauria MEG, Wong X, Gaillard M-C, Tsang P, Pekrun K, et al. Chromosome Conformation Paints Reveal The Role Of Lamina Association In Genome Organization And Regulation. bioRxiv. 2017; 122226.

64. Guelen L, Pagie L, Brasset E, Meuleman W, Faza MB, Talhout W, et al. Domain organization of human chromosomes revealed by mapping of nuclear lamina interactions. Nature. 2008;453: 948–951.

65. Orian A, Abed M, Kenyagin-Karsenti D, Boico O. DamID: a methylation-based chromatin profiling approach. Methods Mol Biol. 2009;567: 155–69.

66. Harr JC, Luperchio TR, Wong X, Cohen E, Wheelan SJ, Reddy KL. Directed targeting of chromatin to the nuclear lamina is mediated by chromatin state and A-type lamins. J Cell Biol. 2015;208: 33–52.

67. Zullo JM, Demarco IA, Piqué-Regi R, Gaffney DJ, Epstein CB, Spooner CJ, et al. DNA sequence-dependent compartmentalization and silencing of chromatin at the nuclear lamina. Cell. 2012;149: 1474–1487.

68. Reddy KL, Zullo JM, Bertolino E, Singh H. Transcriptional repression mediated by repositioning of genes to the nuclear lamina. Nature. 2008;452 SRC - GoogleScholar: 243–247.

69. Wen B, Wu H, Shinkai Y, Irizarry RA, Feinberg AP. Large histone H3 lysine 9 dimethylated chromatin blocks distinguish differentiated from embryonic stem cells. Nat Genet. 2009;41: 246–250.

70. Kind J, Pagie L, de Vries SS, Nahidiazar L, Dey SS, Bienko M, et al. Genome-wide maps of nuclear lamina interactions in single human cells. Cell. 2015;163: 134–147.

71. Kind J, Pagie L, Ortabozkoyun H, Boyle S, de Vries SS, Janssen H, et al. Single-cell dynamics of genome-nuclear lamina interactions. Cell. 2013;153: 178–92.

72. Bian Q, Khanna N, Alvikas J, Belmont AS. β-Globin cis-elements determine differential nuclear targeting through epigenetic modifications. J Cell Biol. 2013;203: 767–783.

73. Nora EP, Lajoie BR, Schulz EG, Giorgetti L, Okamoto I, Servant N, et al. Spatial partitioning of the regulatory landscape of the X-inactivation centre. Nature. 2012;485: 381–385.

74. Fuxa M, Skok J, Souabni A, Salvagiotto G, Roldan E, Busslinger M. Pax5 induces V-to-DJ rearrangements and locus contraction of the immunoglobulin heavy-chain gene 10.1101/gad.291504. Genes Dev. 2004;18: 411–422.

75. Kosak ST, Skok JA, Medina KL, Riblet R, Le Beau MM, Fisher AG, et al. Subnuclear compartmentalization of immunoglobulin loci during lymphocyte development. Science. 2002;296: 158–162.

76. Luperchio TR, Wong X, Reddy KL. Genome regulation at the peripheral zone: lamina associated domains in development and disease. Curr Opin Genet Dev. 2014;25C: 50–61.

77. Yao J, Fetter RD, Hu P, Betzig E, Tjian R. Subnuclear segregation of genes and core promoter factors in myogenesis. Genes Dev. 2011;25: 569–580.

78. Zink D, Amaral MD, Englmann A, Lang S, Clarke LA, Rudolph C, et al. Transcription-dependent spatial arrangements of CFTR and adjacent genes in human cell nuclei. J Cell Biol. 2004;166: 815–825.

79. Wong X, Luperchio TR, Reddy KL. NET gains and losses: the role of changing nuclear envelope proteomes in genome regulation. Curr Opin Cell Biol. 2014;28: 105–120.

80. Williams RRE, Azuara V, Perry P, Sauer S, Dvorkina M, Jørgensen H, et al. Neural induction promotes large-scale chromatin reorganisation of the Mash1 locus. J Cell Sci. 2006;119: 132–140.

81. Reddy KL, Feinberg AP. Higher order chromatin organization in cancer. Semin Cancer Biol. 2013;23: 109–115.

82. Beliveau BJ, Joyce EF, Apostolopoulos N, Yilmaz F, Fonseka CY, McCole RB, et al. Versatile design and synthesis platform for visualizing genomes with Oligopaint FISH probes. Proc Natl Acad Sci U S A. 2012;109: 21301–21306.

83. Beliveau BJ, Boettiger AN, Avendaño MS, Jungmann R, McCole RB, Joyce EF, et al. Single-molecule super-resolution imaging of chromosomes and in situ haplotype visualization using Oligopaint FISH probes. Nat Commun. 2015;6: 7147.

84. Boyle S, Rodesch MJ, Halvensleben HA, Jeddeloh JA, Bickmore WA. Fluorescence in situ hybridization with high-complexity repeat-free oligonucleotide probes generated by massively parallel synthesis. Chromosome Res. 2011;19: 901–909.

85. Kosuri S, Eroshenko N, LeProust E, Super M, Way J, Li JB, et al. A Scalable Gene Synthesis Platform Using High-Fidelity DNA Microchips. Nat Biotechnol. 2010;28: 1295–1299.

86. thereddylab. thereddylab/LADetector. In: GitHub [Internet]. [cited 8 Oct 2018]. Available: https://github.com/thereddylab/LADetector

87. Deato MD, Tjian R. Switching of the core transcription machinery during myogenesis. Genes Dev. 2007;21: 2137–2149.

88. Sauria MEG, Phillips-Cremins JE, Corces VG, Taylor J. HiFive: a tool suite for easy and efficient HiC and 5C data analysis. Genome Biol. 2015;16: 237.

89. Jung YH, Sauria MEG, Lyu X, Cheema MS, Ausio J, Taylor J, et al. Chromatin States in Mouse Sperm Correlate with Embryonic and Adult Regulatory Landscapes. Cell Rep. 2017;18: 1366–1382.

90. Miranda TB, Cortez CC, Yoo CB, Liang G, Abe M, Kelly TK, et al. DZNep is a global histone methylation inhibitor that reactivates developmental genes not silenced by DNA methylation. Mol Cancer Ther. 2009;8: 1579–88.

91. Kubicek S, O’Sullivan RJ, August EM, Hickey ER, Zhang Q, Teodoro ML, et al. Reversal of H3K9me2 by a small-molecule inhibitor for the G9a histone methyltransferase. Mol Cell. 2007;25: 473–481.

92. Yoshida M, Horinouchi S, Beppu T. Trichostatin A and trapoxin: novel chemical probes for the role of histone acetylation in chromatin structure and function. Bioessays. 1995;17: 423–430.

93. Zheng X, Hu J, Yue S, Kristiani L, Kim M, Sauria M, et al. Lamins organize the global three-dimensional genome from the nuclear periphery. bioRxiv. 2017; 211656.

94. Chen Y, Zhang Y, Wang Y, Zhang L, Brinkman EK, Adam SA, et al. Mapping 3D genome organization relative to nuclear compartments using TSA-Seq as a cytological ruler. J Cell Biol. 2018. doi:10.1083/jcb.201807108

95. Larson AG, Elnatan D, Keenen MM, Trnka MJ, Johnston JB, Burlingame AL, et al. Liquid droplet formation by HP1α suggests a role for phase separation in heterochromatin. Nature. 2017;547: 236–240.

96. Larson AG, Narlikar GJ. The Role of Phase Separation in Heterochromatin Formation, Function, and Regulation. Biochemistry. 2018;57: 2540–2548.

97. Strom AR, Emelyanov AV, Mir M, Fyodorov DV, Darzacq X, Karpen GH. Phase separation drives heterochromatin domain formation. Nature. 2017;547: 241–245.

98. Falk M, Feodorova Y, Naumova N, Imakaev M, Lajoie BR, Leonhardt H, et al. Heterochromatin drives organization of conventional and inverted nuclei. bioRxiv. 2018; 244038.

99. Wilson KL, Berk JM. The nuclear envelope at a glance. J Cell Sci. 2010;123: 1973–1978.

100. Wong X, Luperchio TR, Reddy KL. NET gains and losses: the role of changing nuclear envelope proteomes in genome regulation. Curr Opin Cell Biol. 2014;28: 105–120.

101. Luperchio TR, Wong X, Reddy KL. Genome regulation at the peripheral zone: lamina associated domains in development and disease. Curr Opin Genet Dev. 2014;25: 50–61.

102. Wong X, Stewart CL. The Laminopathies and the Insights They Provide into the Structural and Functional Organization of the Nucleus. Annu Rev Genomics Hum Genet. 2020. doi:10.1146/annurev-genom-121219-083616

103. Zullo JM, Demarco IA, Piqué-Regi R, Gaffney DJ, Epstein CB, Spooner CJ, et al. DNA sequence-dependent compartmentalization and silencing of chromatin at the nuclear lamina. Cell. 2012;149: 1474–1487.

104. Lieberman-Aiden E, van Berkum NL, Williams L, Imakaev M, Ragoczy T, Telling A, et al. Comprehensive mapping of long-range interactions reveals folding principles of the human genome. Science. 2009;326: 289–293.

105. Wen B, Wu H, Shinkai Y, Irizarry RA, Feinberg AP. Large histone H3 lysine 9 dimethylated chromatin blocks distinguish differentiated from embryonic stem cells. Nat Genet. 2009;41: 246–250.

106. Towbin BD, González-Aguilera C, Sack R, Gaidatzis D, Kalck V, Meister P, et al. Step-wise methylation of histone H3K9 positions heterochromatin at the nuclear periphery. Cell. 2012;150: 934–947.

107. van Steensel B, Belmont AS. Lamina-Associated Domains: Links with Chromosome Architecture, Heterochromatin, and Gene Repression. Cell. 2017;169: 780–791.

108. Strom AR, Emelyanov AV, Mir M, Fyodorov DV, Darzacq X, Karpen GH. Phase separation drives heterochromatin domain formation. Nature. 2017;547: 241–245.

109. Strom AR, Brangwynne CP. The liquid nucleome - phase transitions in the nucleus at a glance. J Cell Sci. 2019;132. doi:10.1242/jcs.235093

110. Kind J, van Steensel B. Stochastic genome-nuclear lamina interactions: modulating roles of Lamin A and BAF. Nucleus. 2014;5: 124–130.

111. Güttinger S, Laurell E, Kutay U. Orchestrating nuclear envelope disassembly and reassembly during mitosis. Nat Rev Mol Cell Biol. 2009;10: 178–191.

112. Gerlich D, Beaudouin J, Kalbfuss B, Daigle N, Eils R, Ellenberg J. Global chromosome positions are transmitted through mitosis in mammalian cells. Cell. 2003;112: 751–764.

113. Salina D, Enarson P, Rattner JB, Burke B. Nup358 integrates nuclear envelope breakdown with kinetochore assembly. J Cell Biol. 2003;162: 991–1001.

114. Burke B, Ellenberg J. Remodelling the walls of the nucleus. Nat Rev Mol Cell Biol. 2002;3: 487–497.

115. Gibcus JH, Samejima K, Goloborodko A, Samejima I, Naumova N, Nuebler J, et al. A pathway for mitotic chromosome formation. Science. 2018;359. doi:10.1126/science.aao6135

116. Goldman RD, Goldman AE, Shumaker DK. Nuclear Lamins: Building Blocks of Nuclear Structure and Function. Nuclear Organization in Development and Disease. 2008. pp. 3–21. doi:10.1002/0470093765.ch2

117. Davies BSJ, Fong LG, Yang SH, Coffinier C, Young SG. The posttranslational processing of prelamin A and disease. Annu Rev Genomics Hum Genet. 2009;10: 153–174.

118. Jung H-J, Coffinier C, Choe Y, Beigneux AP, Davies BSJ, Yang SH, et al. Regulation of prelamin A but not lamin C by miR-9, a brain-specific microRNA. Proc Natl Acad Sci U S A. 2012;109: E423–31.

119. Swift J, Ivanovska IL, Buxboim A, Harada T, Dingal PCDP, Pinter J, et al. Nuclear lamin-A scales with tissue stiffness and enhances matrix-directed differentiation. Science. 2013;341: 1240104.

120. Nissan X, Blondel S, Navarro C, Maury Y, Denis C, Girard M, et al. Unique preservation of neural cells in Hutchinson- Gilford progeria syndrome is due to the expression of the neural-specific miR-9 microRNA. Cell Rep. 2012;2: 1–9.

121. Coffinier C, Jung H-J, Li Z, Nobumori C, Yun UJ, Farber EA, et al. Direct synthesis of lamin A, bypassing prelamin a processing, causes misshapen nuclei in fibroblasts but no detectable pathology in mice. J Biol Chem. 2010;285: 20818–20826.

122. Lopez-Mejia IC, de Toledo M, Chavey C, Lapasset L, Cavelier P, Lopez-Herrera C, et al. Antagonistic functions of LMNA isoforms in energy expenditure and lifespan. EMBO Rep. 2014;15: 529–539.

123. Amendola M, van Steensel B. Nuclear lamins are not required for lamina-associated domain organization in mouse embryonic stem cells. EMBO Rep. 2015;16: 610–617.

124. Zheng X, Kim Y, Zheng Y. Identification of lamin B–regulated chromatin regions based on chromatin landscapes. Molecular Biology of the Cell. 2015. pp. 2685–2697. doi:10.1091/mbc.e15-04-0210

125. Kim Y, Zheng X, Zheng Y. Proliferation and differentiation of mouse embryonic stem cells lacking all lamins. Cell Res. 2013;23: 1420–1423.

126. Zheng X, Kim Y, Zheng Y. Identification of lamin B-regulated chromatin regions based on chromatin landscapes. Mol Biol Cell. 2015;26: 2685–2697.

127. Pugh GE, Coates PJ, Lane EB, Raymond Y, Quinlan RA. Distinct nuclear assembly pathways for lamins A and C lead to their increase during quiescence in Swiss 3T3 cells. J Cell Sci. 1997;110 (Pt 19): 2483–2493.

128. Vaughan A, Alvarez-Reyes M, Bridger JM, Broers JL, Ramaekers FC, Wehnert M, et al. Both emerin and lamin C depend on lamin A for localization at the nuclear envelope. J Cell Sci. 2001;114: 2577–2590.

129. Dechat T, Gesson K, Foisner R. Lamina-independent lamins in the nuclear interior serve important functions. Cold Spring Harb Symp Quant Biol. 2010;75: 533–543.

130. Gesson K, Vidak S, Foisner R. Lamina-associated polypeptide (LAP)2α and nucleoplasmic lamins in adult stem cell regulation and disease. Semin Cell Dev Biol. 2014;29: 116–124.

131. Ikegami K, Secchia S, Almakki O, Lieb JD, Moskowitz IP. Phosphorylated Lamin A/C in the Nuclear Interior Binds Active Enhancers Associated with Abnormal Transcription in Progeria. Dev Cell. 2020;52: 699–713.e11.

132. Sakaue-Sawano A, Kurokawa H, Morimura T, Hanyu A, Hama H, Osawa H, et al. Visualizing spatiotemporal dynamics of multicellular cell-cycle progression. Cell. 2008;132: 487–498.

133. Vassilev LT, Tovar C, Chen S, Knezevic D, Zhao X, Sun H, et al. Selective small-molecule inhibitor reveals critical mitotic functions of human CDK1. Proc Natl Acad Sci U S A. 2006;103: 10660–10665.

134. Gibcus JH, Samejima K, Goloborodko A, Samejima I, Naumova N, Nuebler J, et al. A pathway for mitotic chromosome formation. Science. 2018;359. doi:10.1126/science.aao6135

135. Ikegami K, Secchia S, Almakki O, Lieb JD, Moskowitz IP. Phosphorylated Lamin A/C in the Nuclear Interior Binds Active Enhancers Associated with Abnormal Transcription in Progeria. Dev Cell. 2020;52: 699–713.e11.

136. Naetar N, Foisner R. Lamin complexes in the nuclear interior control progenitor cell proliferation and tissue homeostasis. Cell Cycle. 2009;8: 1488–1493.

137. Solovei I, Kreysing M, Lanctôt C, Kösem S, Peichl L, Cremer T, et al. Nuclear architecture of rod photoreceptor cells adapts to vision in mammalian evolution. Cell. 2009;137: 356–368.

138. Ikegami K, Secchia S, Almakki O, Lieb JD, Moskowitz IP. Phosphorylated Lamin A/C in the Nuclear Interior Binds Active Enhancers Associated with Abnormal Transcription in Progeria. Dev Cell. 2020;52: 699–713.e11.

139. Belmont AS, Zhai Y, Thilenius A. Lamin B distribution and association with peripheral chromatin revealed by optical sectioning and electron microscopy tomography. J Cell Biol. 1993;123: 1671–1685.

140. Schermelleh L, Carlton PM, Haase S, Shao L, Winoto L, Kner P, et al. Subdiffraction multicolor imaging of the nuclear periphery with 3D structured illumination microscopy. Science. 2008;320: 1332–1336.

141. Vogel MJ, Peric-Hupkes D, van Steensel B. Detection of in vivo protein-DNA interactions using DamID in mammalian cells. Nat Protoc. 2007;2: 1467–1478.

142. Reddy KL, Zullo JM, Bertolino E, Singh H. Transcriptional repression mediated by repositioning of genes to the nuclear lamina. Nature. 2008;452: 243–247.

Curriculum Vitae

EDUCATION

Ph.D. Human Genetics 2015- 2020
Johns Hopkins University School of Medicine, Baltimore, MD
Advisors:
Karen L. Reddy, PhD – Department of Biological Chemistry
Loyal A. Goff, PhD – Department of Neuroscience and Department of Genetic Medicine

B.S. Biology Wake Forest University 2011-2015

High School NC School of Science and Mathematics, Durham, NC 2009-2011

RESEARCH EXPERIENCE

Johns Hopkins School of Medicine Institute for Genetic Medicine 2017 - 2020
Advisors: Karen Reddy, PhD, Dr. Loyal Goff, PhD
Characterizing compartment formation and the role of Lamin C during genome reorganization after mitosis

- Utilized super-resolution imaging-based techniques in live and fixed cells to characterize the steps and timing heterochromatic compartment formation during mitosis
- Determined Lamin C is necessary for Lamina Associated Domain establishment at the nuclear periphery after cell division

Johns Hopkins School of Medicine Institute for Genetic Medicine 2016 - 2017
Advisor: Dr. Michael Parsons
Zebrafish as a model organism to understand the role of EpCAM in β cell neogenesis in the pancreas

- Used CRISPR/Cas9 to create an EpCAM mutant zebrafish line and characterized beta cell regeneration in affected pancreas utilizing nitroreductase-mediated cell-type specific ablation
- Localized marker genes for beta cell progenitors found in zebrafish in human pancreas tissue using immunofluorescence

Wake Forest University Biology Department 2013- 2015
Advisor: Ke Zhang, PhD
Explored the role of exon junction complex member fal1 in splicing meiotic mRNAs in S. pombe

- Characterized meiotic mRNA splice variants in fal1 deletion S. pombe strain using semi-quantitative PCR and qRTPCR

Wake Forest University Biology Department 2014
Advisor: Bill Conner, PhD
Designed and implemented assay to differentiate Acrtiidae species from guano extracted DNA

- Designed species-specific PCR primers to cytochrome C locus to amplify specific moth species DNA out of bat guano to determine efficacy of sonar jamming and acoustic aposematism in moths in the field
- Imaged *Actiidae* tymbal organs using confocal and electron microscopy to characterize click ridges

Wake Forest Baptist Medical Center Center for Genomics 2013- 2014
Advisor: Gregory Hawkins, PhD
Created a genotyping strategy for an APOL4 insertion that causes renal failure in humans

Wake Forest Baptist Medical Center Tumor Biology Department 2011- 2013
Supervisor: Purnima Dubey, PhD

- Maintained mouse colony including breeding, genotyping and survival surgery
- Preformed histology for immune markers on prostate tumors

FELLOWSHIPS

Johns Hopkins Collaborative Teaching Fellowship 2018-2019
UNC Chapel Hill SPIRE Postdoctoral Fellowship (IRACDA) 2020-2023

PEDAGOGICAL TRAINING

Affiliate Instructor *Loyola University Maryland, Baltimore, MD* 2019
Organismal Biology Lab

Teaching Fellow *Goucher College, Towson, MD* 2018-2019
Advisor: Judy Levine, PhD
Designer Genes: Brave New World of CRISPR
Developed syllabus and curriculum for interdisciplinary elective on gene editing for non-majors

Introduction to Chemistry with Lab *Goucher College, Towson, MD*

Co-taught flipped classroom and designed prelab lectures on general chemistry

Goucher College Implementing Teamwork Workshop 2019

JHU Preparing Future Faculty Teaching Academy Certification 2018-2019

JHU 3 Day Teaching Institute Workshop 2018

Teaching Assistant 2017

Fundamentals of Genetics *Johns Hopkins School of Medicine, Baltimore, MD*

Designed review lecture and facilitated flipped classroom for drosophila genetics topics

MENTEES

(year mentored, Name, position during mentorship, current position)

2019-2020	Kristiana Smith, High school student at Baltimore Polytechnic Institute
2018-2019	Erica Neumann, B.S., Undergraduate student UMBC
2016-2017	Megan Groves, B.S., Undergraduate student Johns Hopkins University
2015	Karin Peterson, B.S., Undergraduate student Bemidji State University
2014-2015	Amanda McAneny, B.S., Undergraduate student WFU, Medical student University of Maryland School of Medicine
2014-2015	Emily Fishman, B.S., Undergraduate student WFU, Medical student WFUSOM
2014-2015	Andrew Bray, B.S., Undergraduate student WFU, Research Technician Wake Forest Baptist Health
2014-2015	Lauren Kraty, B.S., undergraduate student WFU, Medical student WFUSOM
2014-2015	Sarah Irvine, B.S. undergraduate student, Wake Forest University
2013	Daniel Guerroro, B.S. undergraduate student, Wake Forest University
2012	Tatum Lemly, B.S., undergraduate student WFU, Physician Assistant

PUBLICATIONS IN PROGRESS

Victoria Hoskins, Kristiana Smith, Karen L Reddy. Understanding the interface between the nuclear lamin and chromatin. (to be submitted to Current Opinion in Genetics and Development by invitation)

PUBLICATIONS

Victoria Hoskins, Xianwrong Wong, Jennifer Harr, Molly Gordon, Karen L Reddy. Lamin C is required to establish genome organization after mitosis. BioRxiv. 213884. (submitted to Genome Biology) https://www.biorxiv.org/content/10.1101/2020.07.28.213884v1

Jevon A Cutler, Xianwrong Wong, **Victoria Hoskins**, Karen L Reddy. 2019. Mapping the micro-proteome of the nuclear lamina and lamin associated domains. BioRxiv. 828210. (under review at Life Science Alliance) https://www.biorxiv.org/content/10.1101/828210v1

Teresa Romeo Luperchio, Michael E.G. Sauria, **Victoria E Hoskins**, Xianrong Wong, Emily DeBoy, Marie-Cecile Gaillard, Peter Tsang, Katja Pekrun, Robert A Ach, Alice Yamada, James Taylor, Karen L Reddy. 2018. The repressive genome compartment is established early in the cell cycle before forming the lamina associated domains. BioRxiv. 481598. (submitted to Nature Communications) https://www.biorxiv.org/content/10.1101/481598v1

Victoria Hoskins, Bahjat Fadi Marayati, Robert W. Boger, James F. Tucker, Emily S. Fishman, Andrew S. Bray, and Ke Zhang. 2016. The fission yeast MTREC and EJC orthologs ensure the maturation of meiotic transcripts during meiosis. RNA 22: 1-11. https://www.ncbi.nlm.nih.gov/pmc/articles/PMC4986891/

ORAL PRESENTATIONS

VE Hoskins. Exploring the role of lamin C in re-establishing genome organization after cell division. March 2020. Keystone Higher-Order Chromatin Architecture in Time and Space.

VE Hoskins. Exploring the role of lamin C in re-establishing genome organization after cell division. December 2019. JHU chromatin and chromosomes work shop.

VE Hoskins. Dynamic LAD Reorganization After Mitosis. May 2018. JHU chromatin and chromosomes work shop.

POSTERS

V. Hoskins, XR. Wong, T. Luperchio, M. Gordon, K. Reddy. Exploring the role of lamin C in re-establishing genome organization after cell division. December 2019. ASCB EMBO

V. Hoskins, XR. Wong, T. Luperchio, M. Gordon, K. Reddy. Exploring the role of lamin C in re-establishing genome organization after cell division. November 2019. NCI Chromosome Biology Symposium.

V. Hoskins, E. Deboy, XR. Wong, T. Luperchio, M. Gordon, K. Reddy. Chromosome Compartment Organization during the cell cycle. May 2018. CSHL Nuclear Organization

V. Hoskins, E. DeBoy, XR. Wong, T. Luperchio, M. Gordon, K. Reddy. Lamina associated domain dynamics during cell cycle investigated by super-resolution microscopy. December 2018. ASCB EMBO

V. Hoskins, R. Beer, H. Edelman, M Parsons. EpCAM is a transcriptional target of Sox9 in pancreatic progenitors. May 2017. Mid-Atlantic SDB